IS-T-1864

Influence of a Perpendicular Magnetic Field on the Thermal Depinning of a Single Abrikosov Vortex in a Superconducting Josephson Junction

by

Kouzoudis, Dimitris

PHD Thesis submitted to Iowa State University

Ames Laboratory, U.S. DOE

Iowa State University

Ames, Iowa 50011

Date Transmitted: February 12, 1999

PREPARED FOR THE U.S. DEPARTMENT OF ENERGY

UNDER CONTRACT NO. W-7405-Eng-82.

DISCLAIMER

AVAILABILITY:

To DOE and DOE contractors: Office of Scientific and Technical Information
P.O. Box 62
Oak Ridge, TN 37831

prices available from: (615) 576-8401
FTS: 626-8401

To the public: National Technical Information Service
U.S. Department of Commerce
5285 Port Royal Road
Springfield, VA 22161

TABLE OF CONTENTS

1 INTRODUCTION 1

2 THEORY AND MODELS 4

Josephson equations 4

Spatial variation of the phase difference 5

Small junction limit 8

Physical interpretation of Eq. (2.11) 9

Critical current 12

External magnetic field parallel to the plane of the junction 12

Single vortex 12

Two vortices 17

Elementary pinning force 17

3 EXPERIMENTAL TECHNIQUES AND CONDITIONS 20

Sample preparation 20

Cryostat 25

Data acquisition 27

4 RESULTS AND DISCUSSION 29

Resistivity measurements 29

Nucleation of a vortex 33

Determination of I_{00} and B_0 35

Depinning current versus temperature through the bottom film 37

Field cooling process 42

Thermal depinning in the absence of an applied field 44

Thermal depinning in the presence of an applied field $B_z = 10$ mG 55

Thermal depinning in the presence of an applied field $B_z = -10$ mG 66

Thermal depinning temperatures versus applied field B_z 66

Two vortex problem 66

5 CONCLUSIONS 80

APPENDIX A CONVERSION BETWEEN MKSA AND GAUSSIAN UNITS . . . 81

APPENDIX B GLOSSARY AND TERMINOLOGY 83

BIBLIOGRAPHY 84

ACKNOWLEDGMENTS 87

LIST OF TABLES

Table 3.1 Deposition and oxidation parameters for the samples DK5-91 and MB3-126 . . 22

Table 3.2 The scanner connections of Fig 3.5 and their functions 27

Table 4.1 The eight pinning sites of Figure 4.15 and their corresponding depinning temperatures 54

Table 4.2 The twenty eight pinning sites of Figure 4.19 and their corresponding depinning temperatures 65

Table 4.3 The sixteen pinning sites of Figure 4.23 and their corresponding depinning temperatures 71

Table 4.4 The temperatures where the vortex was first depinned T_0^{dep} versus the perpendicular magnetic field B_z 71

Table 4.5 The thirteen pinning sites of Figure 4.27 75

LIST OF FIGURES

Figure 2.1 Schematic of a Josephson junction. S and I denote the superconducting electrodes and the insulating barrier correspondingly 5

Figure 2.2 Loss of current uniformity across the junction under the presence of a magnetic field 7

Figure 2.3 Integration path across a Josephson junction 8

Figure 2.4 Physical interpretation of Eq. (2.11) 10

Figure 2.5 Magnetic flux through a strip 11

Figure 2.6 Phase due to an external field parallel to the junction 13

Figure 2.7 Theoretical Fraunhofer diffraction pattern 14

Figure 2.8 Vortex nucleation at the bottom film. The flux lines in the insulating barrier a) are shielded by the top superconducting film and b) they find their way through the top film by means of a second vortex, which in general will be misaligned from the first one 15

Figure 2.9 Phase due to a single vortex 18

Figure 2.10 Image vortex lattice 19

Figure 3.1 Cross type Josephson junction 21

Figure 3.2 The sputtering process 22

Figure 3.3 The high vacuum sputtering chamber 23

Figure 3.4 The cryostat 26

Figure 3.5 The connections to the junction in the cryostat. 28

Figure 4.1 Dependence of the bottom film's resistance versus temperature around the transition temperature 30

Figure 4.2 Dependence of the top film's resistance versus temperature around the transition temperature 31

Figure 4.3 Determination of the critical current I_c from the $V - I$ curves 32

Figure 4.4 Dependence of the junction's critical current versus temperature for a) normal I_0 scale and b) logarithmic I_0 scale. The latter plot reveals the existence of a transition temperature which is in agreement with a transition-type theoretical fit 34

Figure 4.5 Theoretical calculation of I_0/I_{00} for vortex position along the x-axis of the junction 36

Figure 4.6 Determination of I_{00} and B_0 by comparing a) a measured diffraction pattern of a rather unique shape with b) a theoretical diffraction pattern with similar properties 38

Figure 4.7 Dependence of the critical current on the transport current I_p, applied through the bottom film at $T_p = 8.158$ K. The inset indicates that every point on the graph corresponds to a different $V - I$ measurement with I_0 determined as in Figure 4.3 40

Figure 4.8 Dependence of the sum of the square differences on the transport current I_p applied through the bottom film at $T_p = 8.158$ K 41

Figure 4.9 Determination of the depinning current for different temperatures: a) a family of curves like the one in Figure 4.8 and b) the corresponding I_p^{dep} extracted from these curves. Only data for a few temperatures are shown in the former plot for clarity 43

Figure 4.10 Critical current versus the field B_z while cooling 45

Figure 4.11 The diffraction patterns at points A, B, C, and D of Figure 4.10 46

Figure 4.12 Multi-vortex diffraction pattern taken after field cooling at $B_z = 40$ mG followed by application of a transport current of $I_b = 95$ mA through the bottom film . 48

Figure 4.13 Thermal depinning in the absence of an applied field 49

Figure 4.14 Diffraction patterns of points "a" through "h" in Fig. 4.13 50

Figure 4.15 Motion of the vortex in the junction during the free-field thermal depinning experiment 53

Figure 4.16 Energy-spectrum-like diagram of the depinning temperatures of the field-free thermal depinning experiment 54

Figure 4.17 Diffraction pattern taken after a vortex was field cooled nucleated with $B_z = 50$ mG 56

Figure 4.18 The diffraction patterns taken during the $B_z = 10$ mG thermal depinning experiment 57

Figure 4.19 Motion of the vortex in the junction during the B_z = 10 mG thermal depinning experiment 62
Figure 4.20 Energy-spectrum-like diagram of the depinning temperatures of the B_z = 10 mG thermal depinning experiment 63
Figure 4.21 The eight strongest pinning sites of the B_z = 10 mG thermal depinning experiment and the temperature differences needed to depin the vortex 64
Figure 4.22 The diffraction patterns taken during the B_z = -10 mG thermal depinning experiment 67
Figure 4.23 Motion of the vortex in the junction during the B_z = -10 mG thermal depinning experiment 70
Figure 4.24 Energy-spectrum-like diagram of the depinning temperatures of the B_z = -10 mG thermal depinning experiment 72
Figure 4.25 The eight strongest pinning sites of the B_z = -10 mG thermal depinning experiment and the temperature differences needed to depin the vortex 73
Figure 4.26 Depinning temperature where the vortex first moves versus the applied field . . 74
Figure 4.27 Two vortex depinning experiment by the application of a transport current through the bottom film. The arrows indicate depinning jumps 76
Figure 4.28 Diffraction patterns corresponding to each point of Figure 4.27 77
Figure 4.29 The positions of the two vortices shown in Table 4.5 during the transport current depinning experiment 79

1 INTRODUCTION

Since the experiment of W. Meissner and R. Ochsenfeld in 1933, it has been known that magnetic flux is expelled from superconductors [1]. Further experiments showed that there are two broad classes of materials, called type I and type II, which expel the flux in different ways. In type I superconductors, flux is expelled for all fields up to a critical field H_c, where the sample goes completely normal in a first order transition. In type II superconductors on the other hand, total flux expulsion occurs only below a critical field called H_{c1}. Above H_{c1}, the so called mixed state appears where the flux penetrate in the form of flux tubes, each carrying a quantum of flux [2]. These flux tubes are called Abrikosov vortices after the theoretical physicist who first predicted their existence [3].

This fundamental difference between type I and type II superconductors is due to the different sign of the surface energy between normal and superconducting phases. In type II materials the surface energy is negative and the total free energy can be lowered by subdivision of the superconductor into superconducting and normal regions giving the mixed state. The basic unit of this state is the Abrikosov vortex[3, 4] in which the circulating charge carriers have one quantum of angular momentum. The vortex substructure consists essentially of a central cylindrical core region where the superconducting order parameter rises from zero to unity over a distance comparable to ξ, the coherence length [5, 6], and another region, again cylindrical, in which supercurrents circulate in order to generate one quantum of flux. This second region has a characteristic radius of λ, the magnetic penetration length.

Material defects often form pinning centers where it is energetically more favorable for the vortices to be pinned at low enough temperatures. This is because the defects act as small normal regions inside the bulk superconductor and so it takes less free energy if the vortex core, which is basically normal, resides on the defect than if the core is located in the superconducting bulk. The force pinning a single vortex to a defect is known as the elementary pinning force.

Flux pinning is of great practical importance because it determines the critical current of a type II superconductor. In order to have zero electrical resistance, the vortices must not move. By Faraday's law, when the flux of a vortex is moving, it induces a voltage and therefore a finite resistance which

dissipates energy. Hence for dissipationless supercurrent, the vortex must be pinned.

For the present work, Nb was chosen as a suitable material to study pinning because it is a homogeneous intrinsic type II superconductor that is used in microelectronic circuits. The details of pinning depend on many variables, such as the relative magnitude of λ/ξ and all defects that may cause a suppression of the order parameter. For technological applications, a high transition temperature (T_c) is desirable but the high T_c superconductors (HTSC) have a complicated chemical stoichiometry as well as short coherence length ($\sim$ 1.0 nm) [7]. Both of these factors make it difficult to use them for the study of the elementary pinning force. By contrast, the conventional low T_c Nb has $\lambda \sim \xi \sim 40$ nm and it can be easily handled since it is just a single metallic element. In addition, Nb appears to be more attractive for study than the other elemental superconductors, such as In, Sn and Pb because:

- It has the highest transition temperature $T_c \simeq 9.2$ K.
- Niobium oxide is a good insulator, it is very inert against acids, mechanically hard and stable, dense and well bonded to Nb [8].
- Nb has a melting point above 2000 K and low diffusivity below 400 K yielding good long-time material stability, even when repeatedly cycled between 4 K and 300 K [9].

It should also be mentioned that bulk Nb is a type II superconductor in contrast to the majority of metallic superconductors which are type I when they are bulk and type II only when they are thin films [10, 11, 12, 13].

A knowledge of the motion of each individual vortex in a superconducting material is crucial for the understanding of pinning. Direct observation of the vortex structure was first made with the aid of neutron diffraction [14] and later with the use of ferromagnetic powders in magnetic decoration experiments [15]. These techniques are successful only when a large number of vortices are present, and therefore they are best used to study the vortex lattice properties and its interaction with grain boundaries and other large material defects. On the other hand, Josephson junctions are very sensitive to magnetic flux changes and they can be used to identify the position of a single vortex and its interactions with any kind of defects in the superconductor.

A Josephson junction basically consists of two superconducting films which are separated by a thin insulator or normal metal barrier. Each superconductor induces into the barrier a finite pair amplitude [16, 17, 18] which decays exponentially towards the middle of the barrier. Provided the barrier is not too thick, the overlap of the two pair wavefunctions will be large enough for the coupling energy [19, 20]

of the two superconductors to exceed the thermal fluctuation energy [20, 21, 22]. As a result, phase coherence will be established across the junction, and Josephson tunneling becomes possible.

Several papers have been published outlining the basic properties a Josephson junction containing one vortex. The first task was to determine the position of the vortex in a junction. A method involving only current-voltage measurement was worked out by Miller et al [23] and Hyun et al [24]. In this method, use is made of the Josephson current density [25] which is given by the equation $J = J_0 sin(\gamma)$, where γ is the gauge invariant phase difference across the junction. This phase depends on the local magnetic field and so when a vortex is present in the junction, its field has a direct impact on the measured Josephson current density across the junction. S. Miller and D. Finnemore [26] were the first to locate a single vortex in a superconductor-normal metal-superconductor (SNS) junction. Subsequently, O. B. Hyun et al [24] measured the elementary pinning force of a single vortex trapped in a Pb(2.5 at %)Bi thin film and O. B. Hyun [27] investigated the single vortex motion in a SNS Josephson junction made of PbBi(2.5 at %)-AgAl(4 at %)-PbBi(2.5 at %). The SNS junctions first used in this work had the disadvantage of having a low junction resistance (in the micro-ohm range) which causes the voltage signals to be in the range of a few tenths of a nanovolt and therefore difficult to measure. One way around this problem is to introduce an extra insulating layer leading to a superconductor-normal metal-insulator-superconductor (SNIS) junctions. Qiang Li [28] made used of a Pb-Al-Al_xO_y-PbBi junction in order to further investigate the motion of a single vortex and measure the elementary pinning force in these SNIS junctions. Subsequently, Sanders [29] studied the thermal depinning process in a Pb-Al-Al_xO_y-PbBi junction and found that the first depinning occurs when the order parameter of the bulk Pb is about 20% of the T = 0 value. Junghyun Sok[30] repeated this experiment for a Nb-Al-Al_xO_y-Nb junction and found that the corresponding quantity was equal to 24%.

The prime interest of the present research is to measure the thermal energy needed for depinning a trapped vortex when an external magnetic field is perpendicular to the plane of the junction, and thus there are Meissner currents flowing along the edge of the film. These currents introduce an additional force and we wish to study thermal depinning under the influence of this force. These studies are of interest because Nb junctions are used in a wide range of electronic applications. Such junctions are useful, for instance, in superconducting quantum interference devices (SQUIDs) or in vortex-flow transistors because their performance can be enhanced by tuning the parameters of the individual junctions to optimum operation values [31]. Furthermore gated Josephson junctions can be used as Josephson field-effect transistors (JOFETs) [32].

2 THEORY AND MODELS

Josephson equations

In 1957, Bardeen, Cooper, and Schrieffer [33] developed a microscopic theory (known as BCS theory) to describe both a superconducting ground state wavefunction and the excitation spectrum in very general terms. This theory develops a relation for the transition temperature T_c in terms of: the Debye frequency, ω_D; the coupling constant for the attractive interaction of pairs of electrons, V; and the normal state density of states, $N(0)$;

Although the BSC theory is the fundamental microscopic theory of superconductivity, it does not take into account the spatial inhomogeneity which is of great importance in type II superconductors. On the other hand, the macroscopic phenomenological Ginzburg-Landau theory [34] is very successful in describing phenomena in which both the fields and the wavefunctions vary over space. The main point of this theory is the derivation of the local free energy of the superconductor, the minimization of which leads to the celebrated Ginzburg-Landau differential equations

$$\alpha\psi + \beta|\psi|^2\psi + \frac{1}{2m^*}\left(\frac{\hbar}{i}\nabla - \frac{e^*}{c}\mathbf{A}\right)^2\psi = 0 \tag{2.1}$$

$$\mathbf{J} = \frac{e^*\hbar}{2m^*i}(\psi^*\nabla\psi - \psi\nabla\psi^*) - \frac{e^{*2}}{m^*c}\psi^*\psi\mathbf{A} \tag{2.2}$$

where α and β are parameters of the theory, $\mathbf{A}$ is the vector potential, $\psi = |\psi|e^{i\theta}$ is the order parameter and $\mathbf{J}$ is the supercurrent density. This theory describes the wavefunction of the vortex state and provides an excellent tool to predict the behavior of type II materials.

In 1962, Josephson [25] was able to predict that a zero voltage supercurrent

$$I_s = I_c sin\Delta\theta \tag{2.3}$$

should flow between two superconducting electrodes separated by a thin insulating barrier of thickness L as in Figure 2.1. Here $\Delta\theta$ is the difference in the phase of the Ginzburg-Landau wavefunction, ψ, in the two electrodes, and the critical current I_c is the maximum supercurrent that the junction can

support. Josephson also predicted that under a potential difference V across the junction, $\Delta\theta$ would vary as

$$\frac{d\Delta\theta}{dt} = \frac{2eV}{\hbar} \tag{2.4}$$

These two effects are widely known as the dc and ac Josephson effects and have been fully confirmed experimentally.

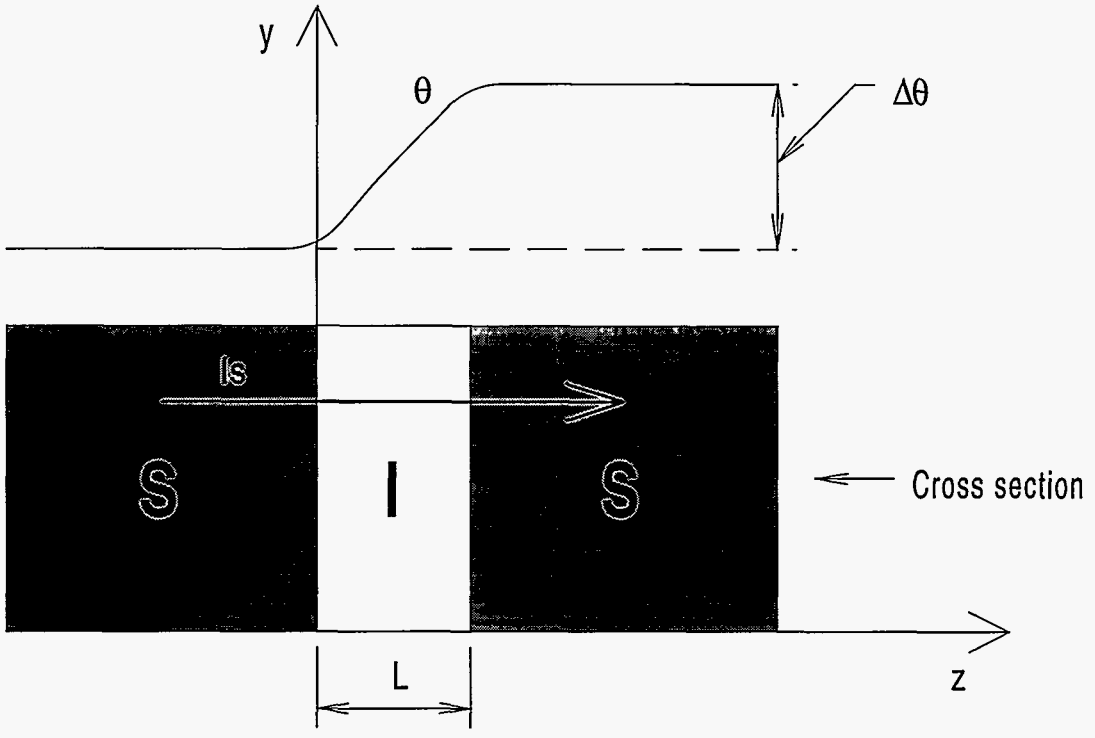

Figure 2.1 Schematic of a Josephson junction. S and I denote the superconducting electrodes and the insulating barrier correspondingly

Spatial variation of the phase difference

If no magnetic fields are present in the junction, the phase θ in each electrode is constant and the current of Eq. (2.3) is uniform across the junction, as in Figure 2.2. With an applied field $\mathbf{B}$, there will be a vector potential $\mathbf{A}$, where $\mathbf{B} = \nabla \times \mathbf{A}$, and thus a spatial variation of the phase of the wavefunction.

In general $\Delta\theta$ would be a function of x and y. Eq. (2.3) then should be modified to

$$J(x,y) = J_0 sin\Delta\theta(x,y) \tag{2.5}$$

where $J(x,y)$ is the supercurrent density across the junction. The current can be found by integrating $J(x,y)$ over the entire cross section. In order to do so, $\Delta\theta$ should be known as a function of x and y. Substitution of $\psi = |\psi|e^{i\theta}$ into Eq. (2.2) gives

$$\hbar\nabla\theta - \frac{e^*}{c}\mathbf{A} = \frac{m^*\mathbf{J}}{e^*|\psi|^2} \tag{2.6}$$

It is well known [35] that supercurrents flow only on the surface and so $\mathbf{J}$ can be taken as zero deep inside the superconductor. For the path Γ shown in Figure 2.3

$$\oint_\Gamma \mathbf{A}\cdot\mathbf{dl} = \int_S \mathbf{B}\cdot\mathbf{dS} \tag{2.7}$$

where S is any surface bounded by Γ. Using elementary properties of calculus

$$\int_{\Gamma_1}\nabla\theta_1\cdot\mathbf{dl} + \int_{\Gamma_2}\nabla\theta_2\cdot\mathbf{dl} = (\theta_1(y+dy)-\theta_1(y)) + (\theta_2(y)-\theta_2(y+dy)) = \Delta\theta(y) - \Delta\theta(y+dy) \tag{2.8}$$

The corresponding integrations along Γ_3 and Γ_4 cancel each other because they are infinitesimally close and have opposite directions. Therefore, the integration of Eq. (2.6) leads to

$$\Delta\theta(y+dy) - \Delta\theta(y) = -\frac{2\pi L}{\Phi_0}B_x dy \tag{2.9}$$

where B_x is the component of the magnetic field along the x-axis and $\Phi_0 = hc/e^*$ is the flux quantum. A similar argument leads to

$$\Delta\theta(x+dx) - \Delta\theta(x) = \frac{2\pi L}{\Phi_0}B_y dx \tag{2.10}$$

which implies that in general [20]

$$\nabla_{xy}\Delta\theta(x,y) = \frac{2\pi L}{\Phi_0}B\times\hat{z} \tag{2.11}$$

This equation gives the x,y variation of $\Delta\theta$ in terms of the magnetic field present in the junction. In practice, there is a substantial penetration of magnetic field inside the two superconducting electrodes and so L should be replaced by

$$d_{eff} = L + \lambda_1 + \lambda_2 \tag{2.12}$$

where λ_1 and λ_2 are the penetration lengths in the electrodes 1 and 2 respectively.

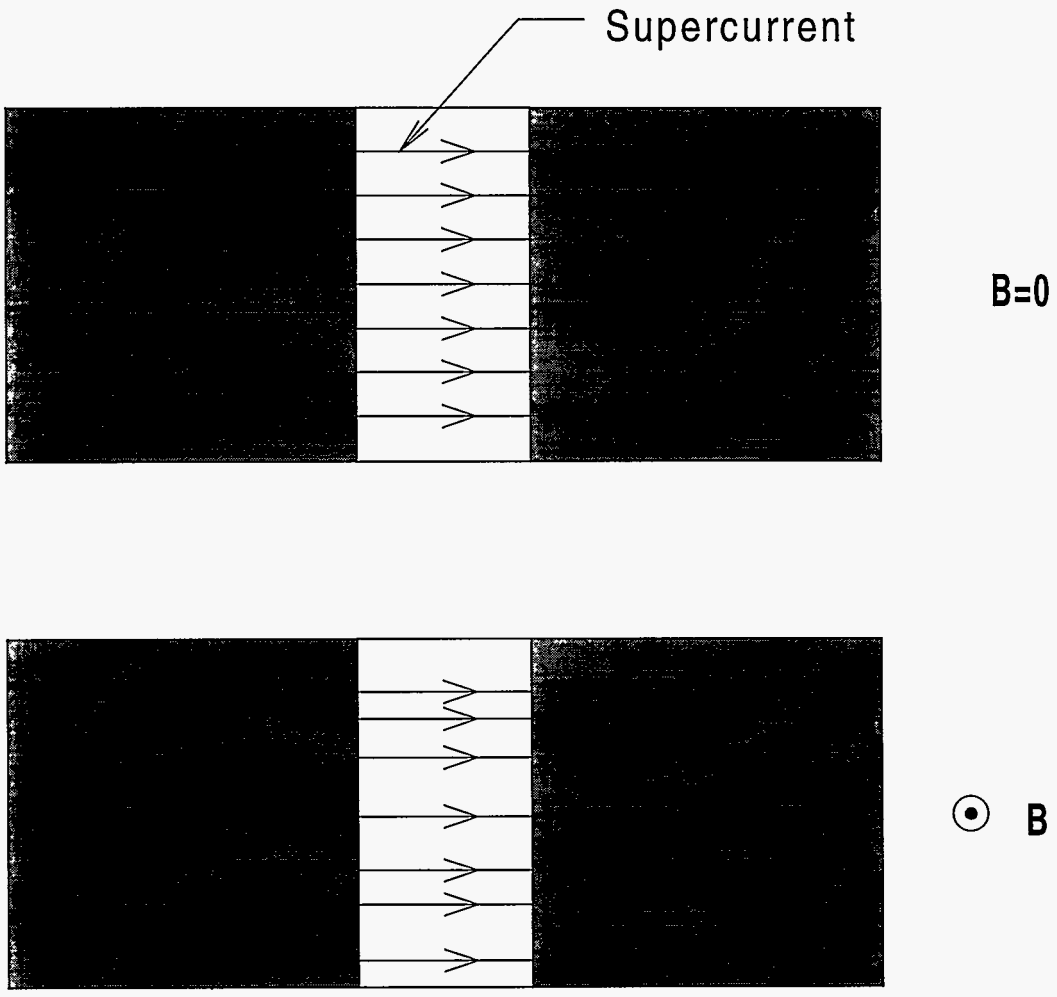

Figure 2.2 Loss of current uniformity across the junction under the presence of a magnetic field

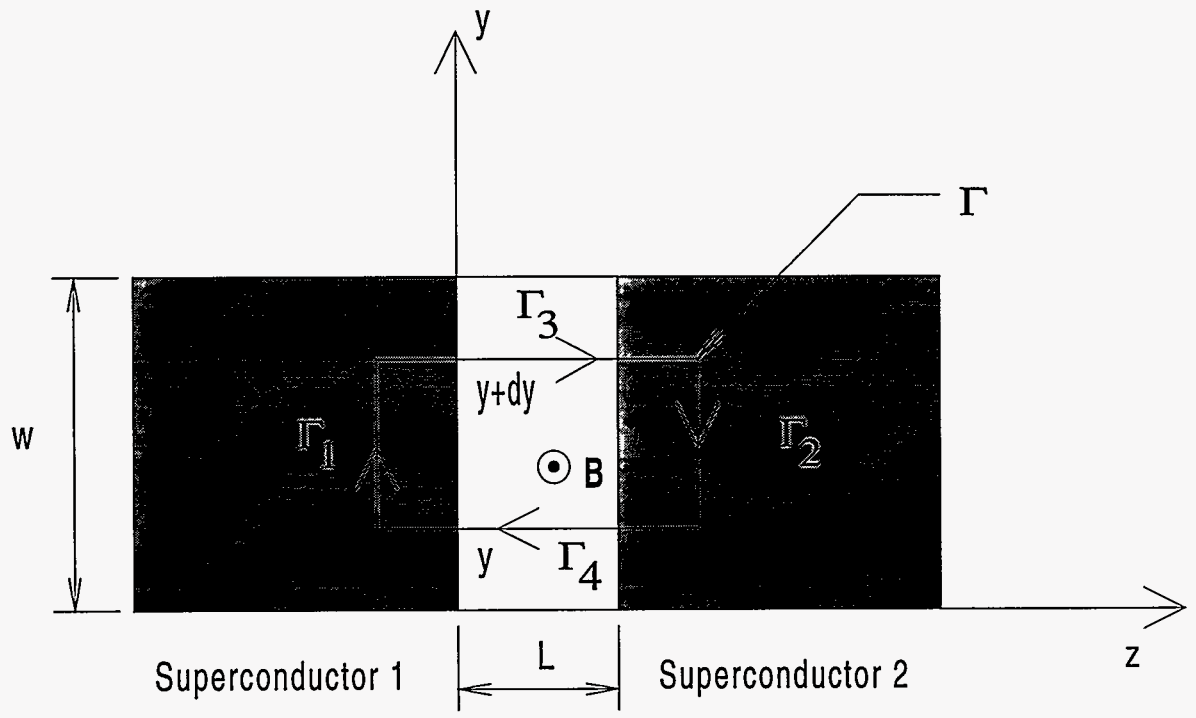

Figure 2.3 Integration path across a Josephson junction

Small junction limit

When Eq. (2.11) is combined with Eqs. (2.3,2.4) and the fourth Maxwell equation, it can be shown [20] that they lead to a sine-Gordon equation of the form:

$$\nabla^2\Delta\theta - \frac{1}{v^2}\frac{\partial^2\Delta\theta}{\partial t^2} = \frac{1}{\lambda_J^2}sin\Delta\theta \tag{2.13}$$

where λ_J is the Josephson penetration depth and is given by

$$\lambda_J^2 = \frac{c\Phi_0}{8\pi^2 d_{eff} J_0} \tag{2.14}$$

In the steady state

$$\nabla^2\Delta\theta = \frac{1}{\lambda_J^2}sin\Delta\theta \tag{2.15}$$

which shows that $\Delta\theta$ varies appreciably over lengths that are comparable to λ_J and that current uniformity in the junction can be achieved only when $w \ll \lambda_J$, where w is the width of the junction. This is known as the small junction limit and all our results will be assumed to lie on this limit. In

practice, the small junction limit can be achieved by increasing the temperature which results in an decrease of J_0. On the other hand, low temperatures are needed in most of our measurements, in order to prevent instabilities due to thermal activation of the vortices. Therefore the temperature where the measurements were taken, was optimized for both current uniformity and vortex stability. For the two samples used in the present work, with ID names MB3-126 and DK5-91, these optimum temperatures were found to be 7.993 and 6.995 K [1] respectively. The Appendix shows the corresponding calculation for the MB3-126 sample. The resulting Josephson supercurrents were less than about 1 mA.

Physical interpretation of Eq. (2.11)

Given the magnetic field distribution in the junction, one can get from Eq. (2.11) the phase difference $\Delta\theta$ and insert it back to Eq. (2.5) in order to derive the current. This procedure will be adopted in subsequent sections in order to get the current-field characteristics for the cases of a uniform external parallel field, a field due to a vortex, and a superimposed field due to two vortices. In this section we follow the argument of Eq. (2.11) and give a physical interpretation which will make it easier to derive $\Delta\theta$ for any field B. Consider a square junction of width w and thickness d_{eff} as in Figure 2.4. Integrating Eq. (2.11) (with L replaced by d_{eff}) along the path PQ

$$\int_{PQ} \nabla_2 \Delta\theta \cdot \mathbf{dl} = \frac{2\pi d_{eff}}{\Phi_0} \int_{PQ} (\mathbf{B} \times \hat{\mathbf{z}}) \cdot \mathbf{dl} \quad . \tag{2.16}$$

and rewriting $(\mathbf{B} \times \hat{\mathbf{z}}) \cdot \mathbf{dl} = \mathbf{B} \cdot (\hat{\mathbf{z}} \times \mathbf{dl})$ leads to

$$\Delta\theta \mid_P^Q = \frac{2\pi d_{eff}}{\Phi_0} \int_{PQ} \mathbf{B_t} dl \tag{2.17}$$

where $\hat{\mathbf{t}} = \hat{\mathbf{z}} \times \mathbf{dl}/|\mathbf{dl}|$ is the unit vector which lies on the x, y plane and is perpendicular to $\mathbf{dl}$ at every point of the PQ curve. Note that the quantity $\Phi_{strip} = d_{eff} \int_{PQ} \mathbf{B_t} dl = \int\int_{strip} \mathbf{B_t} dl dz$ is just the magnetic flux through the strip $PQQ'P'$. Typically the point P is chosen as a reference point and is taken as the origin (0,0), as in Figure 2.5. If the coordinates of point Q are (x, y), then the above result can be written as

$$\Delta\theta(x, y) = \gamma_0 + 2\pi \frac{\Phi(x, y)}{\Phi_0} = \gamma_0 + \Theta(x, y) \tag{2.18}$$

where $\Phi(x, y)$ is the flux through the strip Γ in Figure 2.5, $\gamma_0 = \Delta\theta(0, 0)$ and $\Theta(x, y) = 2\pi\Phi(x, y)/\Phi_0$. Note that if the path Γ is chosen along a field line, the flux through the corresponding strip is zero which means that $\Delta\theta$ is constant and from Eq. (2.5) the current density is also constant. In other words the magnetic field lines in the junction are also equi-current lines.

[1] These two temperatures were initially set to 8.000 and 7.000 K respectively, but there is always some experimental discrepancy in the temperature controller between the programmed set temperature and the real temperature.

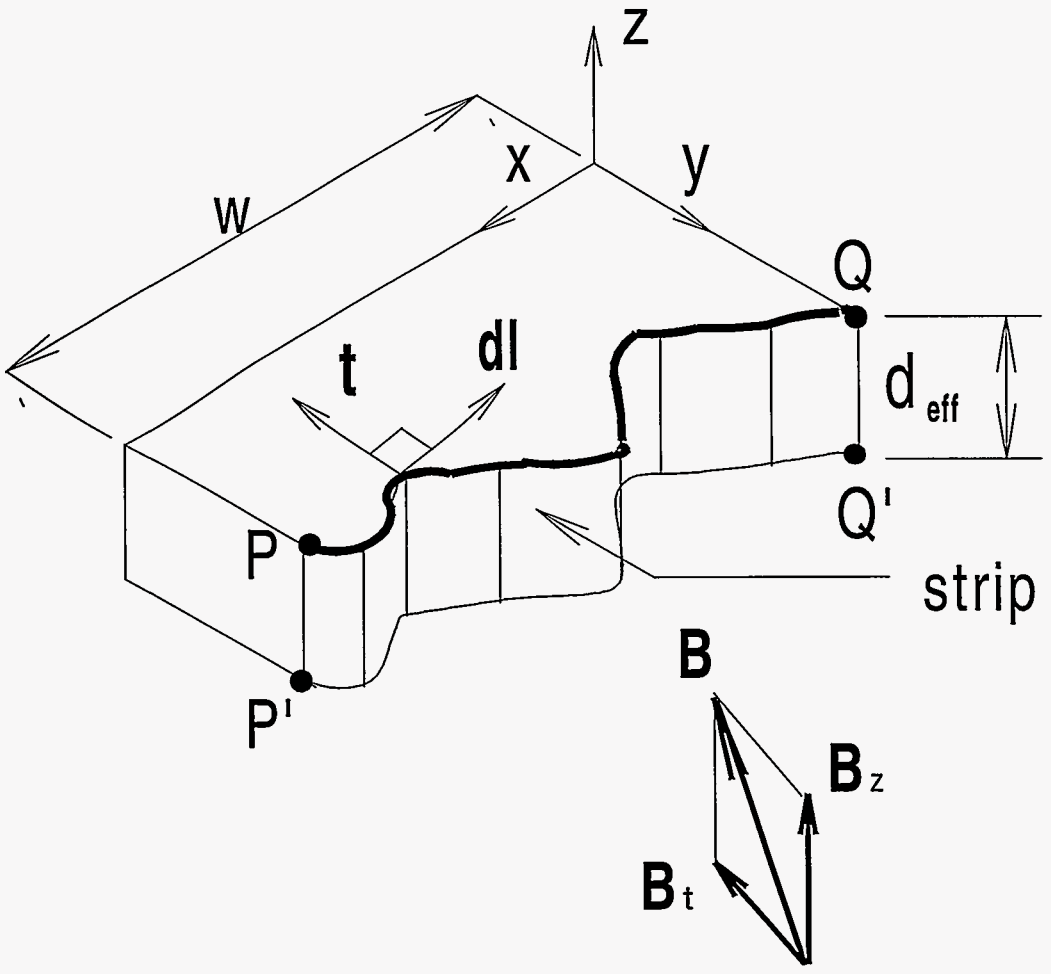

Figure 2.4 Physical interpretation of Eq. (2.11)

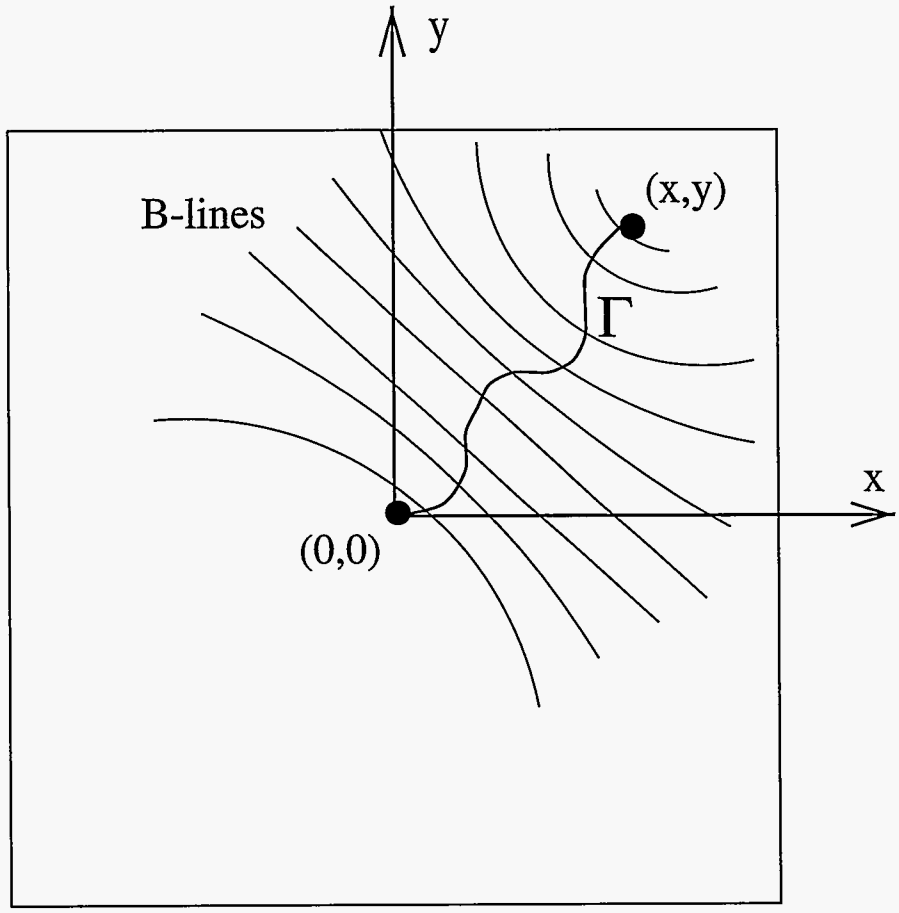

Figure 2.5 Magnetic flux through a strip

Critical current

The total current I across the junction is found by integrating the Josephson current density J over the junction's cross section. Inserting Eq. (2.18) into Eq. (2.5) gives

$$I = \int\int dxdyJ_0 sin\left(\gamma_0 + \Theta(x,y)\right) = sin\gamma_0 I_1 + cos\gamma_0 I_2 \tag{2.19}$$

where $I_1 = J_0 \int\int dxdycos\Theta(x,y)$ and $I_2 = J_0 \int\int dxdysin\Theta(x,y)$. The above expression can be written as

$$I = (I_1, I_2)\cdot(sin\gamma_0, cos\gamma_0) = (I_1^2 + I_2^2)^{1/2}(sin\gamma_0^2 + cos\gamma_0^2)^{1/2} cos\alpha \tag{2.20}$$

where α is the angle between the vectors (I_1, I_2) and $(sin\gamma_0, cos\gamma_0)$. Since by definition the critical current I_c is the maximum current that the junction can sustain without developing a potential difference across it, α has to be set equal to 0 in the last equation to yield I_c. Therefore

$$I_c = (I_1^2 + I_2^2)^{1/2} = I_0\left\{\langle sin\Theta(x,y)\rangle^2 + \langle cos\Theta(x,y)\rangle^2\right\}^{1/2} \tag{2.21}$$

where the brackets denote spatial averaging over the junction area $A = w^2$, and $I_0 = J_0/A$.

External magnetic field parallel to the plane of the junction

In this section an I_c - B curve will be derived for the case of an external magnetic field $\mathbf{B} = B\hat{\mathbf{y}}$ applied parallel to the plane of the junction. An easy path to calculate flux is the straight line Γ shown in Figure 2.6. The flux through the $\Gamma \times d_{eff}$ strip is equal to the flux through the $\Gamma_1 \times d_{eff}$ strip, and its value is given by $\Phi(x,y) = B_y d_{eff} x$. Therefore

$$\Theta(x,y) = 2\pi\frac{B_y x d_{eff}}{\Phi_0} = \pi\frac{B_y}{B_o}x' \tag{2.22}$$

where $B_o = \Phi_0/d_{eff}w$ and x' is the normalized x-coordinate $x' = x/(w/2)$. When this result is inserted in Eq. (2.21), it leads [36] to

$$\frac{I_c}{I_0} = \left|\frac{sin(B_y/B_o)}{B_y/B_o}\right| \tag{2.23}$$

This equation is the same one that produces the familiar Fraunhofer pattern in Optics and a graph of it is given in Figure 2.7. For the rest of this work the symbols x and y will be used without primes to denote the corresponding normalized coordinates $x/(w/2)$ and $y/(w/2)$.

Single vortex

Consider the case shown in Figure 2.8. If a vortex nucleates at the bottom film, there are two cases: The flux lines in the insulating barrier will be shielded by the top superconducting film and excluded

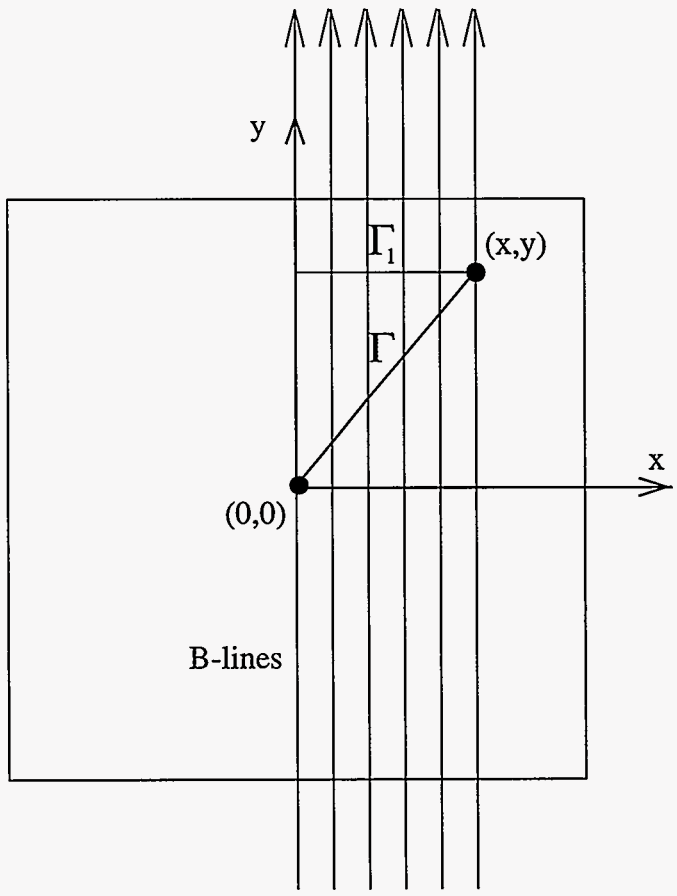

Figure 2.6 Phase due to an external field parallel to the junction

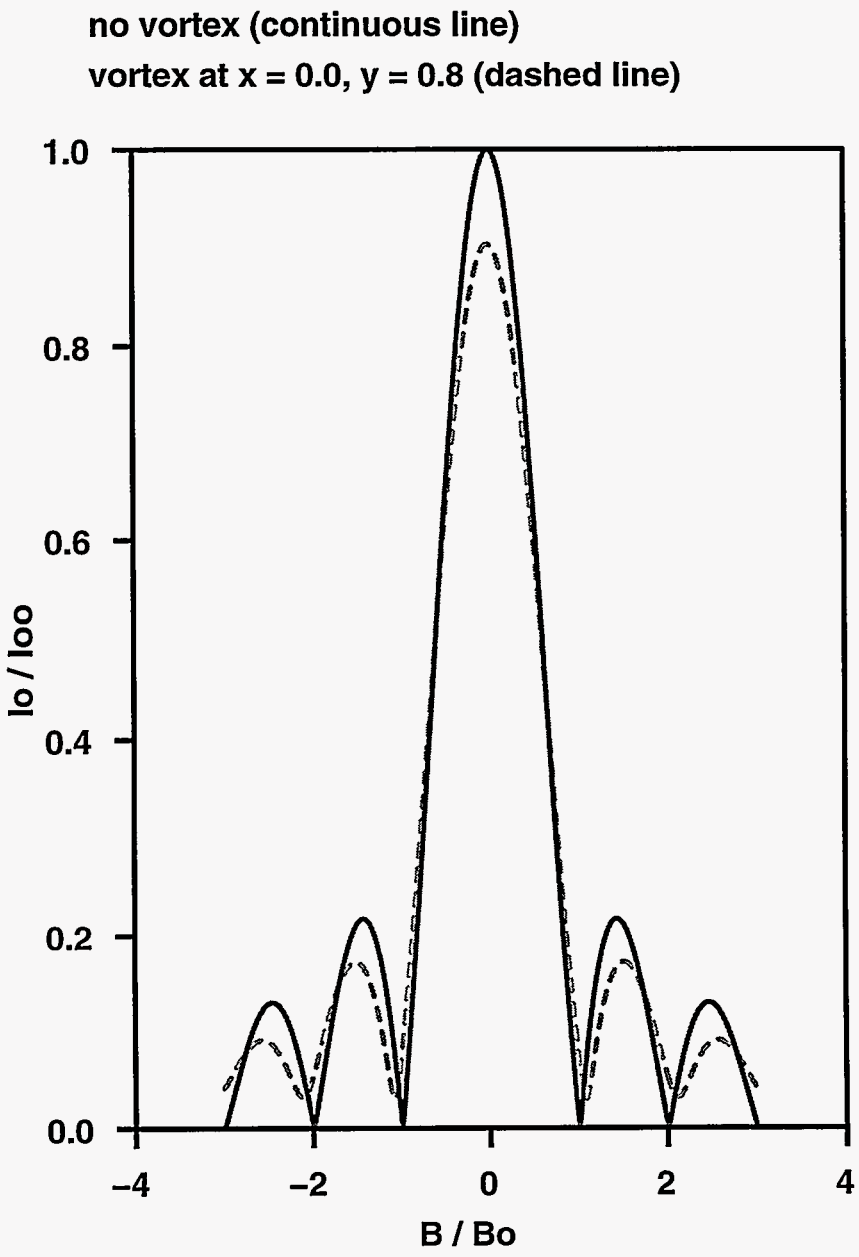

Figure 2.7 Theoretical Fraunhofer diffraction pattern

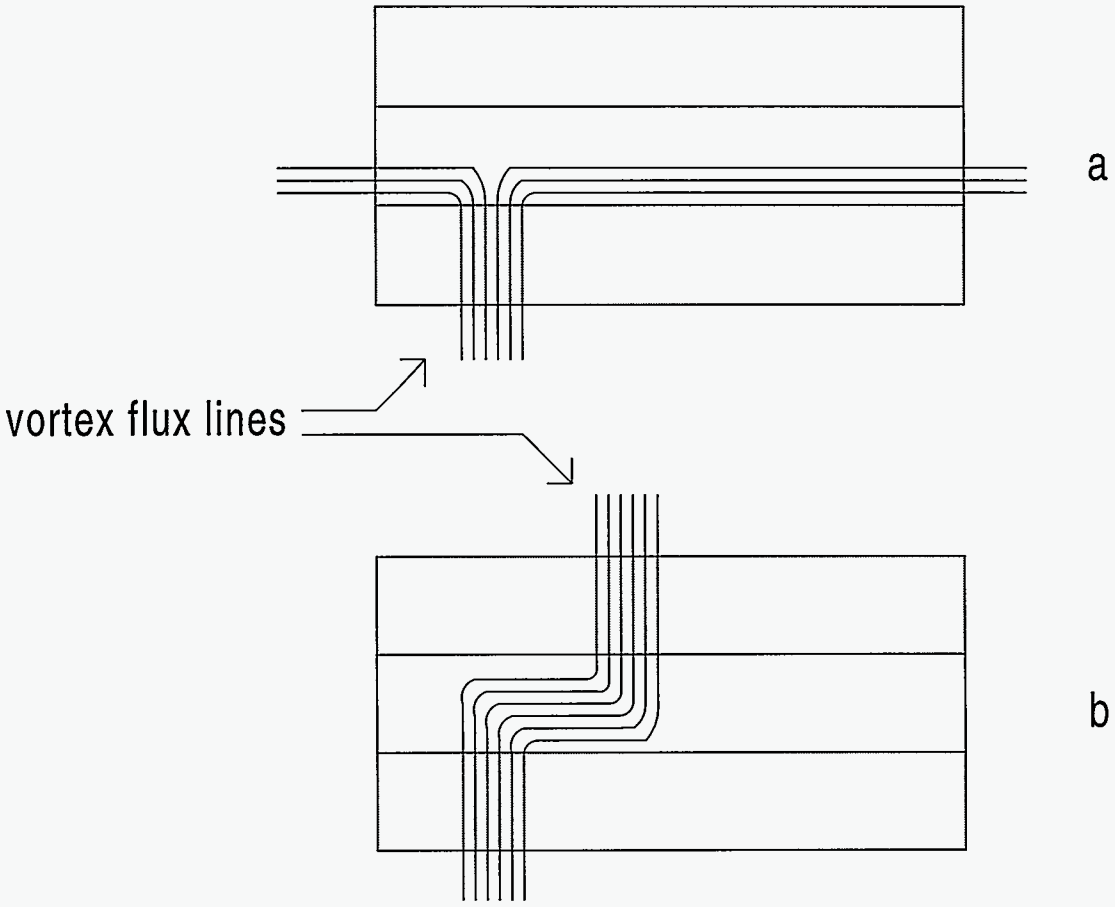

Figure 2.8 Vortex nucleation at the bottom film. The flux lines in the insulating barrier a) are shielded by the top superconducting film and b) they find their way through the top film by means of a second vortex, which in general will be misaligned from the first one

from the junction or they will find their way through the top film by means of a second vortex, which in general will be misaligned from the first one. In the former case we speak of a single vortex while in the latter of a dipole vortex in the barrier. In this section the phase $\Theta(x,y)$ will be derived for the case of a single vortex in the barrier. Figure 2.9 shows the distribution of the flux lines of a positive vortex at (x_0,y_0) in the barrier. By convention, for a positive vortex, the lines emerge out of the page. As in the previous section, the path Γ is chosen to be a straight line. If it assumed that the field lines in the barrier spread out isotropically, then it is easy to see that only a fraction $\gamma/2\pi$ of the quantum of flux Φ_0 of the vortex goes through the stripe $\Gamma \times d$, where $\gamma = \gamma(x,y,x_0,y_0)$ is the angle that the vortex at (x_0,y_0) subtends the points $(0,0)$ and (x,y). Therefore

$$\Phi_+(x,y,x_0,y_0) = \frac{\gamma(x,y,x_0,y_0)}{2\pi}\Phi_0 \tag{2.24}$$

and

$$\Theta_+(x,y,x_0,y_0) = 2\pi\frac{\Phi_+(x,y,x_0,y_0)}{\Phi_0} = \gamma(x,y,x_0,y_0) \tag{2.25}$$

In the case of a negative vortex the flux through the same stripe is negative and so $\Theta_-(x,y,x_0,y_0) = -\gamma(x,y,x_0,y_0)$. It should be noted that in numerical calculations some caution should be exercised when using the function $tan^{-1}(x)$ or $arctan(x)$ to calculate γ because it is only defined within $(-\pi/2,\pi/2)$. When both an external magnetic field and a vortex are present in the junction, the superposition principle states that the two fields and therefore the corresponding phases should be added together. From Eqs. (2.22, 2.25) the combined phase is

$$\Theta(x,y,x_0,y_0) = \pi\frac{B_y}{B_o}x + \gamma(x,y,x_0,y_0) \tag{2.26}$$

So far nothing has been said for the boundary effects due to the finite size of the junction. These effects play little role when the vortex is in the middle of the junction, but a significant role when it is near the edge. Screening currents circulating parallel to the edge of the junction force the magnetic field lines of Figure 2.9 to be perpendicular to the edge [27]. By assuming the vortex to be a magnetic monopole charge, the problem becomes mathematically the same as the 2-D electrostatic problem of a charge in a grounded rectangular box. The charge generates infinite number of image charges outside the box. Moreover, the images distribute all over the x-y plane to form a periodic lattice, as shown schematically in Figure 2.10. Therefore the last equation is to be modified as

$$\Theta(x,y,x_0,y_0) = \pi\frac{B_y}{B_o}x + \gamma(\text{real vortex}) + \gamma(\text{all images}) \tag{2.27}$$

An exact analytical solution for $\Theta(x,y,x_0,y_0)$ from J. Clem can be found in O. Huyn's dissertation [27]. As in the last section, this expression is to be substituted in Eq. (2.21) in order to calculate the critical

current across the junction. The resulting integrations are too complicated to result in an analytical expression and the critical current is calculated numerically. When it comes to computer programming, it is easier to calculate $\Theta(x, y, x_0, y_0)$ by just including a certain number of neighboring image vortices and apply superposition by adding all the phases together.

Two vortices

The procedure of calculating the critical current for the case that there are two vortices present in the junction, is the same as in the last section. By superposition

$$\Theta(x,y) = \pi\frac{B_y}{B_o}x + \gamma(\text{real vortex 1}) + \gamma(\text{all images of 1}) + \gamma(\text{real vortex 2}) + \gamma(\text{all images of 2}) \quad (2.28)$$

As above, the calculation has to be done numerically.

Elementary pinning force

When a current density $\mathbf{J}$ is applied to a superconducting thin film that contains vortices, each vortex feels a Lorentz force per unit length $\mathbf{J} \times \Phi_0/c$, where Φ_0 is a vector parallel to the vortex with magnitude equal to Φ_0 [28]. So far, there has been no general analytical solution available for the transport current density distribution in a thin film. When the penetration length λ is less than the film's thickness d, and in turn this is less than the film's width w however, a useful approximation has been derived [37, 38] for I', the current per unit width of the junction

$$I' = (I/\pi) \cdot [(w/2)^2 - x^2]^{-1/2} \quad (2.29)$$

where x is measured from the film's center and I is the applied current. The Lorentz force in terms of I' is $f = J\Phi_0 d/c = I'\Phi_0/c$. When the current I of Eq. (2.29) is replaced by I^{dep}, the current necessary to depin a vortex, this Lorentz force equals the pinning force and is given by:

$$f_p = (I^{dep}\Phi_0/\pi c) \cdot [(w/2)^2 - x^2]^{-1/2} \quad (2.30)$$

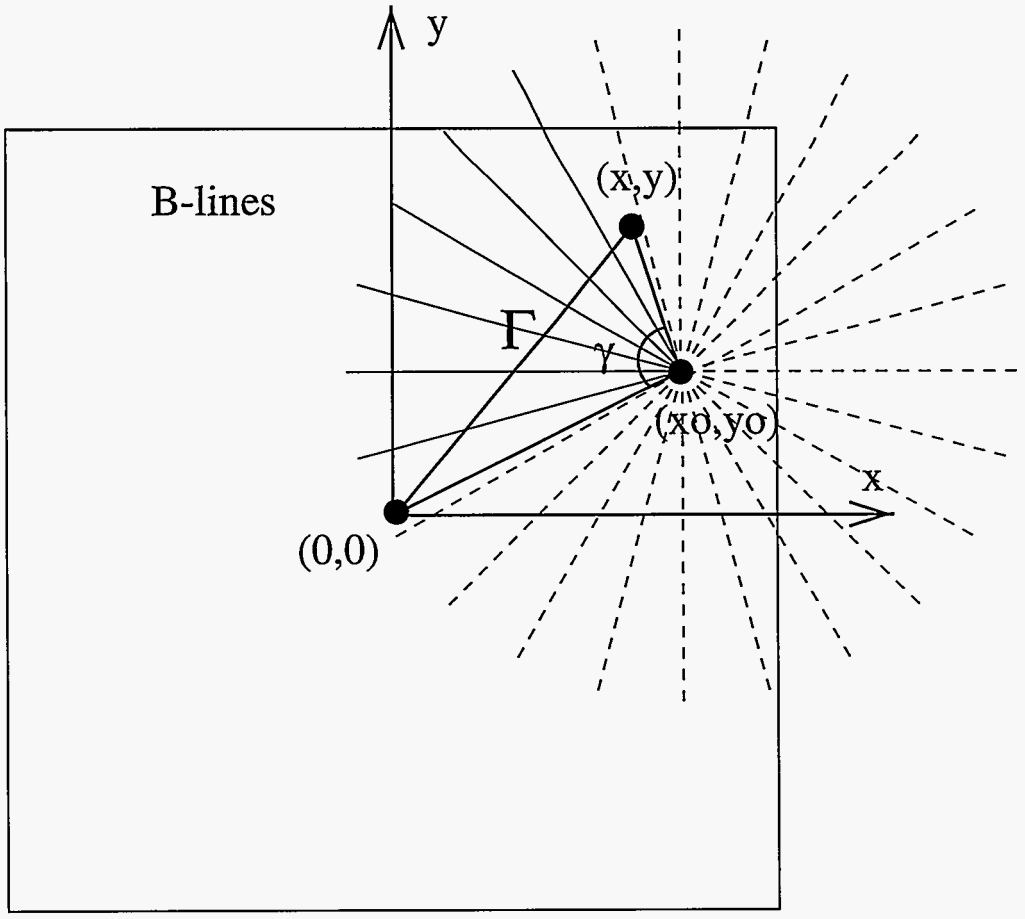

Figure 2.9 Phase due to a single vortex

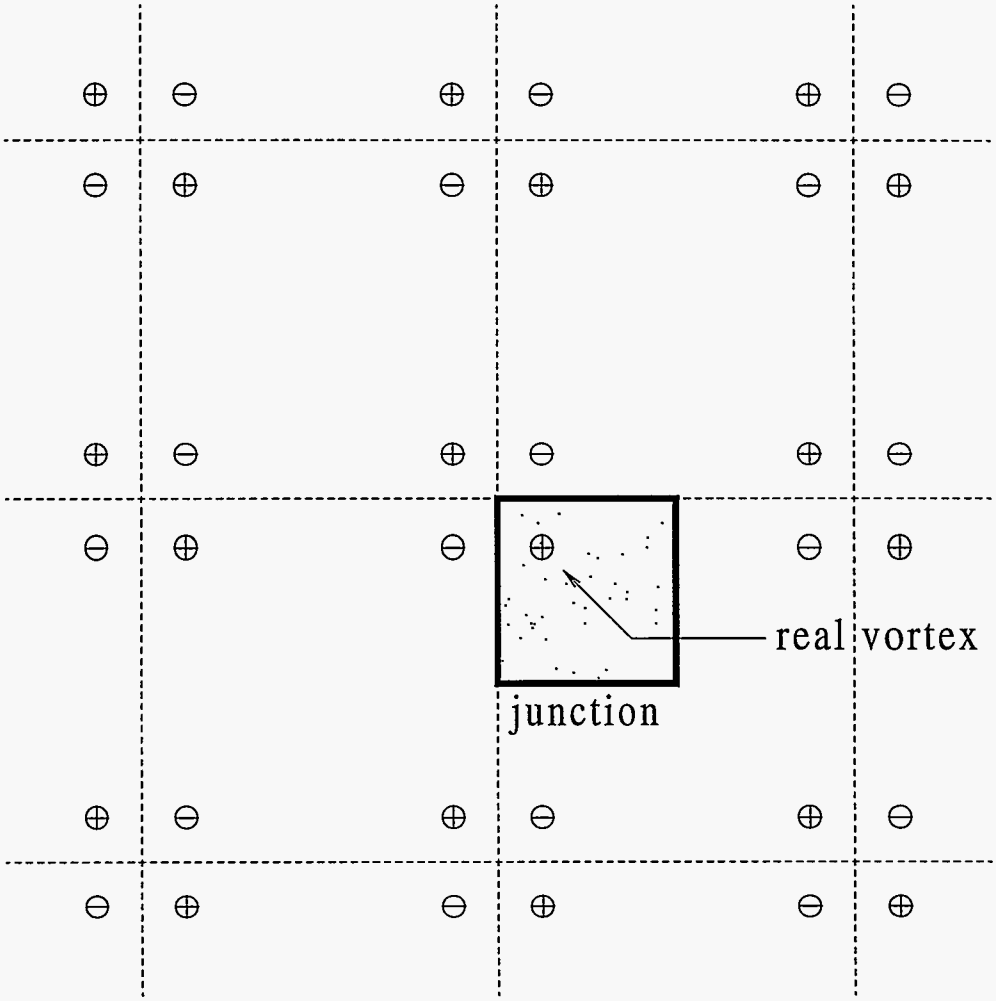

Figure 2.10 Image vortex lattice

3 EXPERIMENTAL TECHNIQUES AND CONDITIONS

Sample preparation

Two SNIS junctions with ID names DK5-91 and MB3-126 were successfully fabricated in a high vacuum sputtering chamber. Both junctions were of the cross type and their composition was Nb-Ag-Al-Al_xO_y-Nb as shown in Figure 3.1.

Each metallic film (including the terminal pads) was deposited by bringing a specially designed mask in contact with the sample and then exposing it to a DC magnetron sputtering source, as in Figure 3.2. Usually the source (or target) is biased with a highly negative potential of several hundred volts with respect to the sample. At the same time a constant Ar gas pressure (10 - 20 mTorr) is maintained within the chamber. Due to the negative potential, electrons are field emitted from the source. A magnetic field caused by the source's magnets forces the electrons to spiral, thus enlarging their path length in the Ar gas and therefore increasing the likelihood of ionizing an Ar atom. The electrons gain kinetic energy due to the electric field and eventually collide with the heavy Ar atoms. The positive Ar atoms that emerge out of the collisions are accelerated by the electric field towards the source and the resulting collision drives material out of the source and towards the sample substrate where it is deposited.

A process known as a glow discharge oxidation was used in order to oxidize the Al layer. During this process, oxygen gas pressure (20-40 mTorr) is maintained in the chamber and an aluminum ring with a diameter of about 4 inches is biased at a high voltage with respect to the chamber ground. This causes a glow discharge which ionizes the oxygen atoms and makes them more reactive resulting in higher oxidation rates. Typical deposition and oxidation parameters for the two samples DK5-91 and MB3-126 are shown in Table 3.1

All the above processes took place in the chamber shown in Figure 3.3. Typically the chamber was evacuated to a base pressure of about 5×10^{-6} Pa (4×10^{-8} Torr) with the aid of a turbo pump and a baking blanket. The sample could be easily inserted into, and removed from the chamber by means of the load-lock mechanism without breaking the high vacuum. The sample also could be easily released in

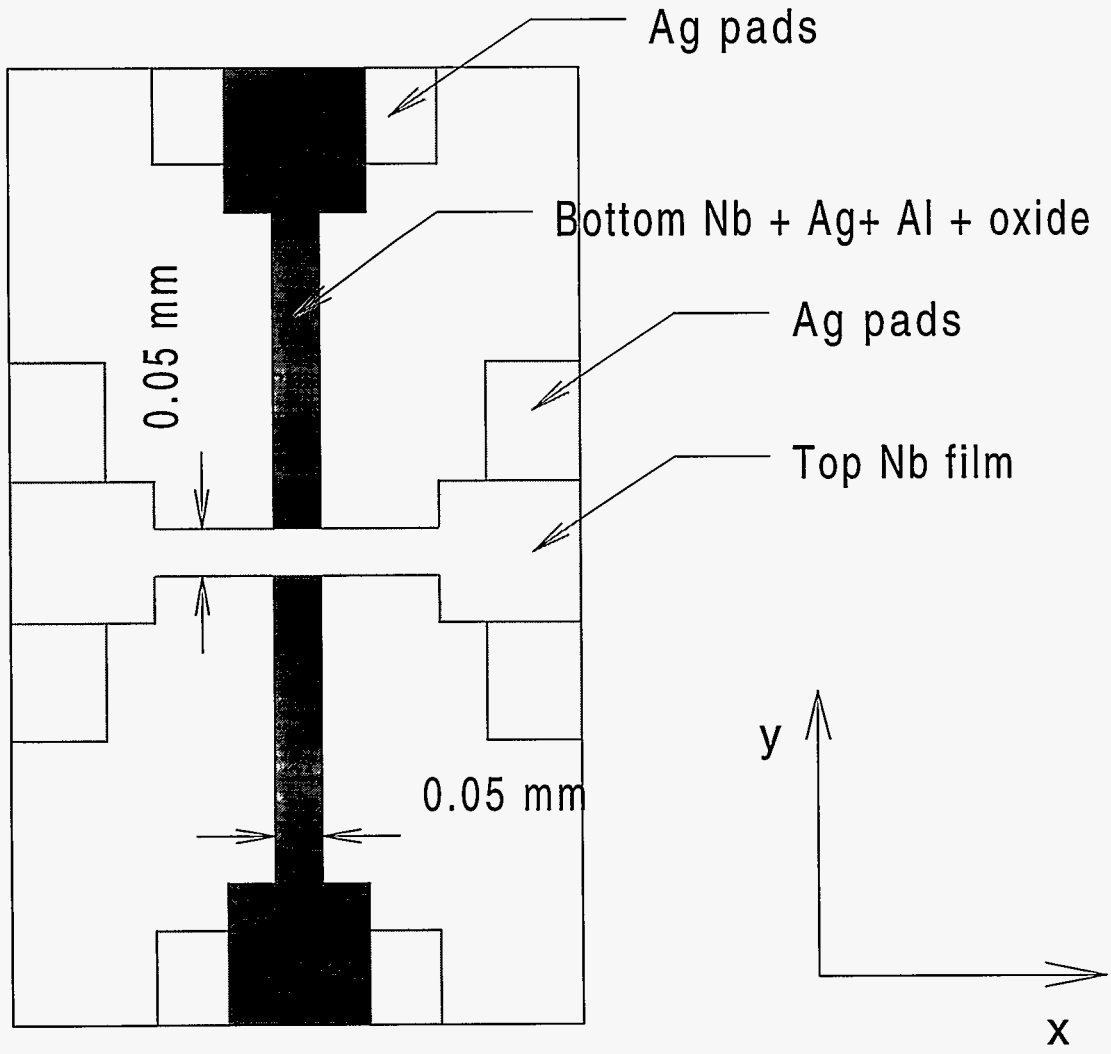

Figure 3.1 Cross type Josephson junction

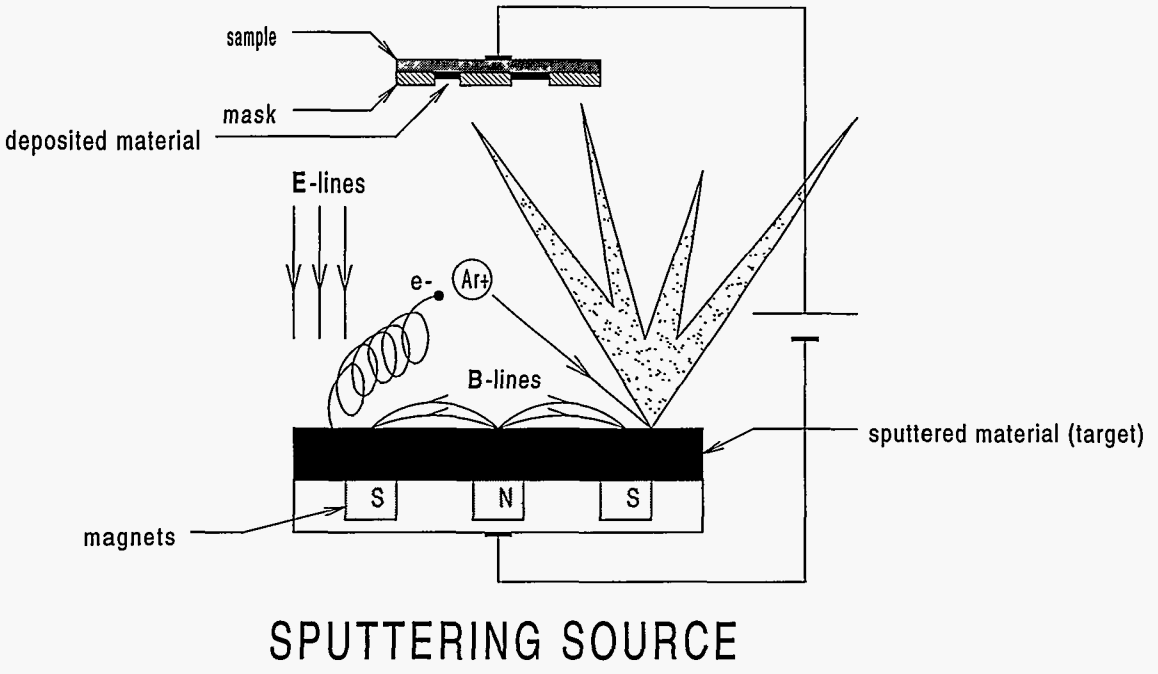

Figure 3.2 The sputtering process

Table 3.1 Deposition and oxidation parameters for the samples DK5-91 and MB3-126

sample	layer	time	P(mTorr)	I(A)	V(V)	rate(Å/s)	t(Å)
MB3-126	Nb	2 h	20 Ar	0.6	225	0.5	4000
	Ag	1 min	5 Ar	0.4	470		~ 3000
	Al	6 min	10 Ar	0.6	400	8.4	3000
	Al_xO_y	80 min	50 O		-500		
	Nb	2 h	20 Ar	0.6	225	0.5	4000
DK5-91	Nb	80 min	20 Ar	0.6	260	0.8	4000
	Ag	1 min	5 Ar	0.4	200		~ 3000
	Al	6 min	10 Ar	0.6	400	8.4	3000
	Al_xO_y	8 min	20 O		-500		
	Nb	1.5 h	20 Ar	0.6	260	0.8	~ 4000

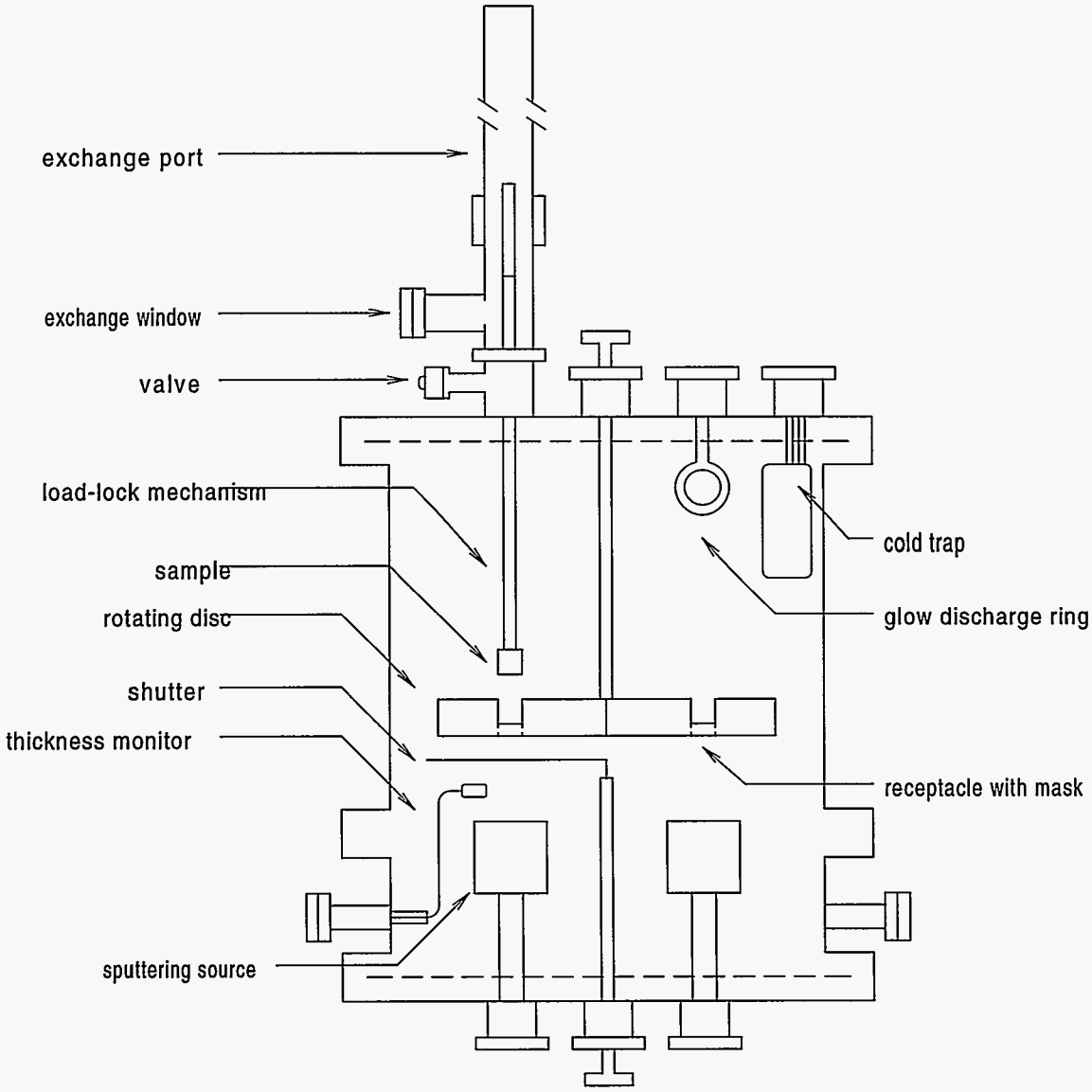

Figure 3.3 The high vacuum sputtering chamber

one of the four receptacles on the rotating disk. The receptacles were symmetrically located 90° apart on the disk and at the bottom of each receptacle there was a mask corresponding to a different film configuration. Once the sample was released in one of the receptacles, the disk was rotated in order to bring the sample above one of the Ag, Al or Nb sputtering sources. Then the source would be turned on with the rotating shutter closed for a period of time in order to clean its surface from any possible surface adsorbants (a process known as presputtering). Deposition would begin when the shutter was open (rotated away). The thickness monitor was located close to the Nb and Al sources enabling a direct in-situ measurement of the Nb and Al thickness.

The deposition procedure of sample MB3-126 follows. Other samples were prepared in a similar way. First an oxidized Si substrate was cleaned by rinsing it with alcohol and blowing it with N_2 gas. The substrate was a piece of a typical single crystal wafer, oxidized and cut along one of its major axes. This substate forms the basis on top of which the various layers are deposited. The substrate was mounted underneath a special holder with the help of a thin smear of Apiezon vacuum grease. Subsequently, the holder was inserted into the exchange port of Figure 3.3 through the exchange window and attached on the lower end of the load-lock mechanism. The exchange port, which was isolated from the chamber by a valve, had to be pumped down to a pressure of less than 500 mTorr before the valve would open. The holder then was safely lowered and inserted in one of the receptacles on the rotating disk. The first layer to be deposited was the bottom Nb. The cold trap was filled with liquid nitrogen in order to trap water vapor and oxygen gas which react very strongly with Nb and thus degrade its superconducting properties. The disk was rotated so as to bring the substrate above the Nb source. The shutter was brought on top of the Nb source and Ar gas would allow to flow into the chamber through a flow modulator which was run by a pressure controller. Then the Nb source was presputtered for at least an hour and then the shutter would be rotated away, allowing thus the Nb flux from the source to reach the sample. Deposition then would take place. Once the desired film thickness was displayed on the thickness monitor controller [1], the source would be turned off and the load-lock would transfer the sample holder to a different receptacle on the disc for the next film to be deposited. The Ag and Al films would follow a similar procedure with the deposition parameters shown in Table 3.1. Also a set of four Ag pads would be deposited as in Figure 3.1 in order to be able later to add contact wires. The next step was the oxidation of the aluminum. Oxygen gas would be inserted into the system through the flow modulator and a negative potential difference (-500 V) would be applied on the Al ring of Figure 3.3 with respect to the chamber's wall. The oxygen ions would react strongly with the Al layer

[1] See Appendix B

on the sample and would form an oxide layer. Unfortunately, there was not any technique available for a direct *in situ* measurement of the oxidation rate. The only information about the quality of the oxide layer, was a resistivity measurement at the end of the deposition process outside the chamber, and so the user had to use his experience and intuition in selecting the oxidation parameters of Table 3.1. After the end of the oxidation process, the chamber as well as the gas lines and flow modulator had to be pumped for prolonged times (2 to 3 hours) to make sure that all the oxygen was removed before the next film would be deposited. The process of depositing the top Nb film was similar to the one followed above for the bottom Nb film.

Cryostat

Once a sample was made, the next step was to insert it into in the cryostat as shown in Figure 3.4. First of all, thin wires (Copper, number 40) were attached to the Ag pads by pressure bonded 0.3-mm-diam In wire. Then the sample was mounted on the Cu block shown in the same figure by applying a thin smear of Apiezon vacuum grease and the Cu wires were soldered on the wire terminals. These wire terminals are wired all the way up to a scanner outside the cryostat without break points in between in order to avoid contact potentials and thermal emfs. On the back of the Cu block at the same height as the sample, there was a calibrated carbon glass resistor (CGR) thermometer (shown underneath the sample in Figure 3.4 for simplicity). Its sole function was to monitor the sample's temperature. A second diode thermometer was mounted close to a resistive heater ($\sim 350\Omega$) and both were connected to a Lake Shore DRC-82C temperature controller. This control circuit was able to maintain a temperature stability of a few millikelvin. The sample and all the above elements were sealed inside the vacuum can which was pumped continuously with a turbomolecular drag pump [2]. The vacuum can was inside the He bath and two orthogonal pairs of Helmholtz coils were attached on it. These coils are made of superconducting Pb wires and their function is to provide a uniform magnetic field either parallel or perpendicular to the plane of the junction. The He bath was thermally isolated from the liquid nitrogen bath by means of the insulating jackets which were evacuated by a mechanical pump. There were two Co-Netic metal cylindrical shields at the bottom of the two baths, surrounding the vacuum can and the coils (not shown in Figure 3.4). Those shields reduced the ambient magnetic field to less than 5 mG and provided the necessary stable magnetic environment and screened out electric and magnetic noise from outside.

[2] See Appendix B

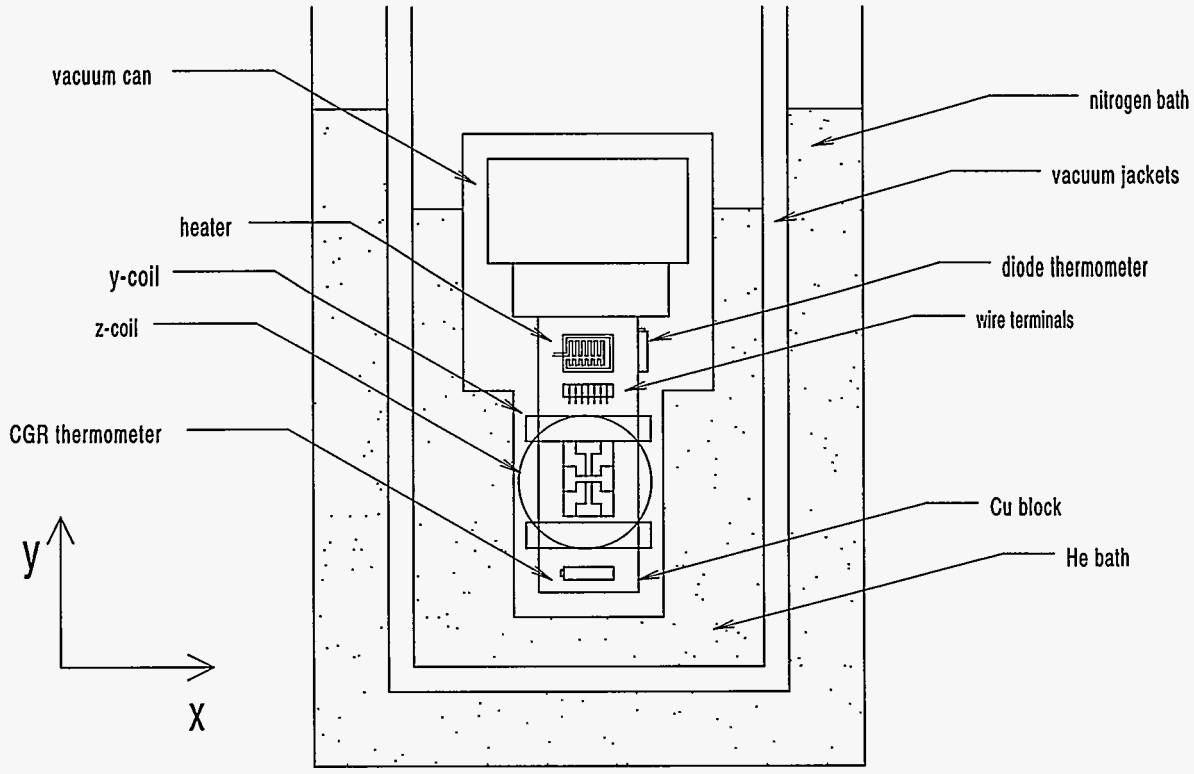

Figure 3.4 The cryostat

Data acquisition

As mentioned above, the junction is connected to the wire terminals 1,2,3,5,6,7 as in Figure 3.5, and these terminals are connected to a current source and a voltmeter through an HP 3495A scanner, which is basically a set of switches. When the number 20 pair of switches is closed, the voltmeter is connected to the junction ends A and C. Below T_c, both the top and the bottom films become superconducting and so a measurement of V_{AC} is a direct measurement of the potential across the junction. Table 3.2 shows the different combinations of switches used for the different measurements. When the number 35 pair of switches is closed, the current flows from point B through the junction to D. This current configuration which is known as "asymmetric feed" has two main disadvantages. On one hand, there are magnetic fields produced by the stripes BO and DO and on the other, the current is not very uniform throughout the square cross section of the junction because current flows through only two of its four sides. The above two problems can be easily overcome by using a "symmetric feed" of currents throughout the junction. It can be achieved by closing two pairs of switches, number 31 and 32. Then positive current enters through points A and B, flows through the junction at O, and returns to the current source through points C and D. There are two benefits of using a symmetric feed of current. First, the current through the junction is more uniform. Second, the magnetic field produced by the two parts of the top (or the bottom) film are opposite in sign and cancel out. Finally, the two pair of switches, number 30 and 33, are used to pass a current through only the bottom or the top film correspondingly. Below T_c, there is no voltage drop along these films but above T_c, the measured voltage V_{AC} divided by the magnitude of the current gives the resistance of the parts AO and CO correspondingly. These resistance measurements are very important in determining the quality of these two films.

Table 3.2 The scanner connections of Fig 3.5 and their functions

pairs of switches closed	current path	T	function
20, 30	A $\rightarrow$ B	$< T_c$	apply I_{bottom}
20, 30	A $\rightarrow$ B	$> T_c$	measure R_{AO}
20, 31, 32	A,B $\rightarrow$ junction $\rightarrow$ C,D	$< T_c$	measure $R_{junction}$, symmetric feed
20, 33	D $\rightarrow$ C	$< T_c$	apply I_{top}
20, 33	D $\rightarrow$ C	$> T_c$	measure R_{CO}
20, 35	B $\rightarrow$ junction $\rightarrow$ D	$< T_c$	measure $R_{junction}$, asymmetric feed

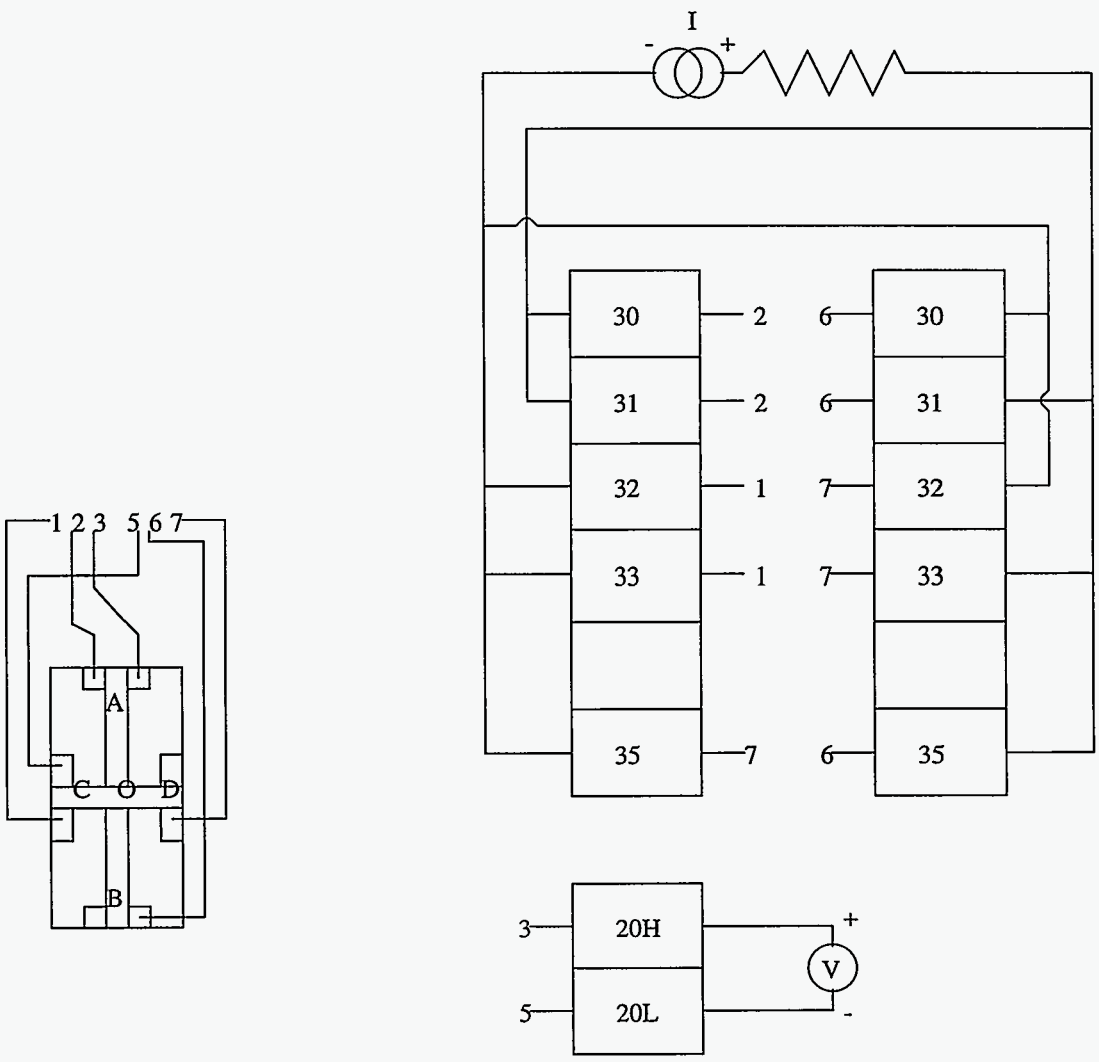

Figure 3.5 The connections to the junction in the cryostat.

4 RESULTS AND DISCUSSION

Resistivity measurements

In all but the last section of this chapter, entitled "Two vortex problem", sample MB3-126 was used exclusively. Figure 4.1 and 4.2 show the resistivity measurements performed on the bottom and top film of this sample respectively. From these graphs it can be inferred that the transition temperatures for the bottom and the top Nb films are $T_c^{bot} = 8.876$ K and $T_c^{top} = 9.314$ K. The latter value may seem a little high compared to the bulk Nb T_c value of 9.25 K, but it is not unusual for Nb thin films to show a T_c of as high as 10.1 K [39]. Both films become superconducting below about 8.9 K but definitely the top film is of better quality because its transition is sharper and its T_c is higher. Note also that in Figure 4.1 it appears as if there are two transitions present. This is probably due to an oxide layer formed on the bottom Nb film during the glow discharge oxidation process by oxygen that diffuses through the Al and Ag barriers. Another contributing factor is the proximity effect that the Ag metal induces into the bottom Nb film.

Figure 4.3 shows a typical $V-I$ curve taken with the voltage V measured across the junction and the current I fed symmetrically in the junction, as was described in the section "Data Acquisition" in chapter 3 above. Although theoretically the critical current I_c is a well defined quantity for SNS junctions, where the resistively shunted junction (RSJ) model applies [40], experimentally it is hard sometimes to determine for these SNIS junctions because the interface conditions are not so well understood. Previous authors in our group [23, 28, 41] have used the method of extrapolating the tangent of the steepest slope to the I axis. This could be done with a relatively high precision because most of their data were of the form of curves taken with a strip recorder. In the present work, the data were digitized, as in Figure 4.3, and so there were only few points to draw the tangent to the steepest slope. Since individual data points are always subject to noise, the method of steepest slope could not be utilized successfully. Instead, a new method was devised for data above 7.0 K which consisted of the following steps:

1. Find the point of the highest voltage V_{max}. All our measurements were taken at the same

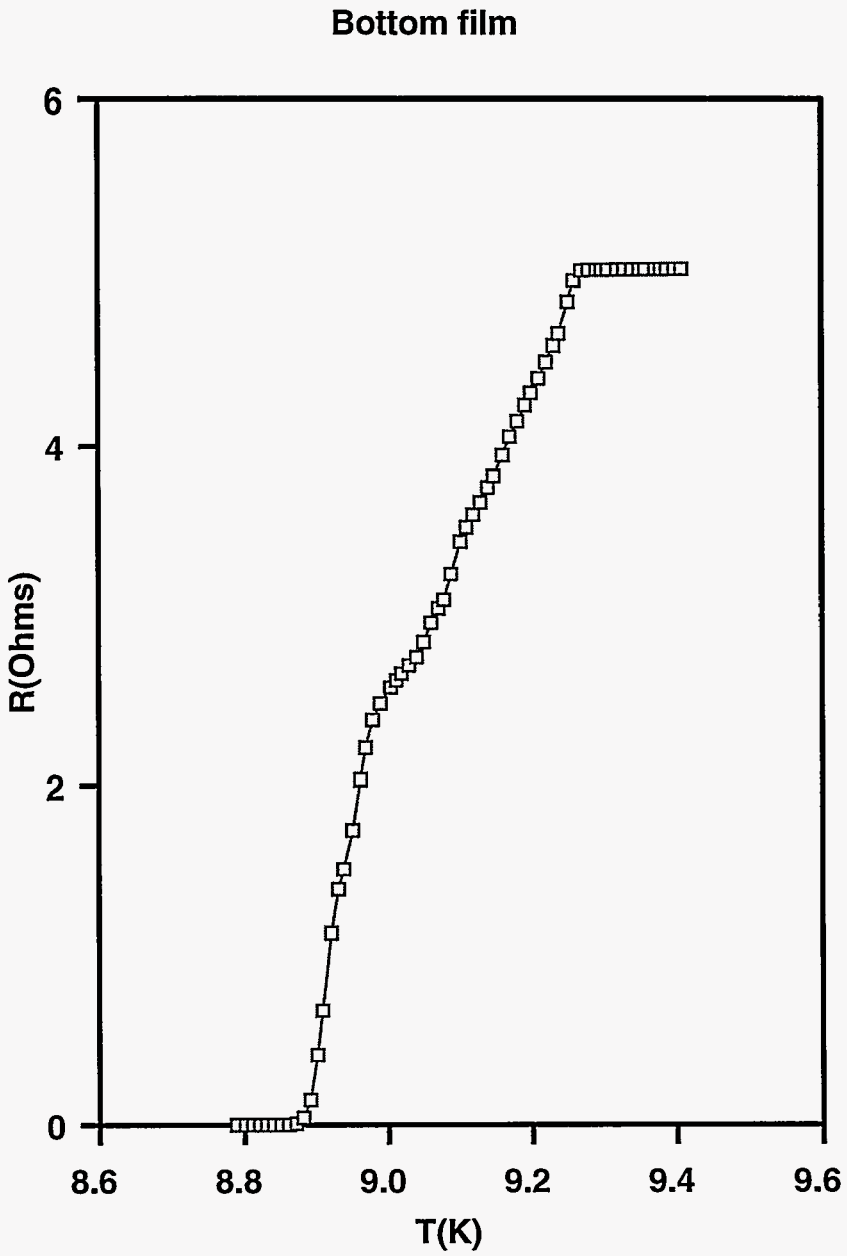

Figure 4.1 Dependence of the bottom film's resistance versus temperature around the transition temperature

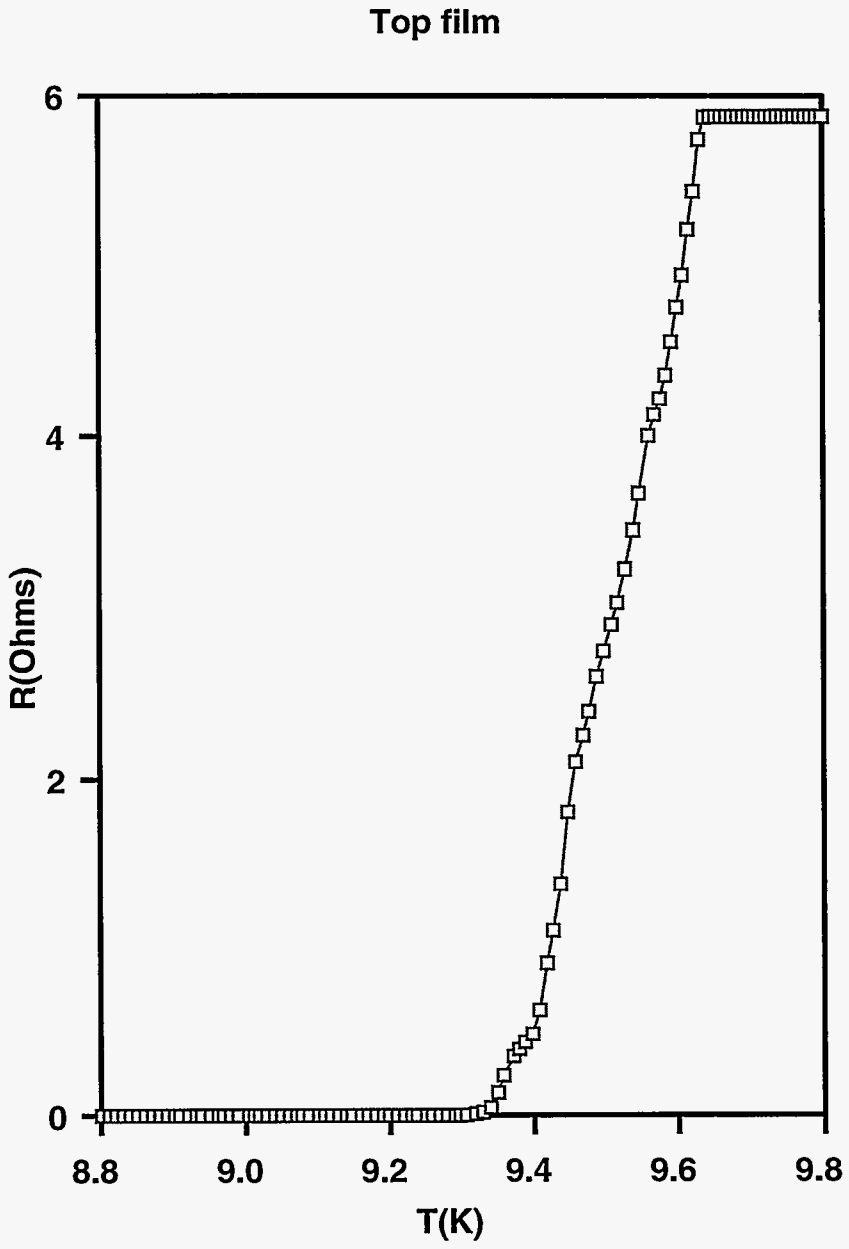

Figure 4.2 Dependence of the top film's resistance versus temperature around the transition temperature

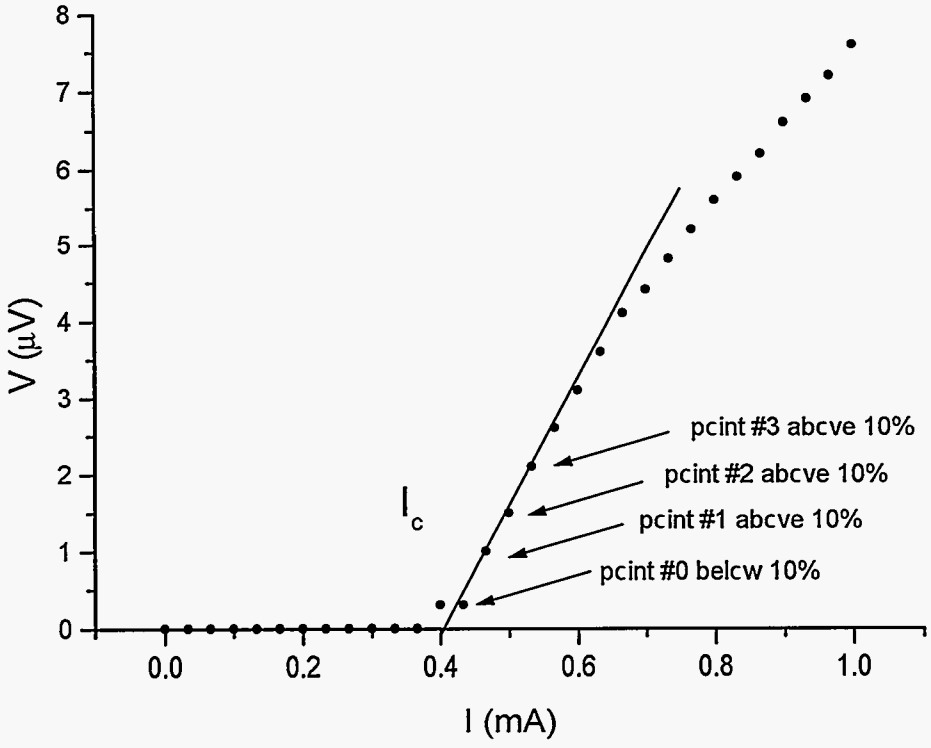

Figure 4.3 Determination of the critical current I_c from the $V - I$ curves

temperature and the same I_{max} and therefore V_{max} was about the same.

2. Pick the first three successive points that are above 10 % of V_{max}, as in Fig 4.3.
3. Draw a least-squares line through these three points and the point before them (point # 0 in the plot).
4. Extrapolate to the I axis to get I_c.

This method was able to give good agreement between theory and experiment as can be seen in the diffraction patterns shown in later sections. In what follows, the symbol I_0 will be used to denote $I_c(B = 0)$, the critical current for the cases where there is no external field applied to the junction.

Using the above method, the dependence of I_0 versus T was determined by a series of $V - I$ curves at various temperatures. The result is shown in Figure 4.4a. From this plot, it is hard to determine the transition temperature of the junction (which in general differs from those of the two films) because the curve has a very small slope near 8.7 K. However, when the same data are plotted on a semi-log graph, it appears to be a sharp transition as in Figure 4.4b. That implies a power law fit of I_0 on T. Trying a function of the form $I_0 = I_0(0)\left(1 - (T/T_c)^{\beta}\right)^{\gamma}$, a very good fit could be obtained with $I_0(0) = 13.16$ mA, $T_c = 8.907$ K, $\beta = 4$, and $\gamma = 3$. The $\beta = 4$ value is rather unusual and it has never being seen in the literature before[28, 41, 42, 43, 44]. Near T_c, the data can be fitted quite well by $(1 - T/T_c)$, $(1 - (T/T_c)^2$, and $(1 - T/T_c)^{3/2}$ for SNS, SIS, and SNIS junctions respectively [28]. The $(1 - (T/T_c)^4)$ dependence may imply some connection to the penetration length λ which varies with temperature as $\lambda(T) = \lambda(0)\left(1 - (T/T_c)^4\right)^{-1/2}$.

Nucleation of a vortex

In order to study the behavior of a single vortex in a junction, a method has to be used that will systematically nucleate a single vortex. Since a vortex is basically a unit of magnetic flux, it means that a sufficiently high magnetic field has to be applied in the junction in order to create enough magnetic energy to overcome the superconducting condensation energy [1]. So far there are three main systematic processes of vortex nucleation:

1. Application of an external uniform magnetic field while cooling the junction through T_c. This process is known as "field cooling nucleation".

[1] See Appendix B

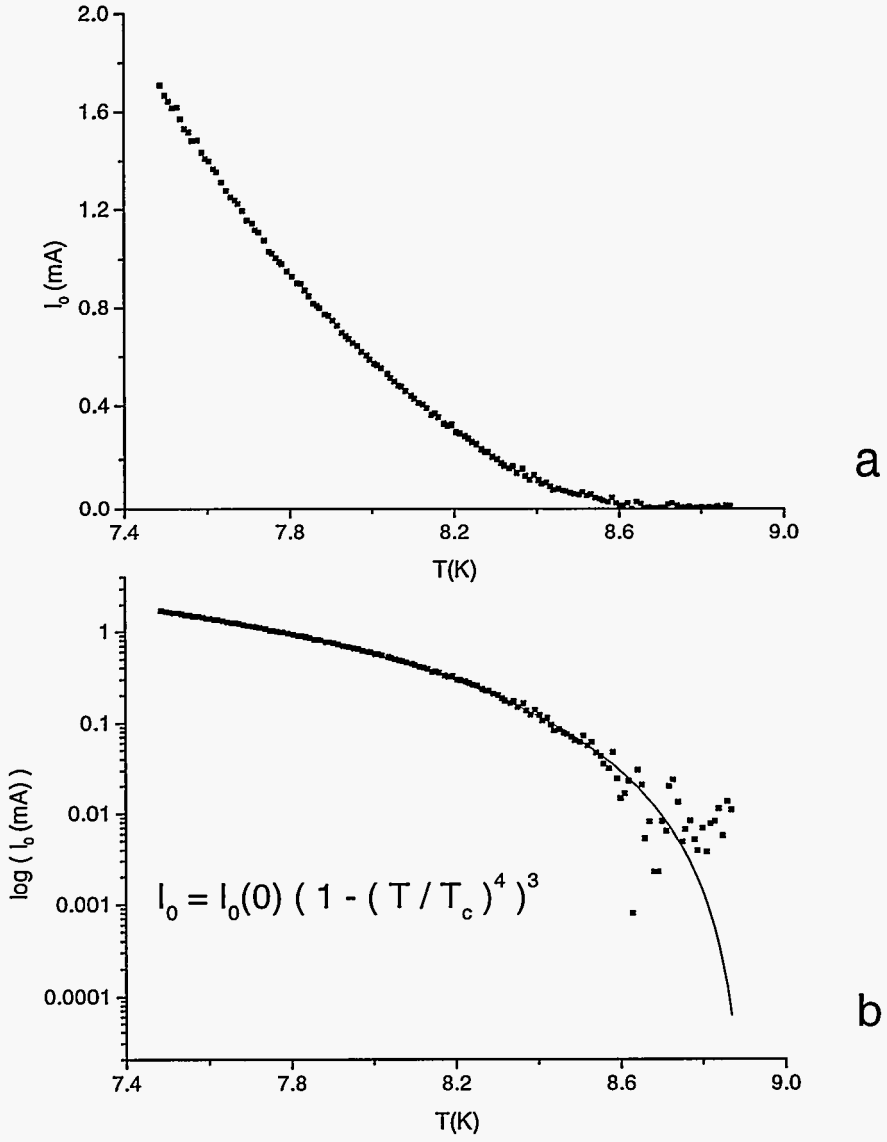

Figure 4.4 Dependence of the junction's critical current versus temperature for a) normal I_0 scale and b) logarithmic I_0 scale. The latter plot reveals the existence of a transition temperature which is in agreement with a transition-type theoretical fit

2. Application of a current through either the top or the bottom film while they are in the superconducting state. These currents generate magnetic fields that are able to nucleate a vortex. This method is known as "transport current nucleation"

3. Cooling through T_c in the presence of stray fields from heater, fore pump etc. Sometimes a vortex will be present in the junction even though all systematic sources of magnetic fields are off. This is because spatial inhomogeneities and defects in the junction tend to trap any stray fields that happen to be around. As the area surrounding the defect becomes superconducting from cooling, the expelled flux tends to accumulate in the defects. When this compressed flux is large enough, it will initiate a vortex.

Usually one or the other method is tried repeatedly in a trial-and-error fashion until a vortex is nucleated. Sometimes, as in step 3 above, one or more vortices will be present in the junction and so nothing has to be done. Normally one measure the" diffraction pattern" [2] in order to determine if a vortex has been nucleated in the junction. There is however, an easier and quicker way to do this. Figure 4.5 shows a theoretical calculation of I_0, the critical current of a diffraction pattern for zero field, along the x-axis. It is obvious that $I_0(x)$, where x is the position of a single vortex along the x-axis, is a very smooth, monotonically increasing function of x, with I_0 tending to zero close to $x = 0$, the center of the junction. That implies that a simple $V - I$ measurement followed by a determination of the critical current is usually a sufficient indication of the presence of one or more vortices in the junction. A plot along other axis shows a similar behavior.

Determination of I_{00} and B_0

The experimental diffraction patterns which are of the form "I_c versus B" have to be normalized into "I_c/I_{00} versus B/B_0" in order to be compared to the theoretical diffraction patterns, where I_{00} is the critical current at zero field and B_0 is the field of the first minimum in the non-vortex diffraction pattern. In practice it is difficult to measure directly these two quantities because one is never sure whether a particular diffraction pattern is the non-vortex one or not. This is because the diffraction patterns for the case of a junction without any vortices present (vortex-free junction) and a junction with a vortex close to its edge, are barely distinguishable. Consider for example the case of a vortex at $x = 0.0$, $y = 0.8$ in Figure 2.7. Its only difference from the non-vortex Fraunhofer diffraction pattern is that its maximum is about 15% lower. An easier way to determine I_{00} and B_0 with a relatively good

[2] See Appendix B

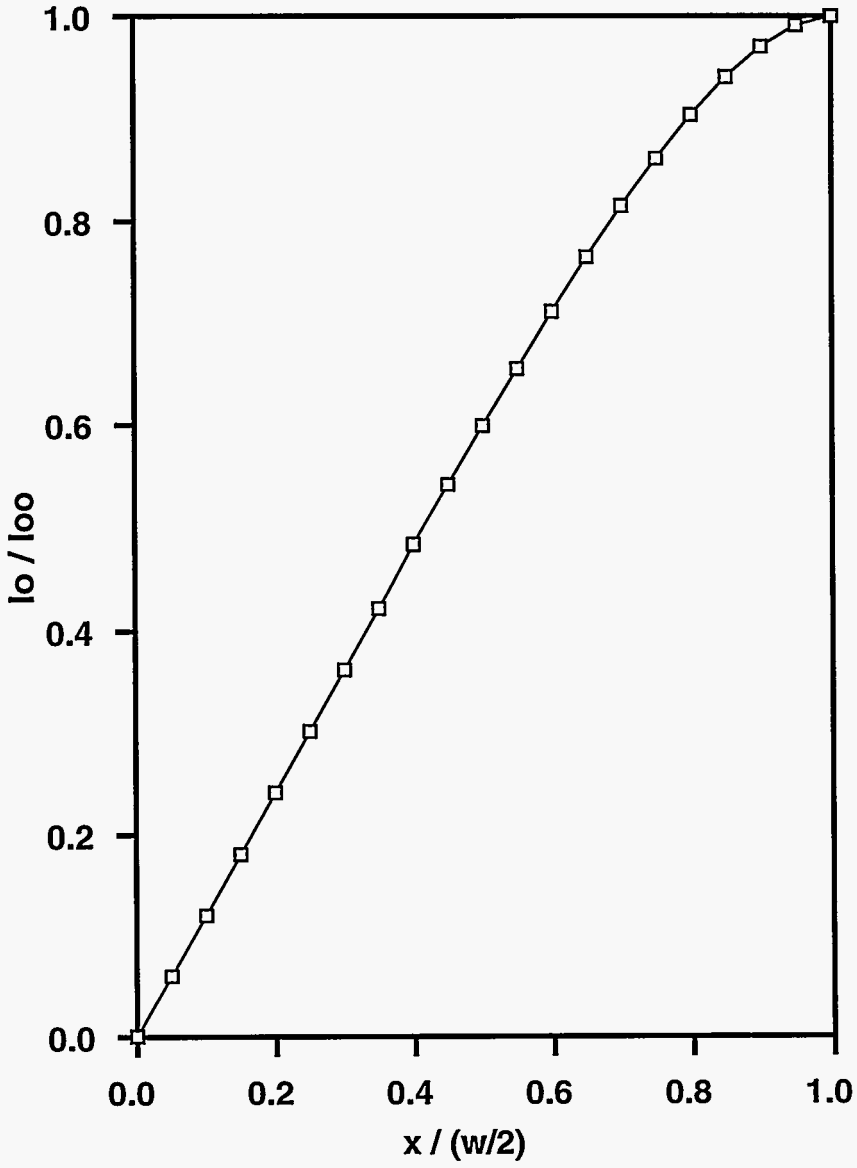

Figure 4.5 Theoretical calculation of I_0/I_{00} for vortex position along the x-axis of the junction

precision is to look at a one-vortex diffraction pattern with a rather unique shape and compare it to the theory. In the present work the diffraction pattern shown in Figure 4.6a was chosen for this purpose. It was taken after a field of B_z = -8 mG was applied while cooling the junction from 10.5 K (higher than $T_c \sim 9.0$ K) down to 7.993 K in 200 steps of 1 second each (field cooling method). Its "M-type" shape is characteristic of a one-vortex diffraction pattern. Our theoretical diffraction patterns are calculated with a vortex position accuracy of 0.05. Within this accuracy, there are about twenty distinguishable "M-type" diffraction patterns to compare with only a few with the two maxima being equal. Among these, the one shown in Figure 4.6b had the closest minimum-to-maximum-peak-ratio to the one in Figure 4.6a. Comparing these two diffraction patterns, I_{00} and B_0 were easily determined to be 759 μA and 357 mG correspondingly. Additionally, it was noted that the pattern of Figure 4.6a was not centered around $B = 0$ G as the one in Figure 4.6b, which probably means that there was a small magnetic field background of 60 mG present in the experimental apparatus even when all the coils were off. Although this field is small, it is still significant for the purpose of the present experiment and so a new piece of Co-Netic shield was added to the system after this diffraction pattern was taken. This new shield was able to keep the background magnetic field to a level of about 5 mG. It should be noted that our measured diffraction patterns had to be shifted appropriately in order to account for this offset field.

Depinning current versus temperature through the bottom film

Once a vortex is nucleated in the junction, it is usually "pinned" at one of the "pinning sites" [3] and unless some external energy is supplied to it, it will probably remain there, providing the temperature is low enough. The magnetic field of the vortex exerts a Lorentz force on any currents that happen to be around it. From the action-reaction principle these currents exert an equal and opposite Lorentz force on the vortex. This principle is utilized in the present work by applying a current I_p through the bottom film at different temperatures in order to measure the depinning current I_p^{dep}, the current that first "depins" [4] the vortex, versus temperature. Once I_p was applied at a given temperature, the system was brought down to a lower reference temperature 7.993 K in order to measure the $V - I$ curves. The reasons for choosing 7.993 K are explained in the discussion following Eq. (2.15). The experiment to measure I_p^{dep} at a particular temperature consisted of the following steps:

1. Nucleate a vortex and bring the system to the reference temperature of 7.993 K.

[3] See Appendix B
[4] See Appendix B

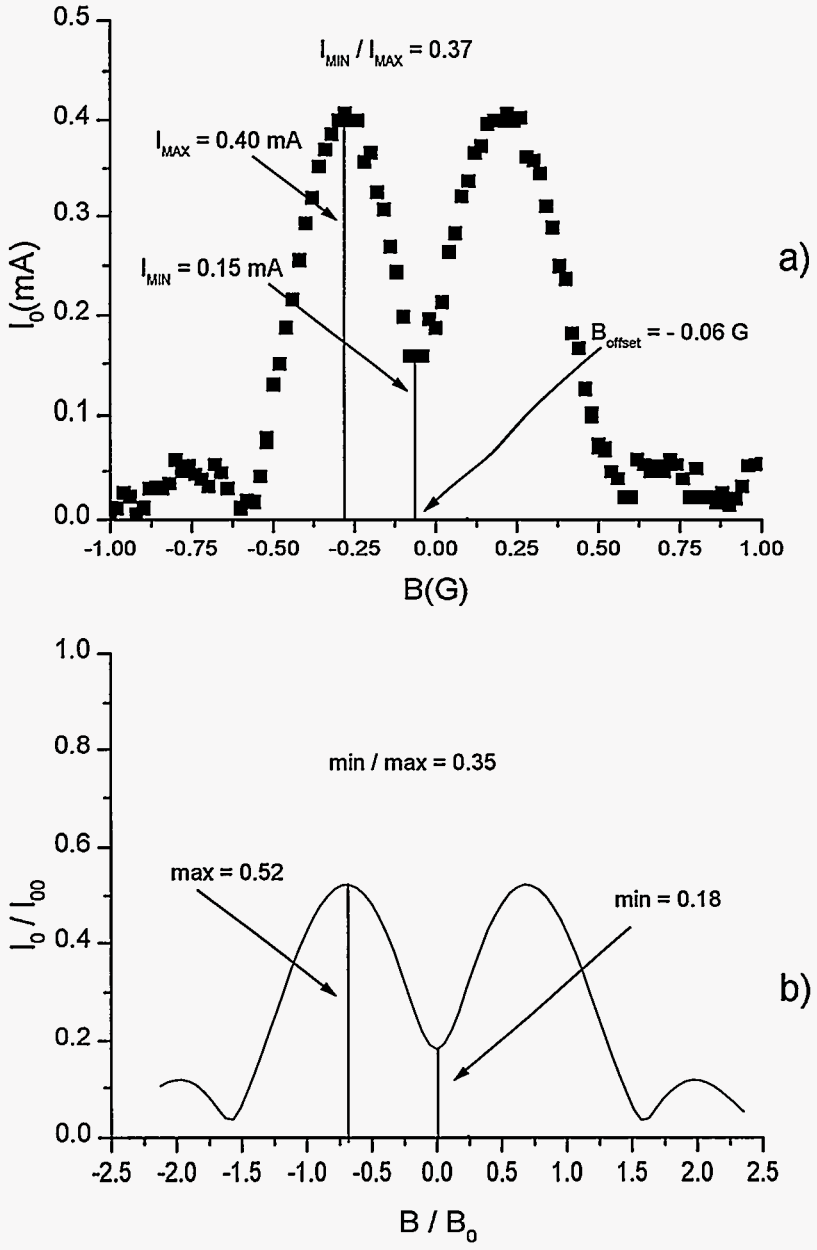

Figure 4.6 Determination of I_{00} and B_0 by comparing a) a measured diffraction pattern of a rather unique shape with b) a theoretical diffraction pattern with similar properties

2. Take a $V - I$ curve in order to verify that there is a vortex present in the junction.

3. Warm up to the desired temperature in 25 steps of 1 second each.

4. Measure the temperature. Name this temperature T_p.

5. Apply I_p through the bottom film for 5 seconds.

6. Decrease the temperature to the reference temperature with the same rate used in step 2 above.

7. Take a $V - I$ curve and determine I_0.

8. Plot the (I_p, I_0) pair on a graph.

9. Repeat steps 2-7 above with slightly higher I_p.

Figure 4.7 shows a plot of I_0 versus I_p that was taken according to the above procedure at $T_p = 8.158$ K. The sample was first cooled from 10.5 K (higher than $T_c \sim 9.0$ K) down to 7.993 K in 100 steps of 1 second each and a $V - I$ was taken in order to determine if there was a vortex trapped in the junction. Since $I_0 \sim 650\mu$A (first point of Figure 4.7) was significantly smaller than the theoretical value of $I_{00} = 759\mu$A (calculated in the last section), it was inferred that there was a trapped vortex near the edge of the junction. Each value of I_0 in Figure 4.7 was determined by a separate $V - I$ measurement as the inset shows. It is apparent that there is a flat portion on the $I_0 - I_p$ curve where the vortex is pinned and the Lorentz force is smaller that the pinning force. At higher currents the vortex starts to move but the steps are rather continuous and it is difficult to extract the I_p^{dep} from the graph. This result is in contrast with measurements done in Pb-based junctions which have a step-like behavior at the depinning current [27, 28]. As was mentioned above, there is some noise on our $V - I$ curves and therefore there is some uncertainty in determining I_0 precisely. In order to extract I_p^{dep} the quantity

$$s = \sum_{i=1}^{N} (V(i) - V_0(i))^2 \tag{4.1}$$

was plotted versus I_p as in Figure 4.8. In this expression, $V(i)$ is the set of measured voltages for each data point of Figure 4.7 and $V_0(i)$ the corresponding set for $I_p = 0$. From now on s will be referred as the "sum of the square differences". It is clear that the plot of Figure 4.8 provides a better evidence that the vortex was initially pinned until some current I_p^{dep} was reached. Also in this plot the depinning occurs continuously and so a criterion is needed to determine I_p^{dep}. The criterion was that I_p^{dep} is the current when first $s = 0.01$, as it is shown in the figure.

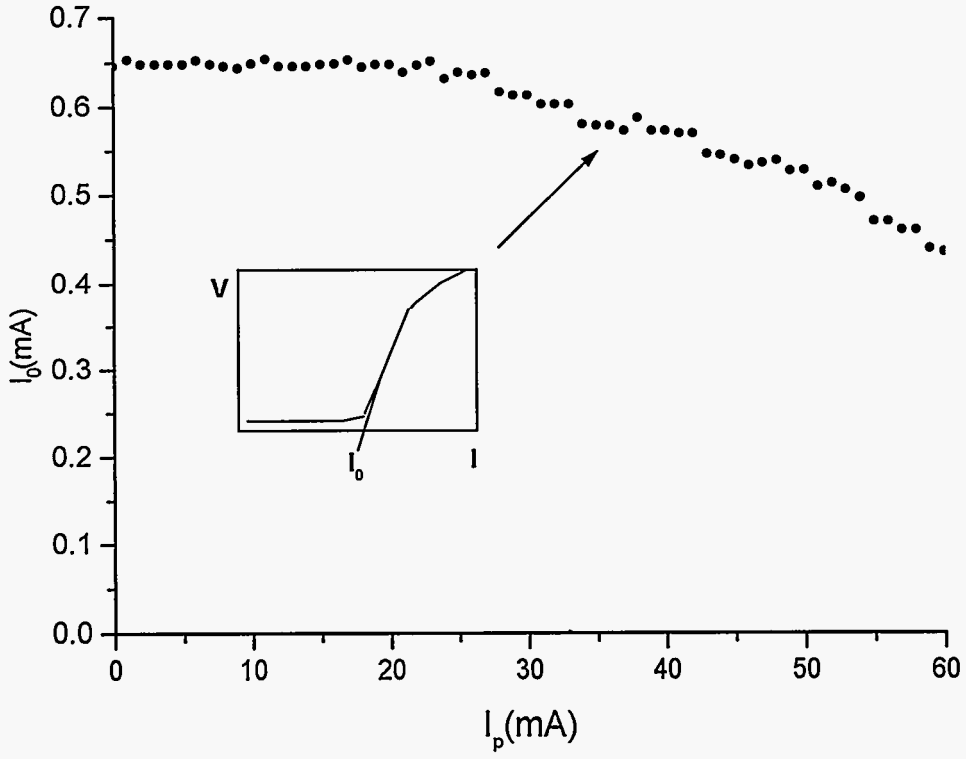

Figure 4.7 Dependence of the critical current on the transport current I_p, applied through the bottom film at $T_p = 8.158$ K. The inset indicates that every point on the graph corresponds to a different $V - I$ measurement with I_0 determined as in Figure 4.3

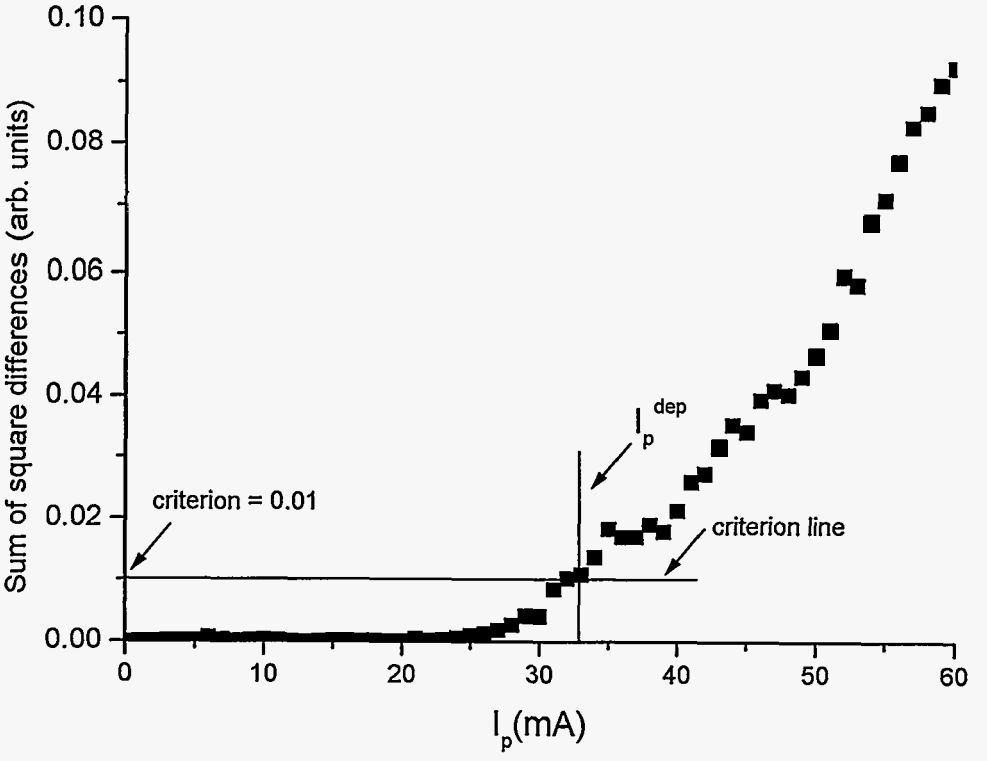

Figure 4.8 Dependence of the sum of the square differences on the transport current I_p applied through the bottom film at $T_p = 8.158$ K

The procedure described in the last paragraph was repeated for several temperatures, as in Figure 4.9a where curves for only 6 different temperatures are shown for clarity. In order to ensure similar, if not identical initial conditions, the sample was warmed above, and cooled through T_c as above. Surprisingly, values close to 650μA were always obtained for I_0 at $I_p = 0$. Using the aforementioned criterion $s = 0.01$, I_p^{dep} could be determined for a wide range of temperatures and a plot of it is shown in Figure 4.9b. These points seem to lie on a straight line, described by the equation

$$I_p^{dep}(mA) = -71.2T_p(K) + 615.9 \tag{4.2}$$

which extrapolates to $I_p^{dep} = 0$ mA for $T_p(K) = 8.650$ K.

From the above results, the pinning force as a function of temperature can be calculated as follows: As it was mentioned in the last paragraph, $I_0 \sim 650\mu$A after vortex nucleation. With $I_{00} = 759\mu$A calculated above, I_0/I_{00} is about 0.85 which from Figure 4.5 implies that the vortex was approximately at $x/(w/2) = 0.75$. When this result is inserted in Eq. (2.30), it gives

$$f_p = 3.024\frac{I_p^{dep}(T)\Phi_0}{\pi c w} \tag{4.3}$$

in Gaussian units. As Appendix shows, this equation can be written in practical units as

$$f_p(\mathrm{N}) = 4.00 \times 10^{-11}\mathrm{I_p^{dep}(A)} \tag{4.4}$$

where the value $w = 50\mu$m was used for the film's width. Converting amperes to milliamperes and substituting I_p^{dep} from Eq. (4.2) leads to

$$f_p(\mathrm{N}) = (-285\mathrm{T_p(K)} + 2464) \times 10^{-14} \tag{4.5}$$

For example $f_p = 1.84 \times 10^{-12}$ and 0.42×10^{-12} N for $T = 8.0$ and 8.5 K respectively. These values are very close to the ones found by O. B. Hyun [27] and Qiang Li[28].

Field cooling process

It is interesting to know what the effects of an applied B_z field are during the field-cooling process because as it was mentioned above, this process is used to nucleate a vortex.

The following steps were followed during this experiment:

1. Warm the sample to 10.5 K (higher than T_c of both films).

2. Stay there for 10 seconds in order to reach thermal equilibrium.

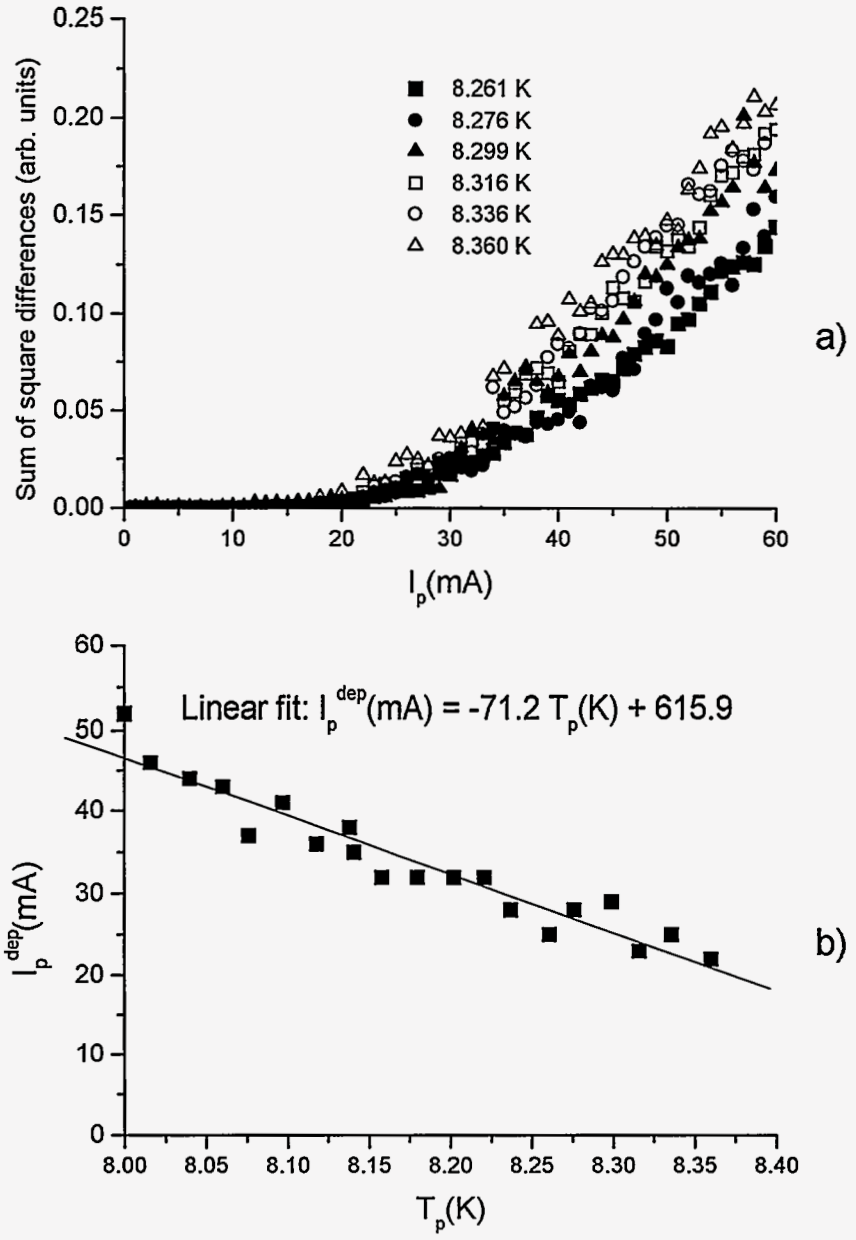

Figure 4.9 Determination of the depinning current for different temperatures: a) a family of curves like the one in Figure 4.8 and b) the corresponding I_p^{dep} extracted from these curves. Only data for a few temperatures are shown in the former plot for clarity

3. Apply the desired B_z.

4. Cool the sample to the referenced temperature of 7.994 K in 100 steps of 1 second each.

5. Turn the B_z field off.

6. Take a $V - I$ curve and determine I_0.

7. Plot the (B_z, I_0) pair on a graph.

8. Repeat steps 1-6 above with slightly higher B_z.

Figure 4.10 shows a plot of I_0 versus B_z that was taken according to the above procedure. The initial purpose of the experiment was to start with a vortex-free junction and observe what is going to happen as B_z increases. Unfortunately, a vortex was present even at zero applied field, at point "A" of Figure 4.10, as Figure 4.11 shows. Since it is generally hard to have a vortex-free junction, it was decided to continue the experiment anyway. Other than the point "A" above, three more diffraction patterns were taken during this run, indicated by "B", "C", and "D" on Figure 4.10 and shown in Figure 4.11. It can be seen from the theoretical fits, shown by the solid lines, that each of the points "A", "B", and "C" represent a different single vortex, as every step in Figure 4.11 involves warming above T_c. It is quite interesting that the vortices "A" and "B" that correspond to $B_z = 0$ and 20 mG, were nucleated very close to each other, at positions (0.40, 0.70) and (0.45, 0.75) respectively. Further increase of the magnetic field to 40 mG at point "C", resulted in a nucleation of a vortex which was closer to the junction's center than "A" and "B". This is the reason why the curve of Figure 4.10 is declining around this region. Point "C" was the single vortex limit for B_z. Diffraction patterns taken above 40 mG could not be fitted successfully with one-vortex patterns. As more and more vortices kept being nucleated in the junction, the diffraction patterns looked more and more suppressed and without any interference minima present, as in the pattern of point "D" in Figure 4.11. The solid line in this figure shows the best one-vortex theoretical fit to these data, which is obviously very poor. It appears from Figure 4.10 that the range of B_z shown between the I_0 axis and the first separation line is an appropriate range for thermal depinning experiments since variations of B_z there do not result in dramatic changes of I_0.

Thermal depinning in the absence of an applied field

Another way to depin a vortex is by supplying thermal energy to it. As the temperature rises, the superconducting pair potential decreases and the thermal energy becomes comparable to the pinning

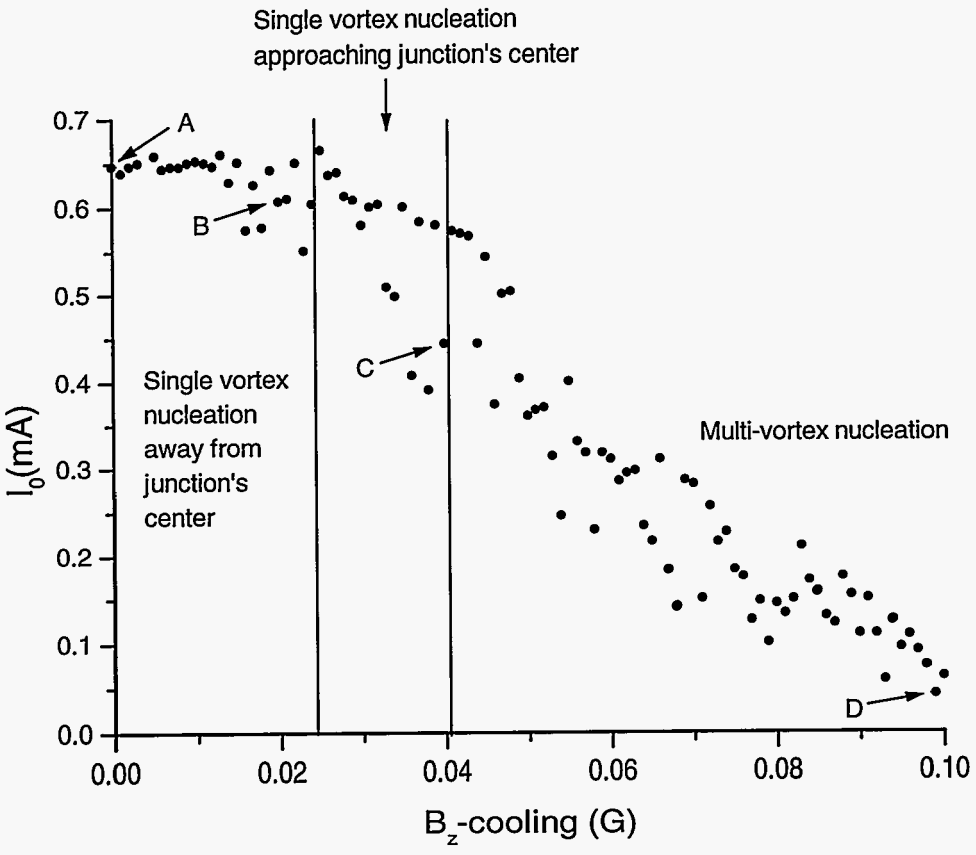

Figure 4.10 Critical current versus the field B_z while cooling

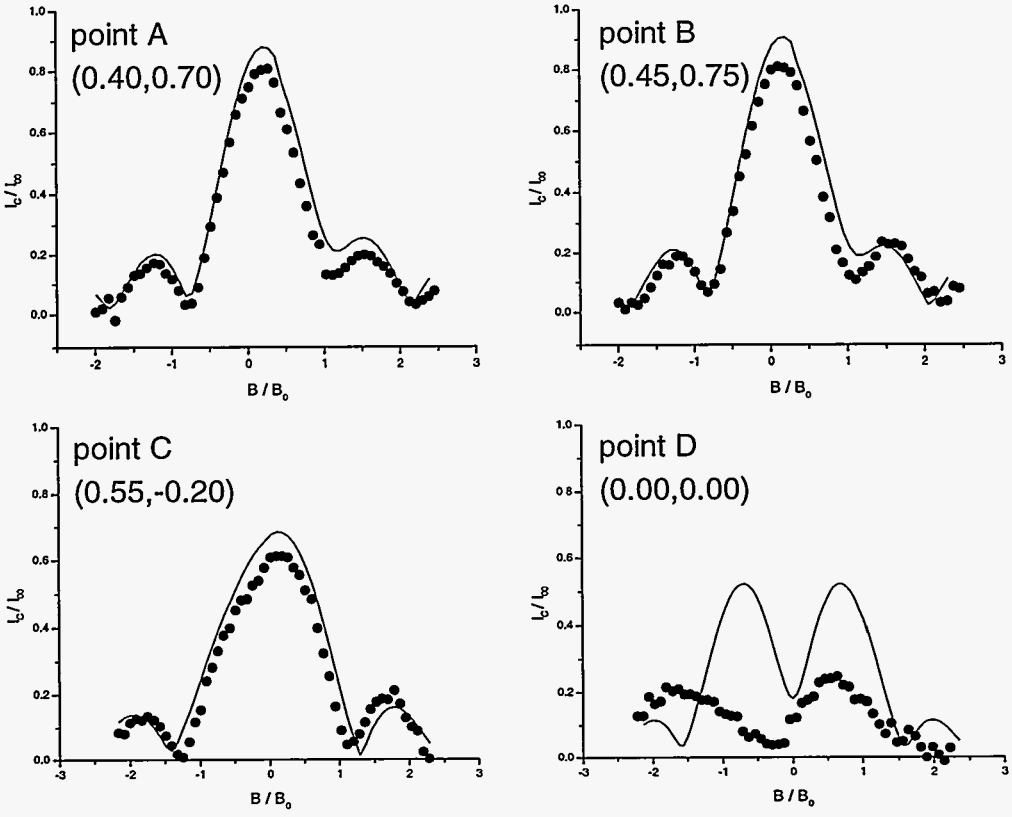

Figure 4.11 The diffraction patterns at points A, B, C, and D of Figure 4.10

potential. The vortex thus becomes unstable. The process of applying heat in order to move the vortex from one pinning site to another, is known as "thermal depinning". It is the purpose of this section to investigate the behavior of a single vortex in a Nb-based junction under thermal depinning. S. C. Sanders [29] studied thermal depinning for Pb-based junctions in the past and Junghyun Sok [41] repeated the experiment for Nb. It will be shown here that our results are in agreement with the work of Sok.

In the experiment that follows, a vortex was nucleated by a rather strange sequence of events. First, the junction was field cooled with $B_z = 40$ mG from 10.5 K down to 7.993 K, in 100 steps of 1 second each. Then a transport current of $I_b = 95$ mA was applied through the bottom film. A diffraction pattern was taken, as shown in Figure 4.12. This pattern is characteristic of a multi-vortex situation because it is generally suppressed and does not show any interference minima. In order to clear the junction from all these vortices, the temperature was raised from 7.993 K to 8.681 K and back to 7.993 K, and the diffraction pattern indicated by the letter "a" in Figure 4.13 was taken. The theoretical fit in Figure 4.14 (solid line) shows that indeed there was only a single vortex present at x = 0.40 and y = -0.10.

Once the vortex was nucleated, the following steps were followed:

1. At the reference temperature of 7.993 K, take a $V - I$ curve.
2. Warm up to the desired depinning temperature in 25 steps of 1 second each.
3. Measure the temperature.
4. Ramp down to the referenced temperature with the same rate used in step 2 above.
5. Take a $V - I$ curve and compare it with the $V - I$ of step 1 above by using the method of the sum of squared differences described in the last section.
6. If there is not a significant change go back to step 2 and repeat
7. If there is a change of 0.15 or more in the sum of squared differences, then take a diffraction pattern

Figure 4.13 shows the results of this experiment. There were seven depinning events, labeled "b" through "h" in the figure, for which the sum of square differences was above the criterion of 0.15. The corresponding diffraction patterns are shown in Fig. 4.14 together with the theoretical fits. It could be argued that the fits of the points "a", "c", "e", "g" and "h" are generally good, representing a single

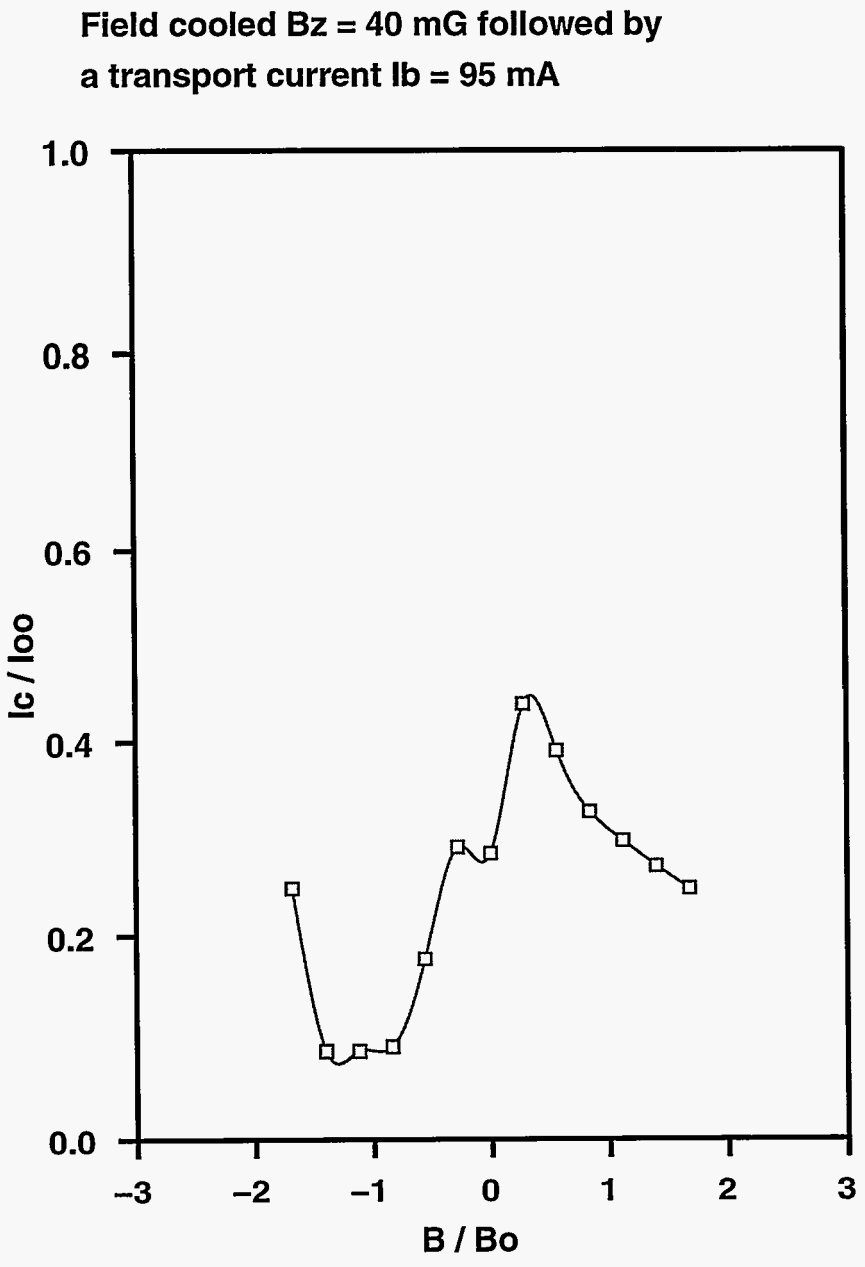

Figure 4.12 Multi-vortex diffraction pattern taken after field cooling at B_z = 40 mG followed by application of a transport current of I_b = 95 mA through the bottom film

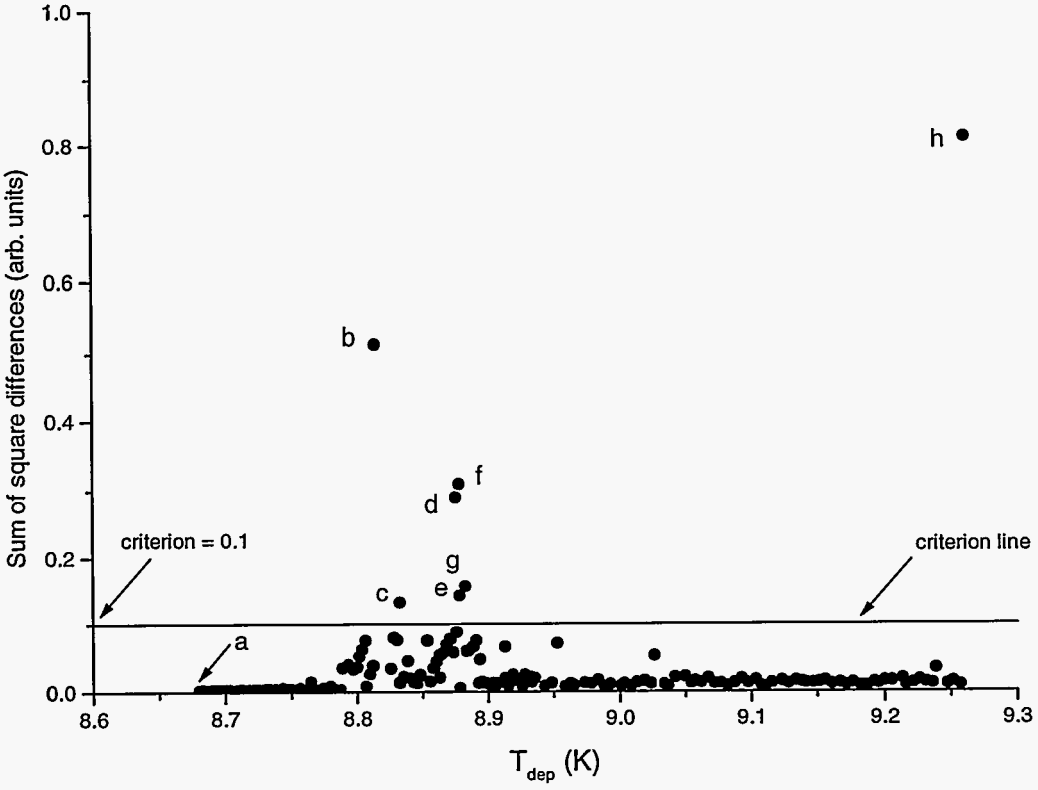

Figure 4.13 Thermal depinning in the absence of an applied field

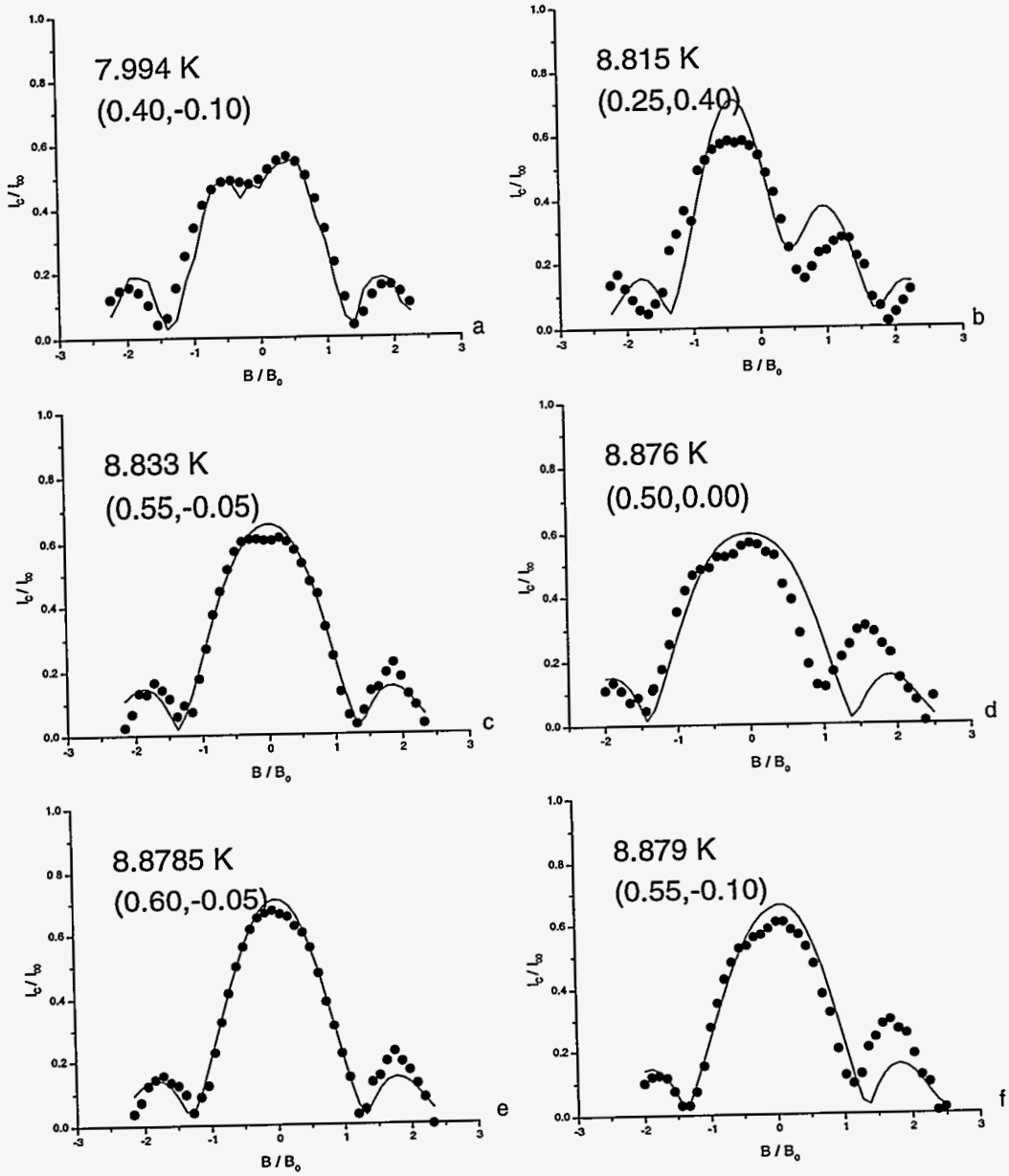

Figure 4.14 Diffraction patterns of points "a" through "h" in Fig. 4.13

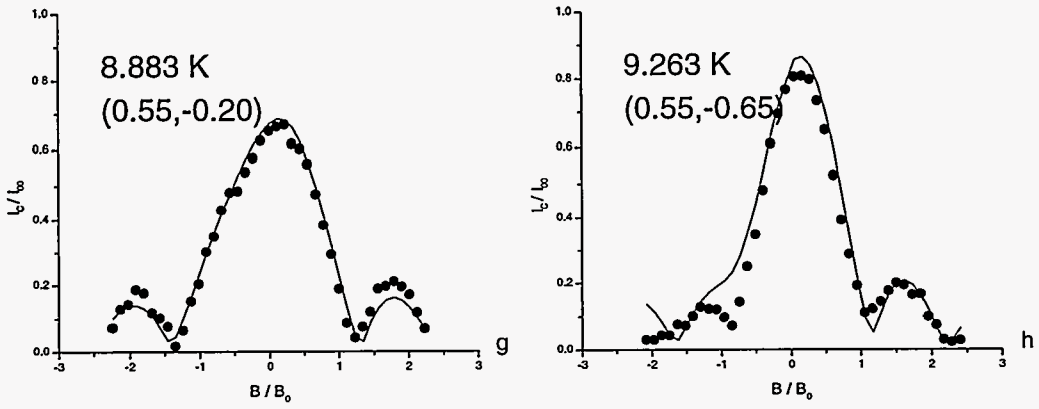

Figure 4.14 (Continued)

vortex at the positions shown on the graphs. The fits at "d" and "f" are not quite so good, indicating probably the coexistence of a vortex at the position that corresponds to the fit, and of another vortex very close to the edge of the junction. This second vortex acts as a small perturbation because it is almost canceled by its closest mirror image vortex. Finally the fit "b" in Figure 4.14 is rather poor, implying the existence of two or more vortices deep inside the junction. Figure 4.15 shows the vortex positions of these fits in the junction. Excluding point "b", which basically has no meaning in this figure, the other points seem to approximately follow a smooth path indicated by a dash line, which could probably be a grain boundary. The above results show that the vortex was initially at the pinning site "a" and as the temperature rose to 8.815 K, a second vortex entered the junction. At 8.833 K, this second vortex left the junction again, while the first vortex moved to the pinning site "c". As the temperature kept rising, the vortex hopped around locally to a few sites before it found its way towards the edge of the junction, at site "h". The depinning temperature of this last step was 9.263 K which is higher than $T_c^{bot} = 8.876$ K and lower than $T_c^{top} = 9.314$ K, indicating that the vortex was trapped at the top film. Unfortunately, further increase of the temperature did not force the vortex to leave the junction. This is in contrast to results of thermal depinning experiments performed on Pb junctions where there was observed a vortex-free temperature window [29, 41].

The depinning temperatures are plotted on a vertical temperature scale in Figure 4.16, in an "energy spectrum" style plot. Also shown for comparison in this diagram, are the transition temperatures of the two films and the junction. It is apparent that nothing much happened to the junction until the temperature was close enough to both T_c^{bot} and T_c^{jun}, at which point, the vortex become very mobile, hopping around from site to site, even for very small temperature increases. It is of interest that there was a temperature window between the last two pinning sites at 8.883 K and 9.263 K, that the vortex did not move, even though the temperatures were quite elevated. That probably implies a strong pinning site at point "g" in Figure 4.15. All the above results are summarized in Table 4.1 which also includes a BSC calculation of the normalized superconducting order parameter Δ/Δ_0 and the superfluid density ρ_s at the depinning temperatures. The calculations were done by using the approximate linear form $(\Delta/\Delta_0)^2 = 2.967(1 - T/T_c^{jun})$, which is valid close to the transition temperature. The values of Δ/Δ_0 = 0.178 and ρ_s = 3.16% where the vortex first moves, were close to the corresponding values of 0.24 and 6.0% found by Sok [41] for a Nb-Al-Al_xO_y-Nb junction. The discrepancy is probably due to the extra Ag layer in our junction.

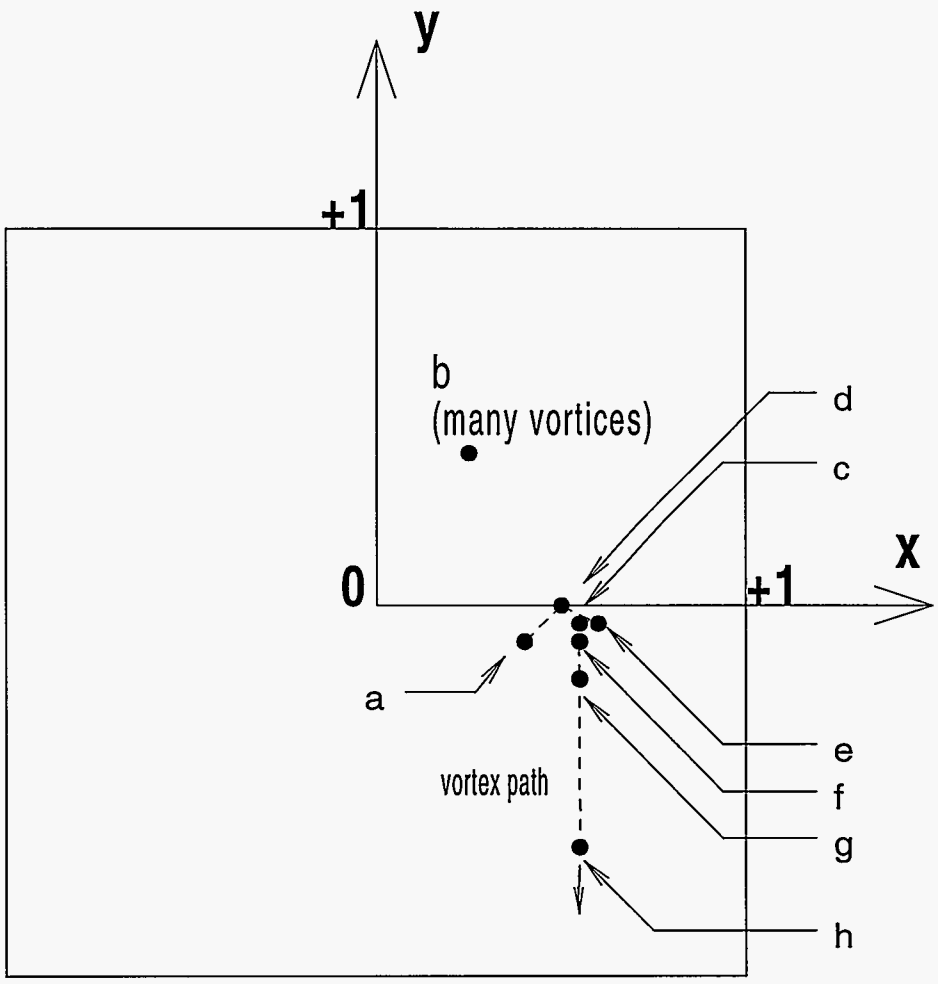

Figure 4.15 Motion of the vortex in the junction during the free-field thermal depinning experiment

Table 4.1 The eight pinning sites of Figure 4.15 and their corresponding depinning temperatures

Pinning site number	Vortex position	Depinning temperature (K)	Δ/Δ_0	ρ_s
a	(0.40, -0.10)	7.994	0.552	30.50%
b	(0.25, 0.40)	8.815	0.178	3.16%
c	(0.55, -0.05)	8.833	0.160	2.56%
d	(0.50, 0.00)	8.876	0.106	1.13%
e	(0.60, -0.05)	8.878	0.103	1.05%
f	(0.55, -0.10)	8.879	0.102	1.03%
g	(0.55, -0.20)	8.883	0.095	0.90%
h	(0.55, -0.65)	9.263	-	-

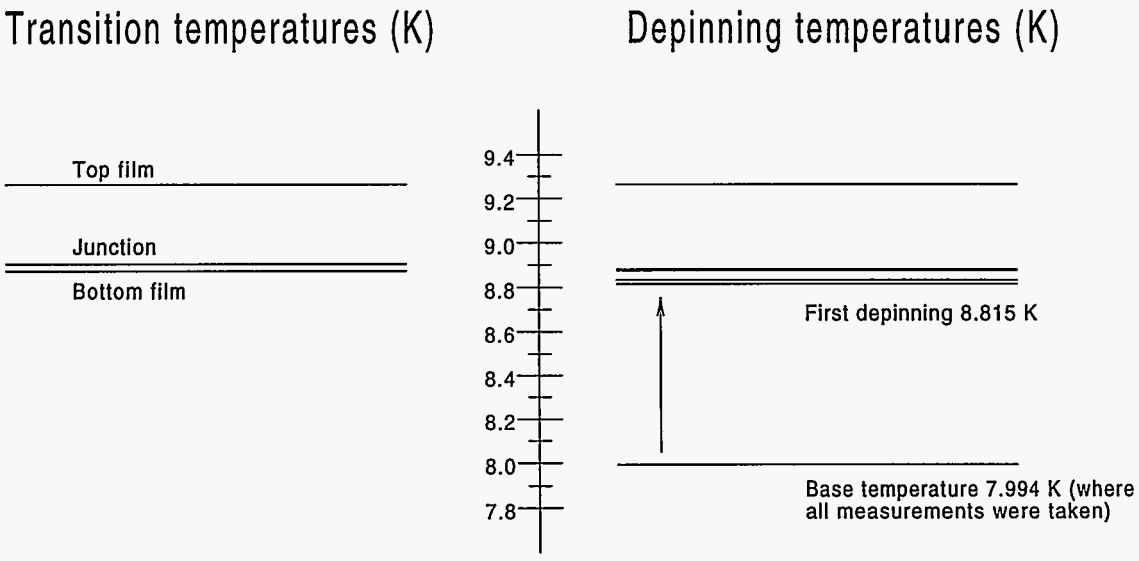

Figure 4.16 Energy-spectrum-like diagram of the depinning temperatures of the field-free thermal depinning experiment

Thermal depinning in the presence of an applied field $B_z = 10$ mG

In this section, the thermal depinning experiment of the last section is repeated in the presence of an applied field $B_z = 10$ mG perpendicular to the junction. In the experiment that follows, a vortex was nucleated by field cooling in $B_z = 50$ mG from 10.5 K down to 7.994 K in 100 steps of 1 second each. The resulting diffraction taken at 7.994 K is shown in Figure 4.17 and the theoretical fit places the vortex at x = 0.50 and y = -0.30.

The steps taken during this experiment are similar to the ones of the last section and they are summarized below:

1. At the reference temperature of 7.994 K, take a $V - I$ curve.
2. Warm up to the desired depinning temperature in 25 steps of 1 second each, under the presence of a field $B_z = 10$ mG.
3. Measure the temperature.
4. Ramp down to the referenced temperature with the same rate and the same B_z field used in step 2 above.
5. Turn the B_z field off.
6. Take a $V - I$ curve and compare it with the $V - I$ of step 1 above by using the method of the sum of the square differences.
7. If there is not a significant change go back to step 2 and repeat
8. If there is a change of 0.15 or more in the sum of square differences, then take a diffraction pattern

There were totally 28 diffraction patterns taken during this process and they are shown in Figures 4.18. The corresponding vortex path is shown in Figure 4.19. As in the last section, there are cases where a theoretical single vortex diffraction pattern cannot fit the data. These points are indicated by "m.v." (multi-vortex) in Figure 4.19. It can be said that initially the vortex was hopping around locally from site to site but as the temperature kept rising, the hopping become larger and more random. There was not any apparent path that the vortex would follow. Figure 4.20 shows all the depinning temperatures in a vertical temperature scale, as in the last section. It appears that the application of the B_z field of 10 mG during the thermal depinning had two major effects:

- Lowering of the first depinning temperature.

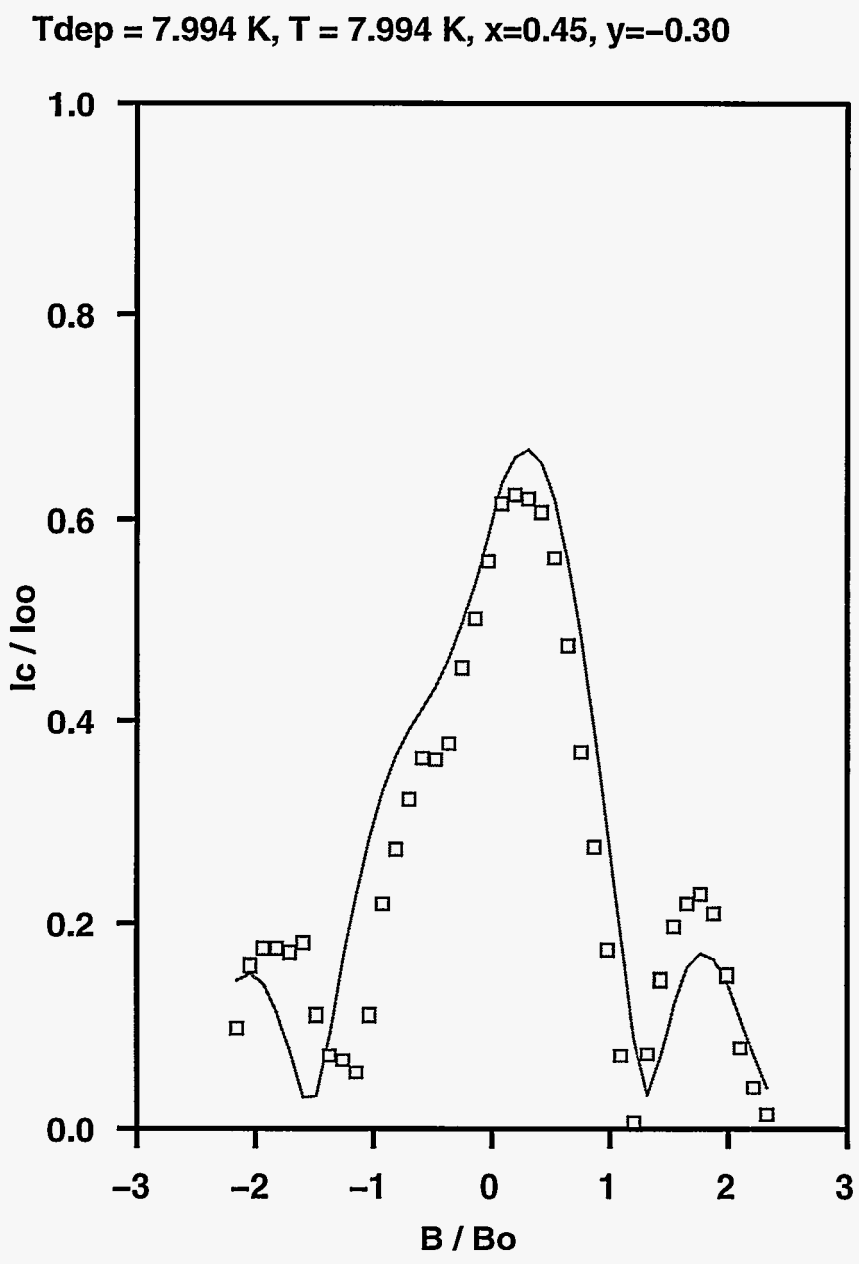

Figure 4.17 Diffraction pattern taken after a vortex was field cooled nucleated with $B_z = 50$ mG

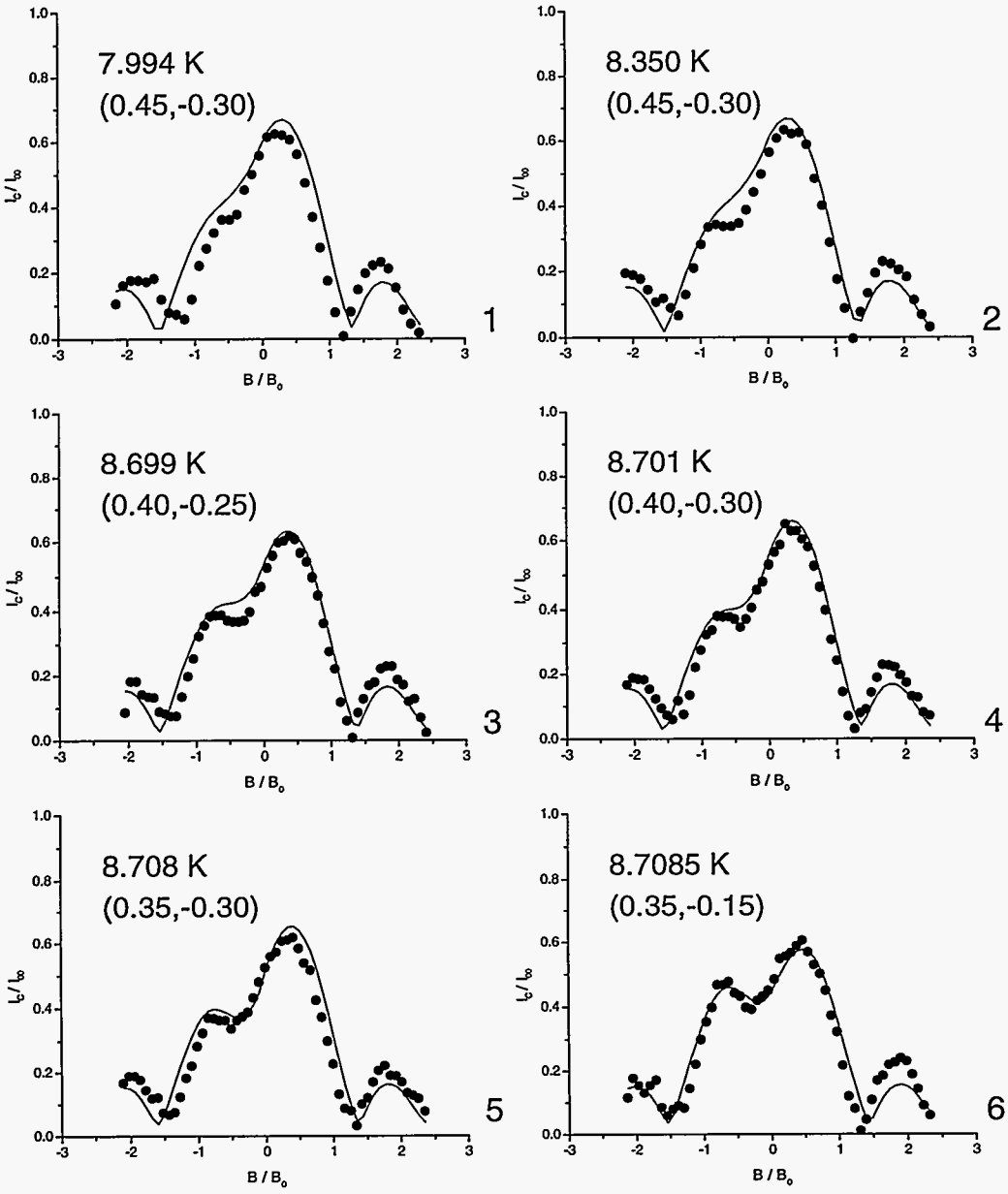

Figure 4.18 The diffraction patterns taken during the $B_z = 10$ mG thermal depinning experiment

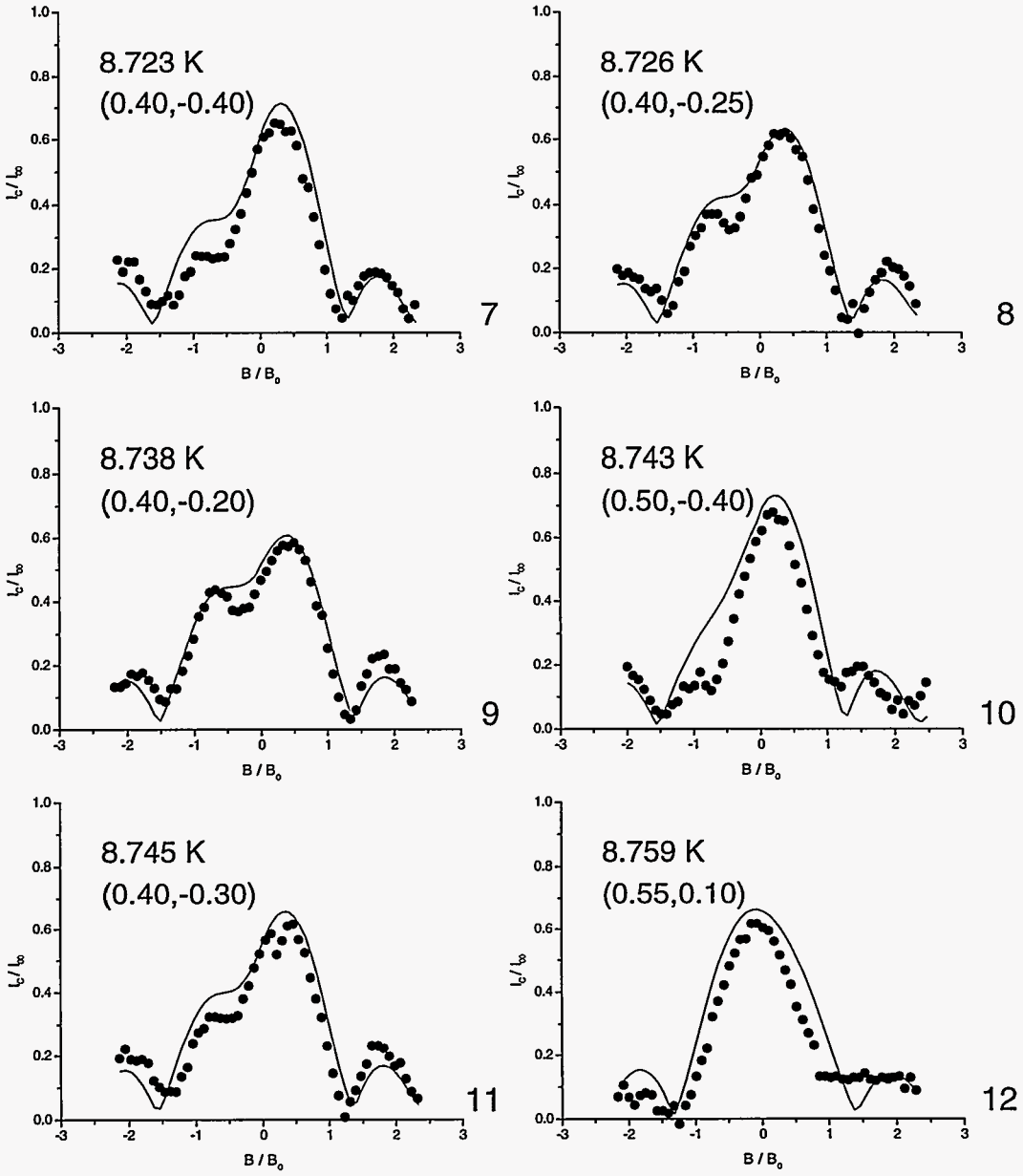

Figure 4.18 (Continued)

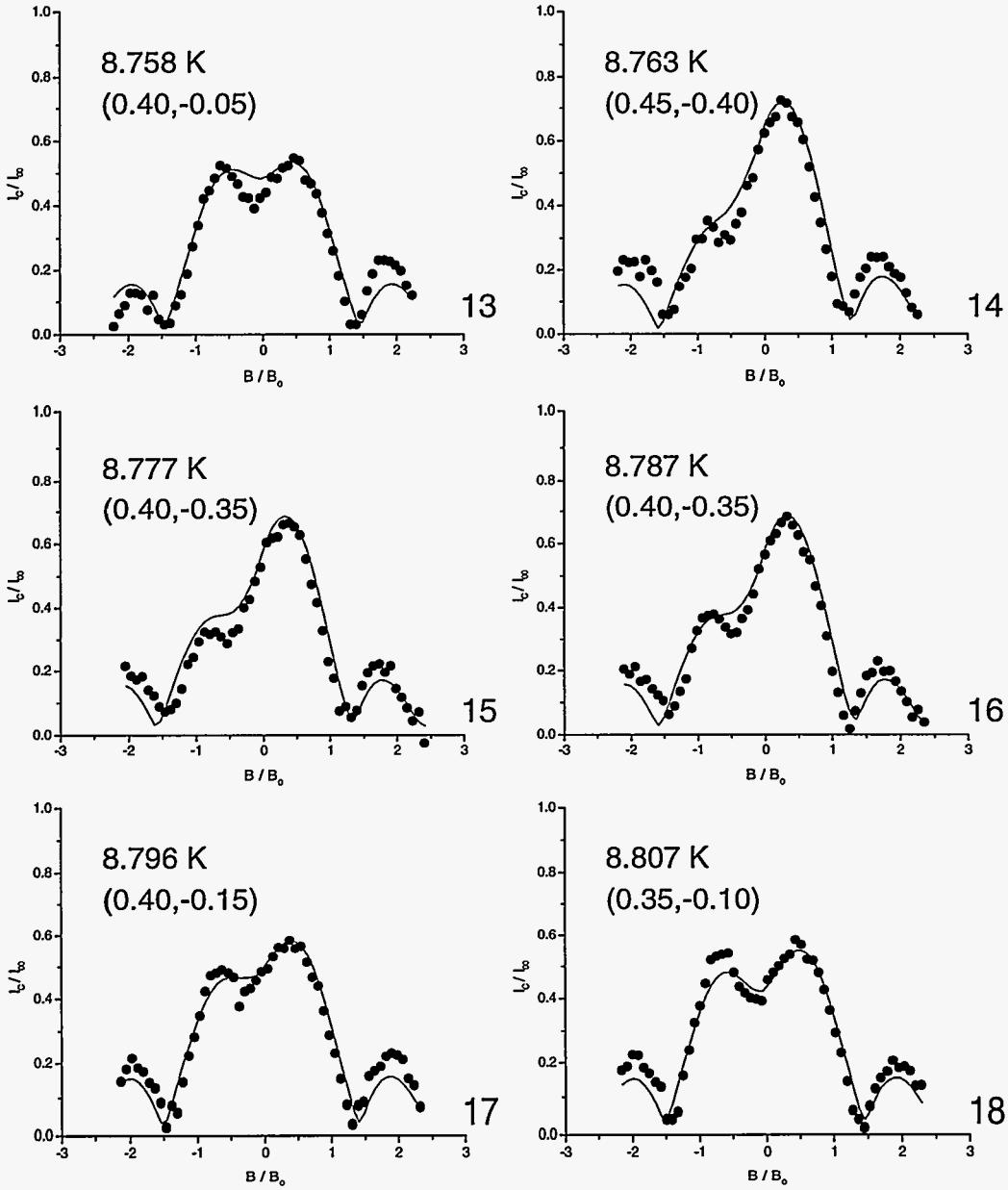

Figure 4.18 (Continued)

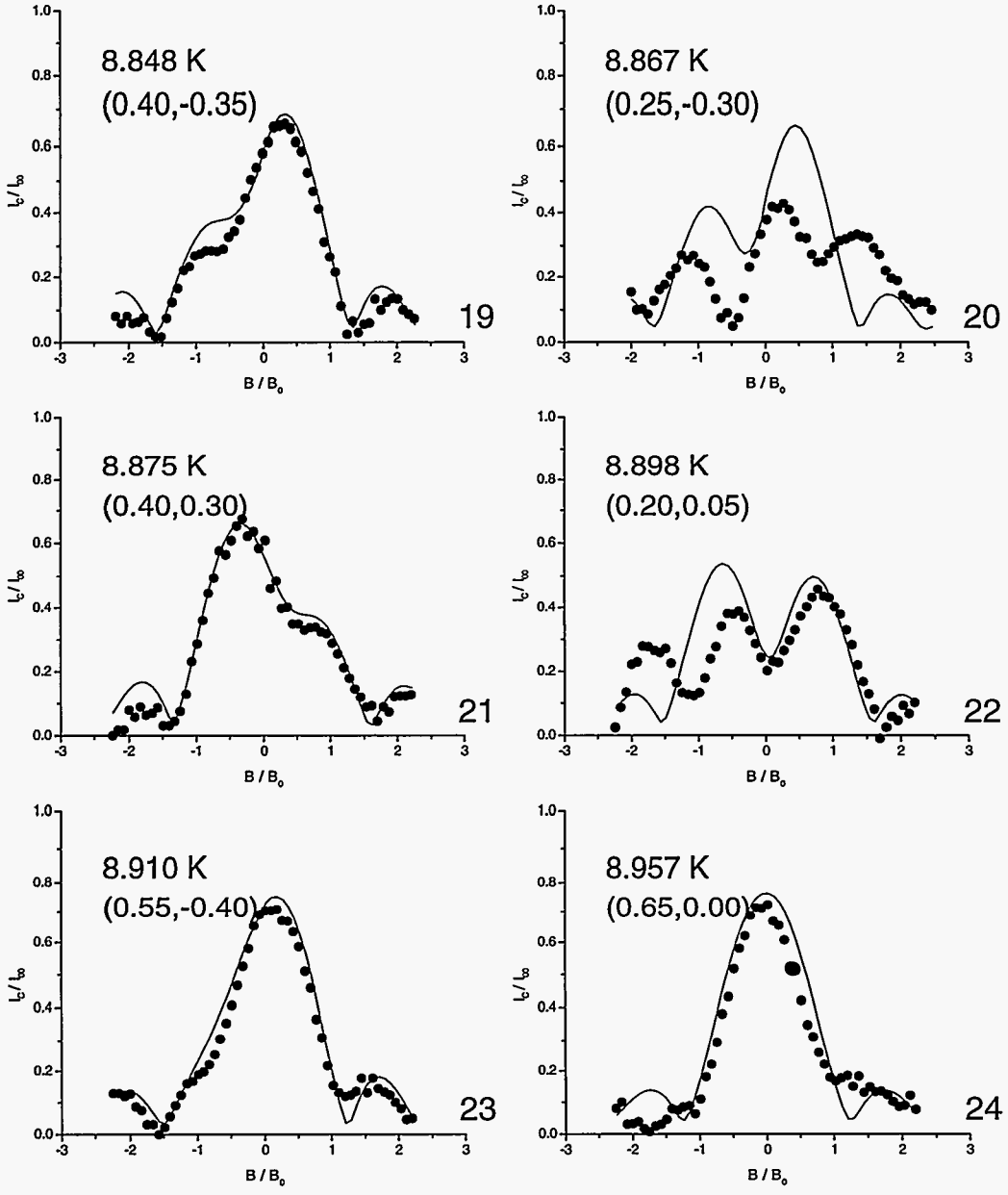

Figure 4.18 (Continued)

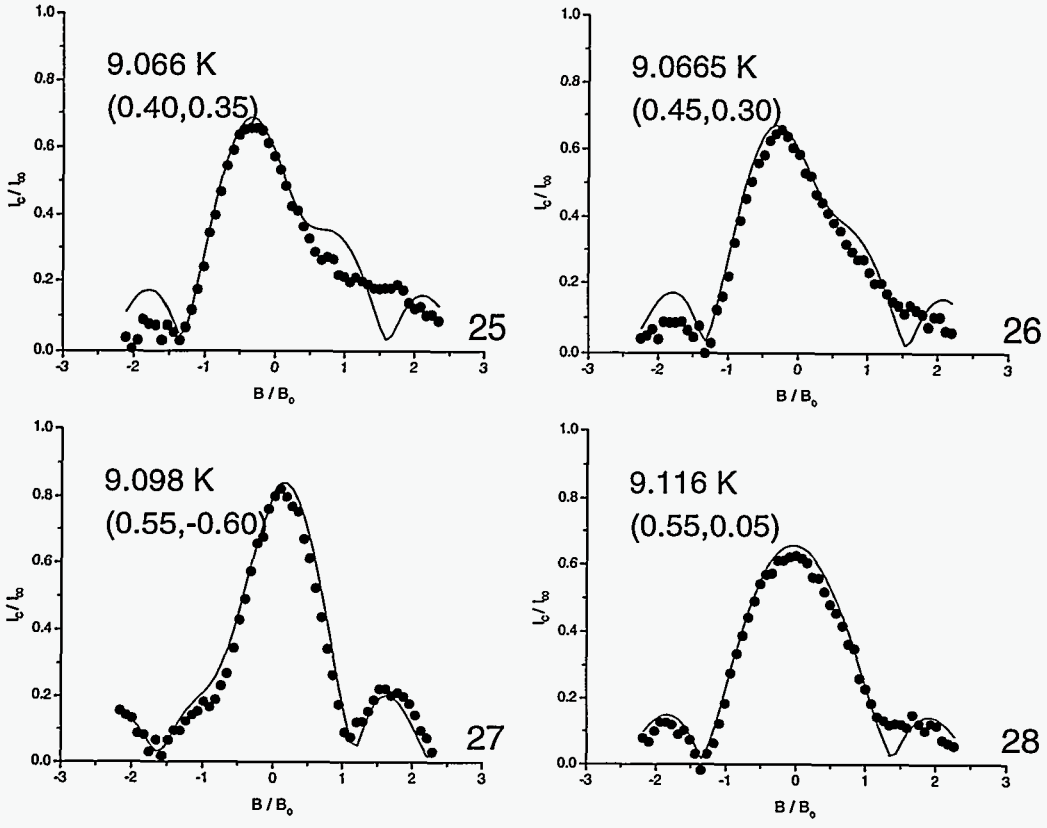

Figure 4.18 (Continued)

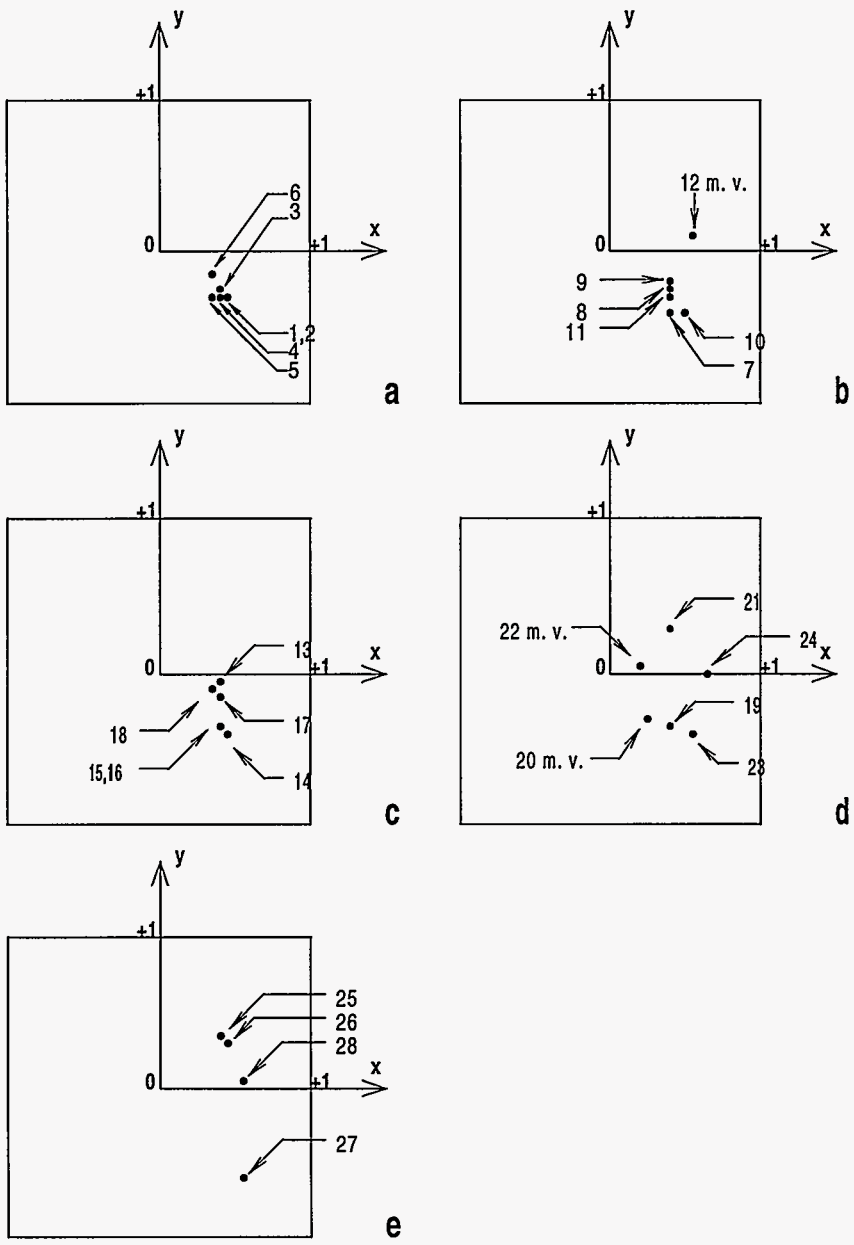

Figure 4.19 Motion of the vortex in the junction during the $B_z = 10$ mG thermal depinning experiment

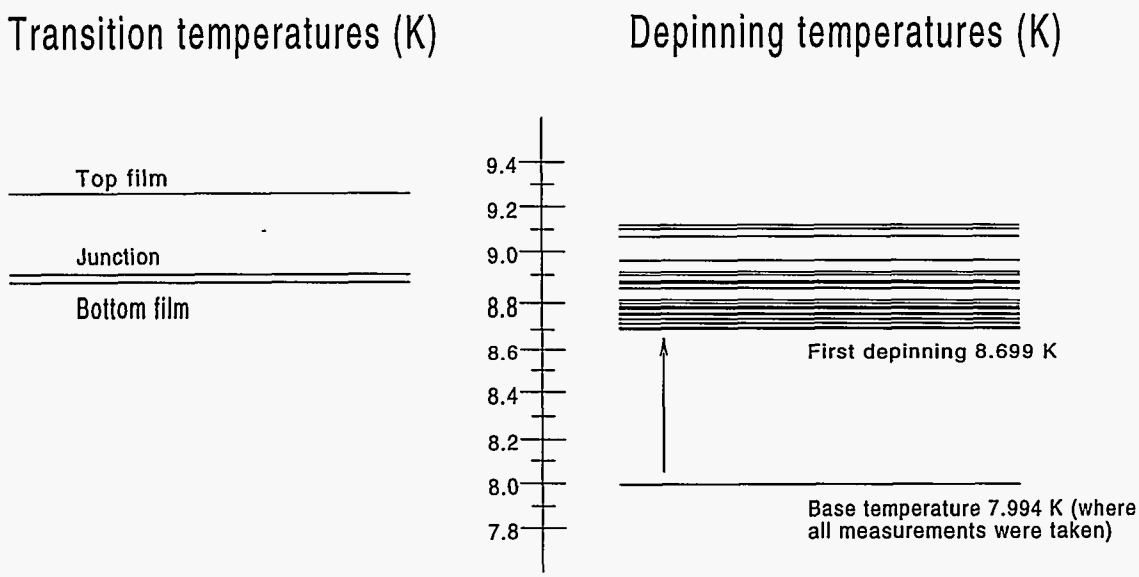

Figure 4.20 Energy-spectrum-like diagram of the depinning temperatures of the $B_z = 10$ mG thermal depinning experiment

- Appearance of an almost continuum of depinning temperatures above the first depinning temperature.

The above results suggest that once the vortex left its initial pinning site of (0.45, -0.30) at $T = 8.699$ K, it become very unstable due to the external magnetic field, wandering from site to site in the junction. There is still a fairly large temperature gap between 8.957 and 9.066 K in Figure 4.20 but both above and below it, the vortex seemed to be very mobile. Since this gap is above T_c^{bot}, it means that vortex was trapped at the top film, as in the last section. There are also smaller gaps present, indicating the existence of strong pinning sites in the junction. The positions of these strong pinning sites are shown in Figure 4.21 together with the temperature gaps needed to depin a particular site. Also shown for comparison is the path of the thermal depinning experiment of the last section. Two of the pinning sites are on this path, reinforcing the idea that the path could lay on a grain boundary. Most of the other sites also lay on a path which could be another grain boundary. All the above results are summarized in Table 4.2 which as in the last section, includes a BSC calculation of the normalized superconducting order parameter Δ/Δ_0 and the superfluid density ρ_s at the depinning temperatures.

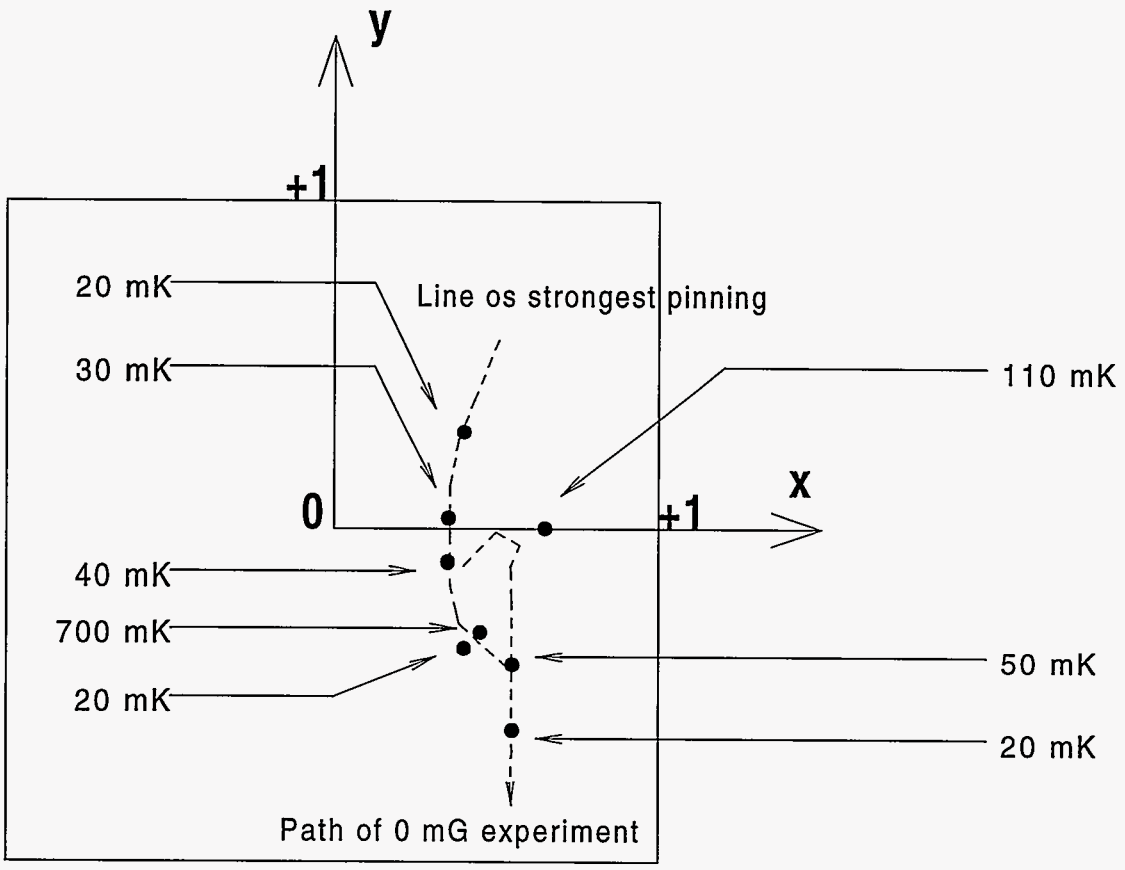

Figure 4.21 The eight strongest pinning sites of the $B_z = 10$ mG thermal depinning experiment and the temperature differences needed to depin the vortex

Table 4.2 The twenty eight pinning sites of Figure 4.19 and their corresponding depinning temperatures

Pinning site number	Vortex position	Depinning temperature (K)	Δ/Δ_0	ρ_s
1	(0.45, -0.30)	7.994	0.552	30.50%
2	(0.45, -0.30)	8.350	0.432	18.6%
3	(0.40, -0.25)	8.699	0.265	7.03%
4	(0.40, -0.30)	8.701	0.264	6.96%
5	(0.35, -0.30)	8.708	0.259	6.73%
6	(0.35, -0.15)	8.709	0.259	6.71%
7	(0.40, -0.40)	8.723	0.250	6.23%
8	(0.40, -0.25)	8.726	0.248	6.13%
9	(0.40, -0.20)	8.738	0.239	5.73%
10	(0.50, -0.40)	8.743	0.236	5.56%
11	(0.40, -0.30)	8.745	0.234	5.49%
12	(0.55, 0.10)	8.759	0.224	5.03%
13	(0.40, -0.05)	8.758	0.225	5.06%
14	(0.45, -0.40)	8.763	0.221	4.90%
15	(0.40, -0.35)	8.777	0.210	4.43%
16	(0.40, -0.35)	8.787	0.202	4.10%
17	(0.40, -0.15)	8.796	0.195	3.80%
18	(0.35, -0.10)	8.807	0.185	3.43%
19	(0.40, -0.35)	8.848	0.144	2.06%
20	(0.25, -0.30)	8.867	0.120	1.43%
21	(0.40, 0.30)	8.875	0.108	1.17%
22	(0.20, 0.05)	8.898	0.063	0.40%
23	(0.55, -0.40)	8.910	0.000	0.00%
24	(0.65, 0.00)	8.957	-	-
25	(0.40, 0.35)	9.066	-	-
26	(0.45, 0.30)	9.067	-	-
27	(0.55, -0.60)	9.098	-	-
28	(0.55, 0.05)	9.116	-	-

Thermal depinning in the presence of an applied field $B_z = -10$ mG

Sixteen different pinning sites were observed during the thermal depinning experiment under a field of $B_z = -10$ mG. The corresponding diffraction patterns are shown in Figure 4.22 and the vortex path is shown in Figure 4.23. Unlike the last two sections, most of the theoretical single vortex fits are generally good, and it can be argued that there was always a single vortex present in the junction. As it was expected, the vortex moved in gradually larger steps as the temperature was rising. Also the vortex seemed to be more stable, since the temperature gaps in Figure 4.24 are well defined, and the continuum of depinning temperatures of the last section has disappeared. However, there are still a lot more depinning temperatures than in Figure 4.16 which shows that generally the application of a B_z field enhances depinning. The temperature $T = 8.648$ K where the vortex first moved is very close to the corresponding 8.699 K of $B_z = 10$ mG. Also there is a large temperature gap of about 110 mK for B_z = -10 mG which is of the same magnitude as the corresponding gap of $B_z = 10$ mG. They also happen at about the same temperature, 8.957 for $B_z = 10$ mG and 8.989 for B_z = - 10 mG. Following the same argument as in the last section, the vortex was apparently trapped at the top film since the gap was above T_c^{bot}. Figure 4.25 shows the positions of the strongest pinning sites of this experiment, together with the temperature gaps. Some of these sites appear to lay on a new path which, as above, it could possibly be a grain boundary. All the above results are summarized in Table 4.3.

Thermal depinning temperatures versus applied field B_z

The thermal depinning experiments were repeated for two more values of B_z, 5 and -5 mG respectively. Since the last two sections covered the details of the thermal depinning experiment under a field B_z, the results will be presented here only briefly. Table 4.4 shows T_0^{dep}, the depinning temperature where the vortex first moves, for five different values of B_z. A plot of these values is also shown in Figure 4.26

Two vortex problem

In general, it is more difficult to deal with the two-vortex problem than the one-vortex problem. One reason for this is that the fitting programs take much longer time and they require larger disk space because the number of possibilities is larger. For example, if one divides the junction in 20 $\times$ 20 blocks he (she) will have 400 possibilities for the position of a single vortex, which will increase to $400^2 = 160000$ possibilities for a pair of vortices. Also, from the physical point of view the two-

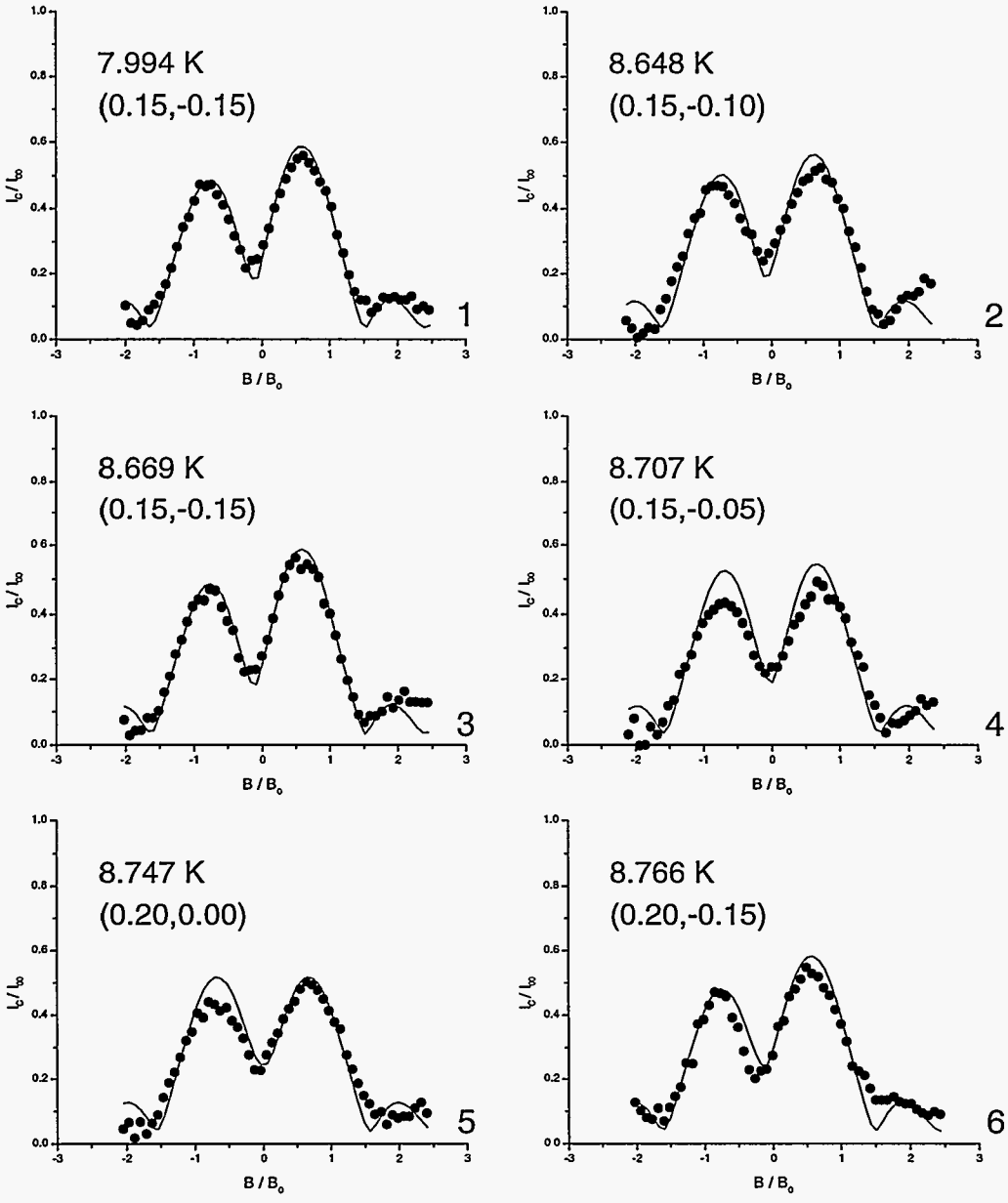

Figure 4.22 The diffraction patterns taken during the B_z = -10 mG thermal depinning experiment

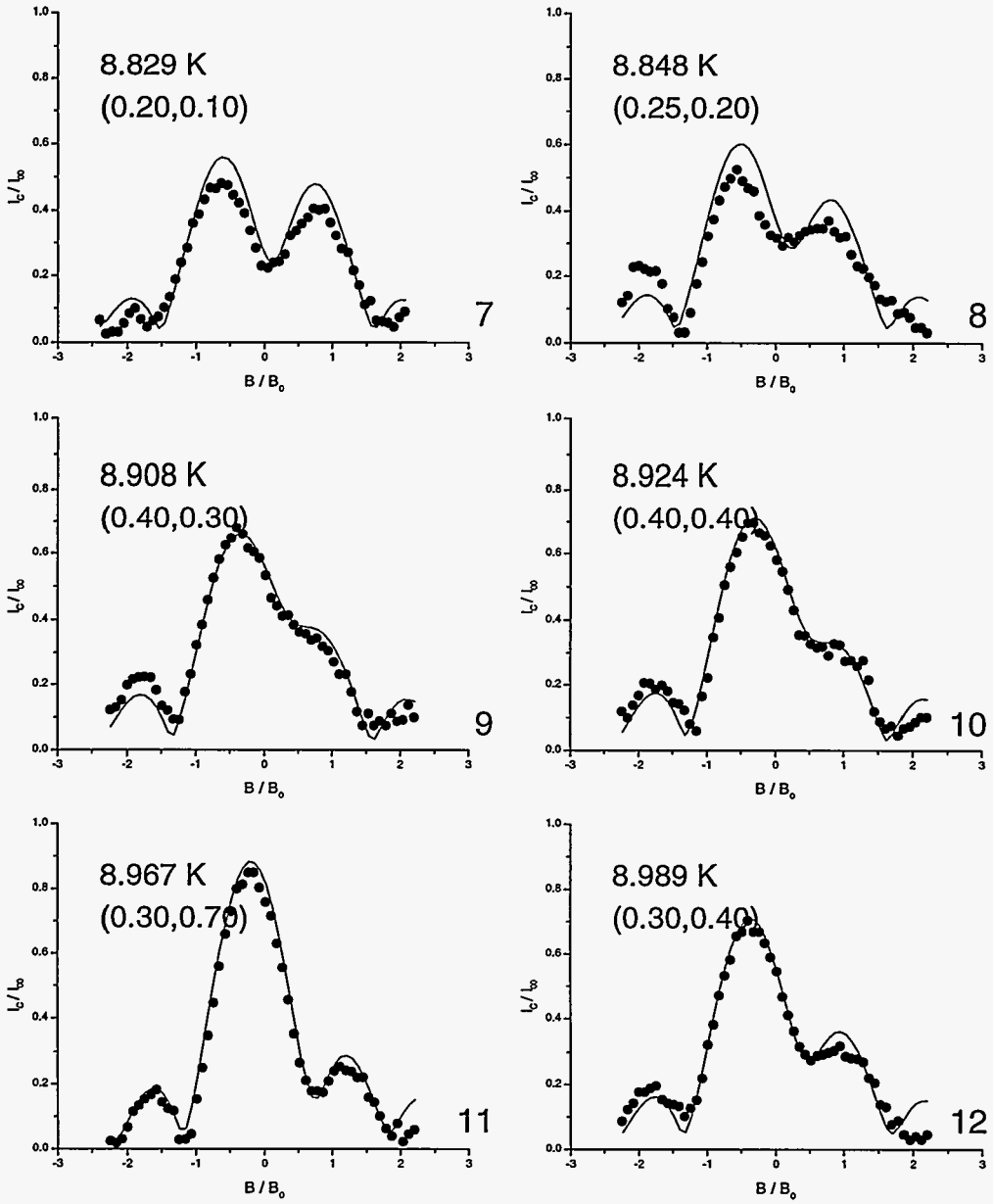

Figure 4.22 (Continued)

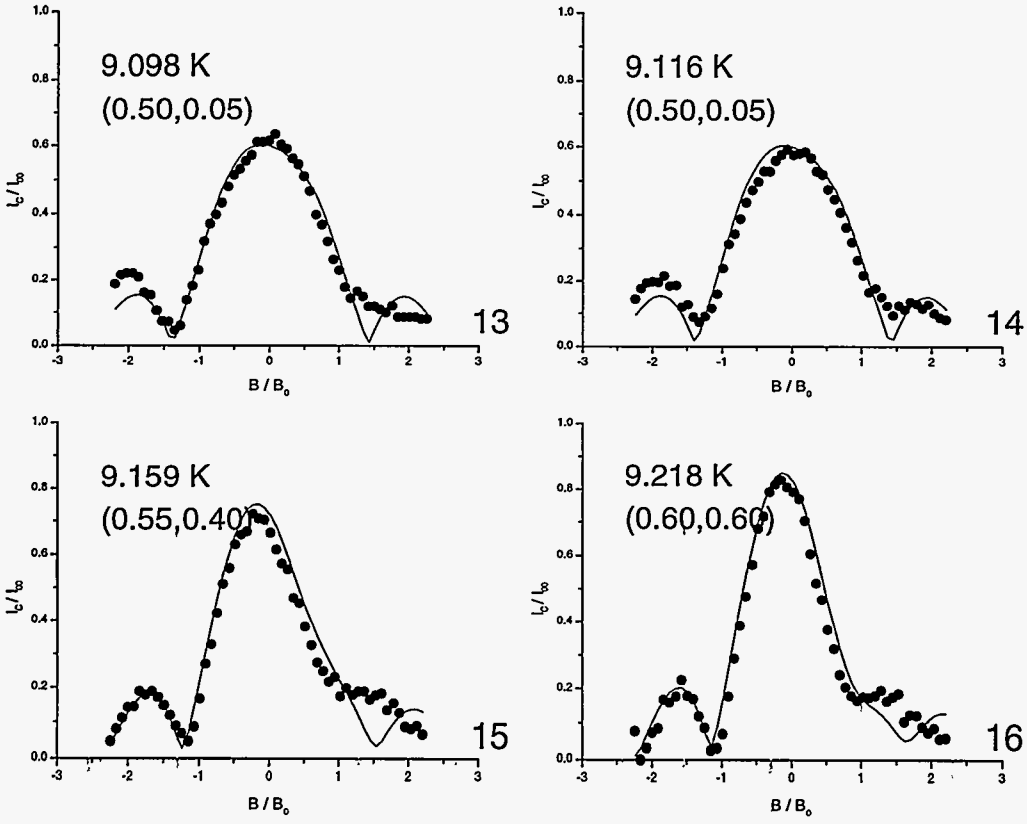

Figure 4.22 (Continued)

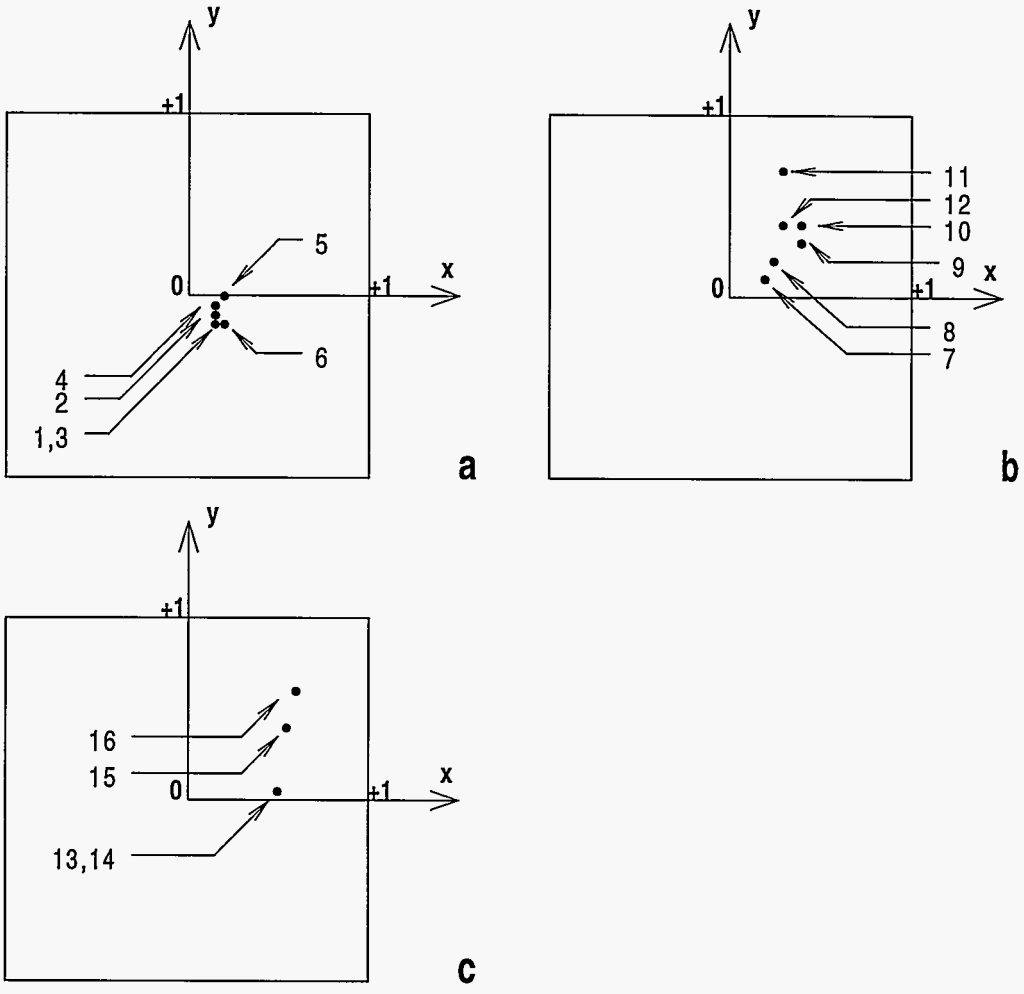

Figure 4.23 Motion of the vortex in the junction during the B_z = -10 mG thermal depinning experiment

Table 4.3 The sixteen pinning sites of Figure 4.23 and their corresponding depinning temperatures

Pinning site number	Vortex position	Depinning temperature (K)	Δ/Δ_0	ρ_s
1	(0.15, -0.15)	7.994	0.552	30.50%
2	(0.15, -0.10)	8.648	0.295	8.72%
3	(0.15, -0.15)	8.669	0.283	8.03%
4	(0.15, -0.05)	8.707	0.260	6.76%
5	(0.20, 0.00)	8.747	0.233	5.43%
6	(0.20, -0.15)	8.766	0.219	4.80%
7	(0.20, 0.10)	8.829	0.164	2.70%
8	(0.25, 0.20)	8.848	0.144	2.06%
9	(0.40, 0.30)	8.908	0.026	0.06%
10	(0.40, 0.40)	8.924	-	-
11	(0.30, 0.70)	8.967	-	-
12	(0.30, 0.40)	8.989	-	-
13	(0.50, 0.05)	9.098	-	-
14	(0.50, 0.05)	9.116	-	-
15	(0.55, 0.40)	9.159	-	-
16	(0.60, 0.60)	9.218	-	-

Table 4.4 The temperatures where the vortex was first depinned T_0^{dep} versus the perpendicular magnetic field B_z

B_z(mG)	T_0^{dep} (K)
-10	8.648
-5	8.544
0	8.815
5	8.715
10	8.699

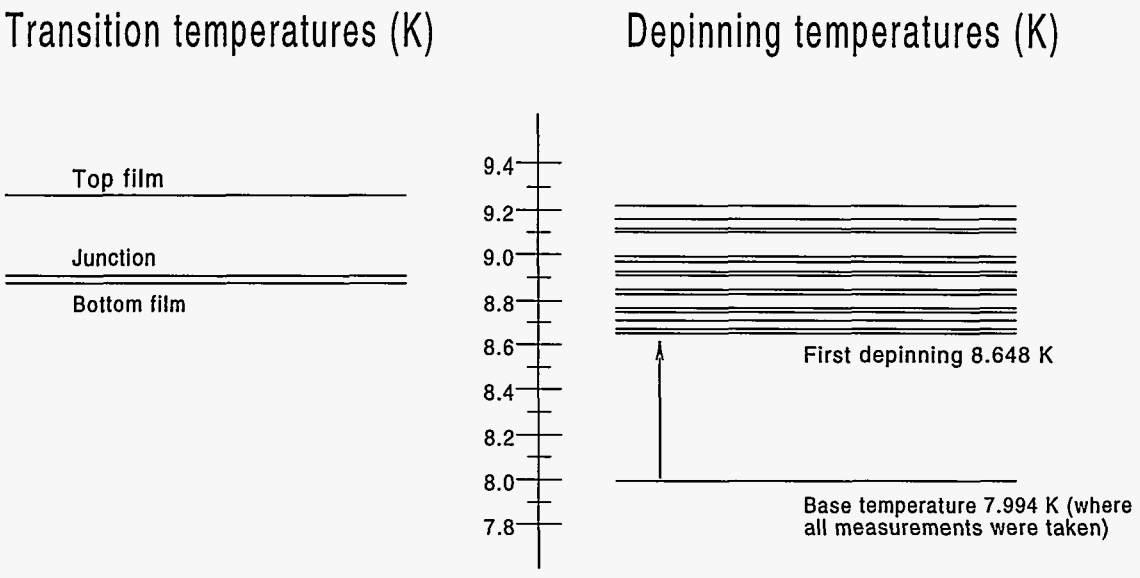

Figure 4.24 Energy-spectrum-like diagram of the depinning temperatures of the B_z = -10 mG thermal depinning experiment

vortex problem is more complicated, as well as more interesting, due to the interaction between the two vortices.

The experiment that follows has nothing to do with the process of the thermal depinning which is the focus of the present work. It is just a supplement to the main body of the present work, and a possible initiation for future work. All the two-vortex measurements were done on the DK5-91 sample. Actually the diffraction patterns measured on this sample were impossible to fit by one-vortex theoretical patterns. The next step was to try a two-vortex fit which turned out to be quite successful. A depinning current experiment was performed on this sample that consisted of the following steps:

1. Try to nucleate a vortex and bring the system at the reference temperature of 6.995 K.
2. Apply the desired current through the bottom film. Name this current I_p
3. Take a diffraction pattern.
4. Calculate s, the sum of the squared differences between the current diffraction pattern and the one taken at the beginning of the experiment.

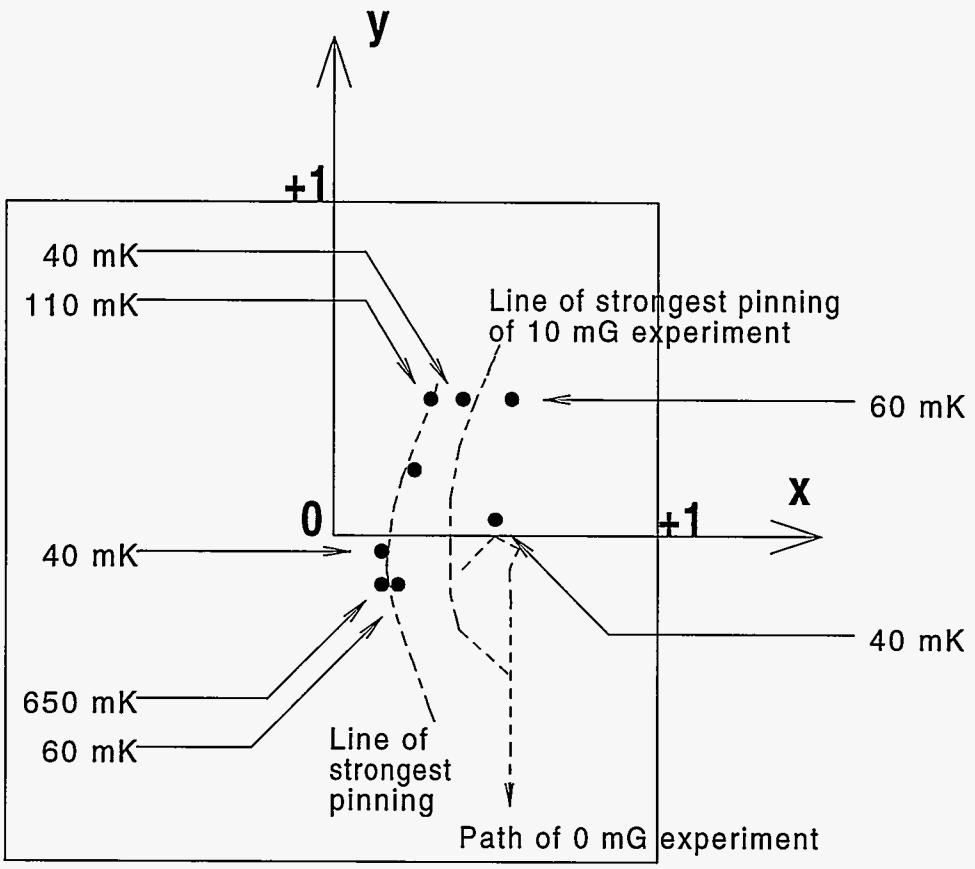

Figure 4.25 The eight strongest pinning sites of the B_z = -10 mG thermal depinning experiment and the temperature differences needed to depin the vortex

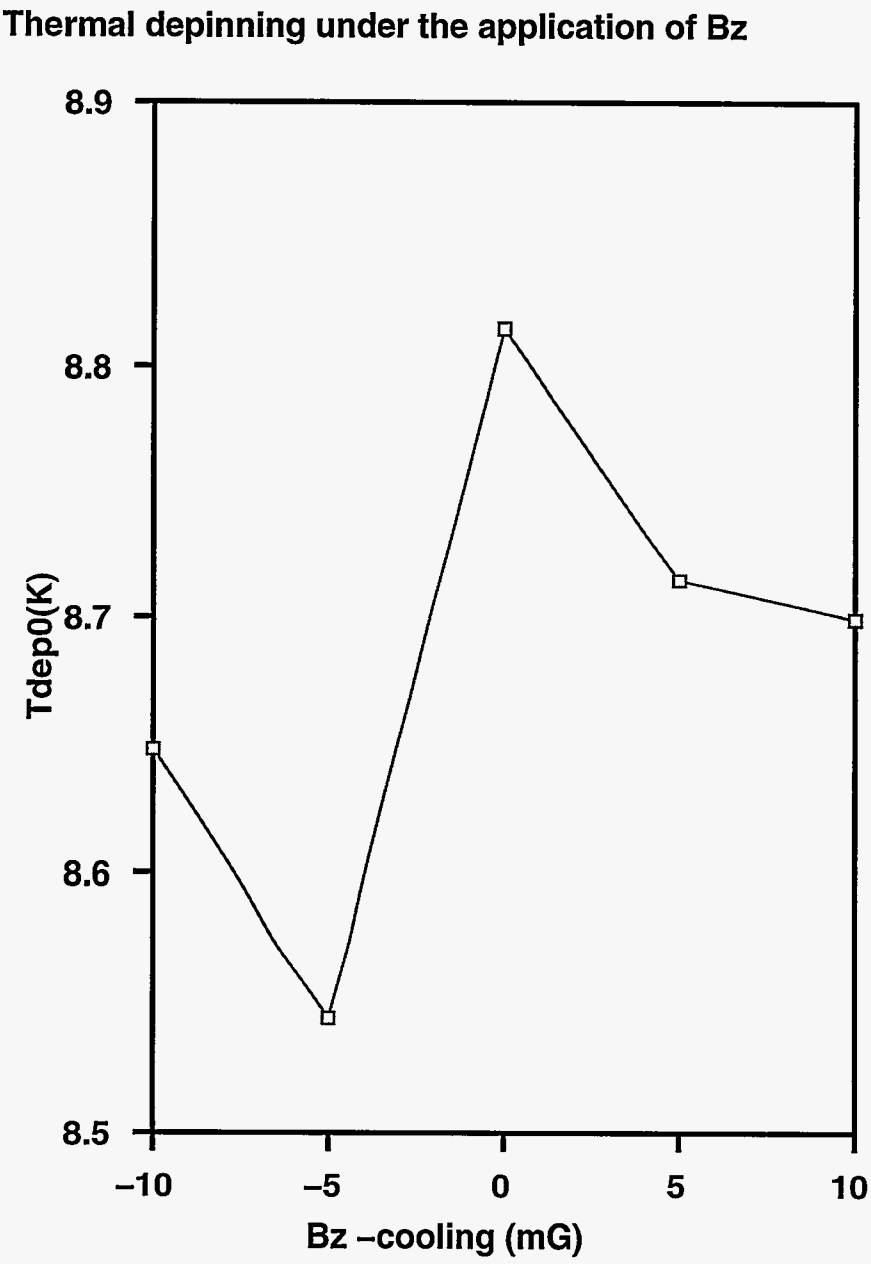

Figure 4.26 Depinning temperature where the vortex first moves versus the applied field

5. Plot the (I_p, s) pair on a graph

6. Repeat steps 2-5 above with slightly higher I_p.

The resulting plot is showing at Figure 4.27 and the corresponding diffraction patterns at Figure 4.28. All the theoretical fits correspond to a two-vortex configuration with the two vortices having the same polarity and are characterized by their elevated minima. Although in general it is rather unlike to have two vortices with the same polarity, this configuration has been observed by other authors in the past [45, 46] It looks like there is a good agreement between these fits and the data, leading to the conclusion that there are two vortices present in the junction. Table 4.5 gives the positions of each vortex pair and the corresponding applied current. These positions are also depicted schematically in Figure 4.29. It can be immediately seen from this figure that the two vortices did not move much from their original position, and they always kept a diagonally opposite position from each other. This result is to be expected because there is always a repulsive interaction between vortices of the same polarity, pretty much like in electrostatics. Therefore, in an effort to minimize this interaction the vortices are trying to lie along the longest direction in the junction which is one of the main diagonals. On the other hand, Meissner shielding currents flowing on the surface of the junction, push the two vortices towards the center. These Meissner currents are present only when $B_z \neq 0$, but as it was mentioned above there are always some stray fields present of the order of 5 mG. It is the equilibrium between these two forces that keeps the two vortices diagonally opposite and around the two clusters shown in Figure 4.29.

Table 4.5 The thirteen pinning sites of Figure 4.27

Site	I_b	x_1	y_1	x_2	y_2
0	0.00	-0.537	-0.262	0.462	0.262
1	0.01	-0.537	-0.262	0.462	0.262
2	0.02	-0.537	-0.262	0.462	0.262
3	0.03	-0.537	-0.262	0.462	0.262
4	0.04	-0.512	-0.262	0.562	0.262
5	0.05	-0.487	-0.262	0.562	0.262
6	0.06	-0.487	-0.262	0.537	0.262
7	0.07	-0.487	-0.262	0.537	0.262
8	0.08	-0.512	-0.262	0.562	0.262
9	0.09	-0.512	-0.312	0.562	0.362
10	0.10	-0.437	-0.262	0.512	0.237
11	0.11	-0.426	-0.262	0.512	0.237
12	0.12	-0.437	-0.262	0.512	0.237

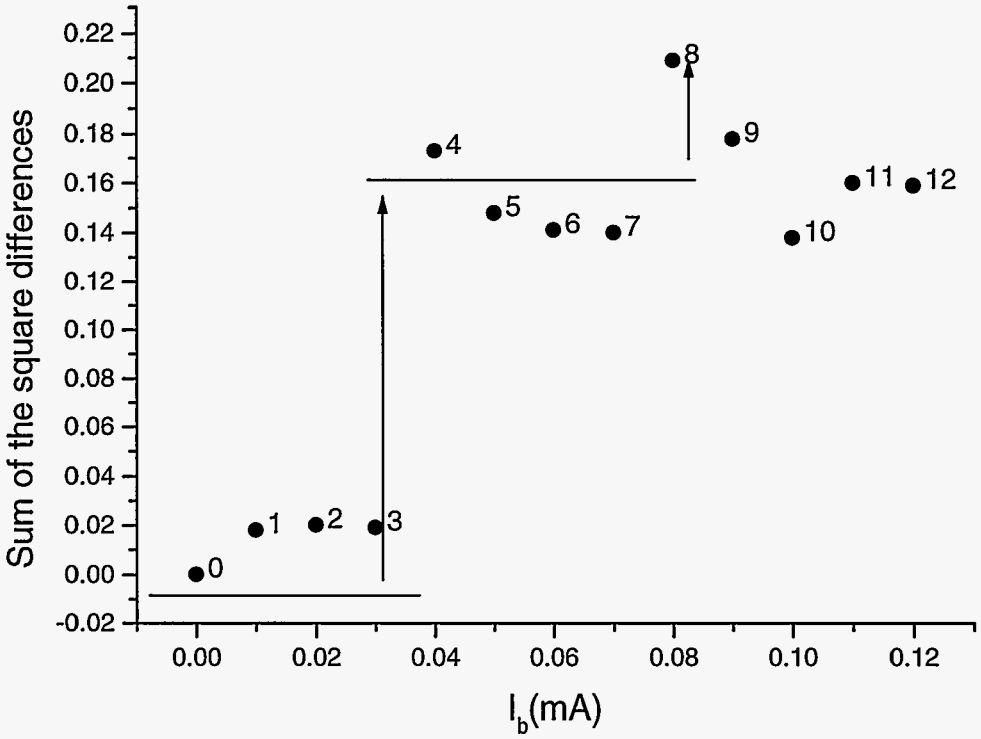

Figure 4.27 Two vortex depinning experiment by the application of a transport current through the bottom film. The arrows indicate depinning jumps

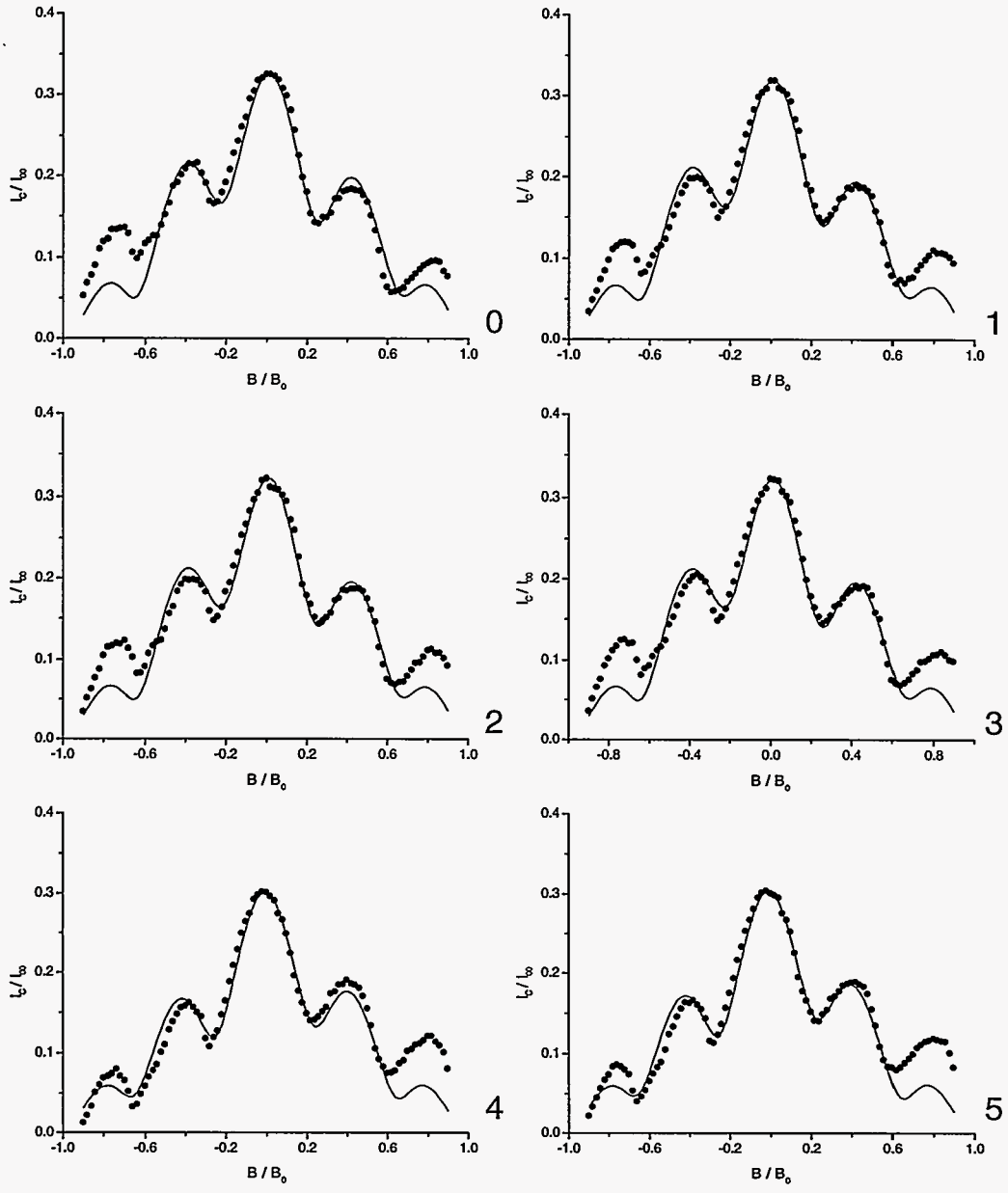

Figure 4.28 Diffraction patterns corresponding to each point of Figure 4.27

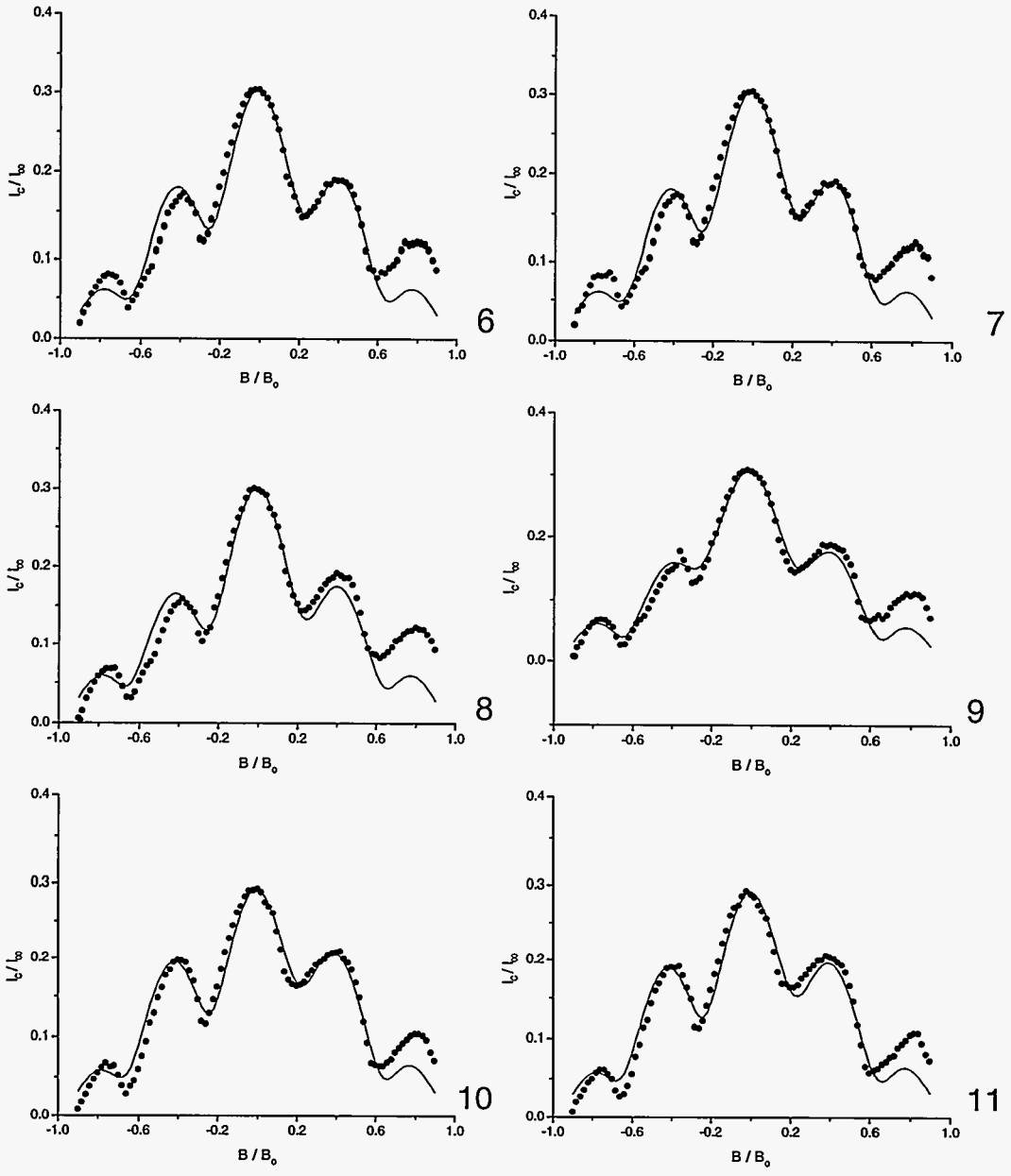

Figure 4.28 (Continued)

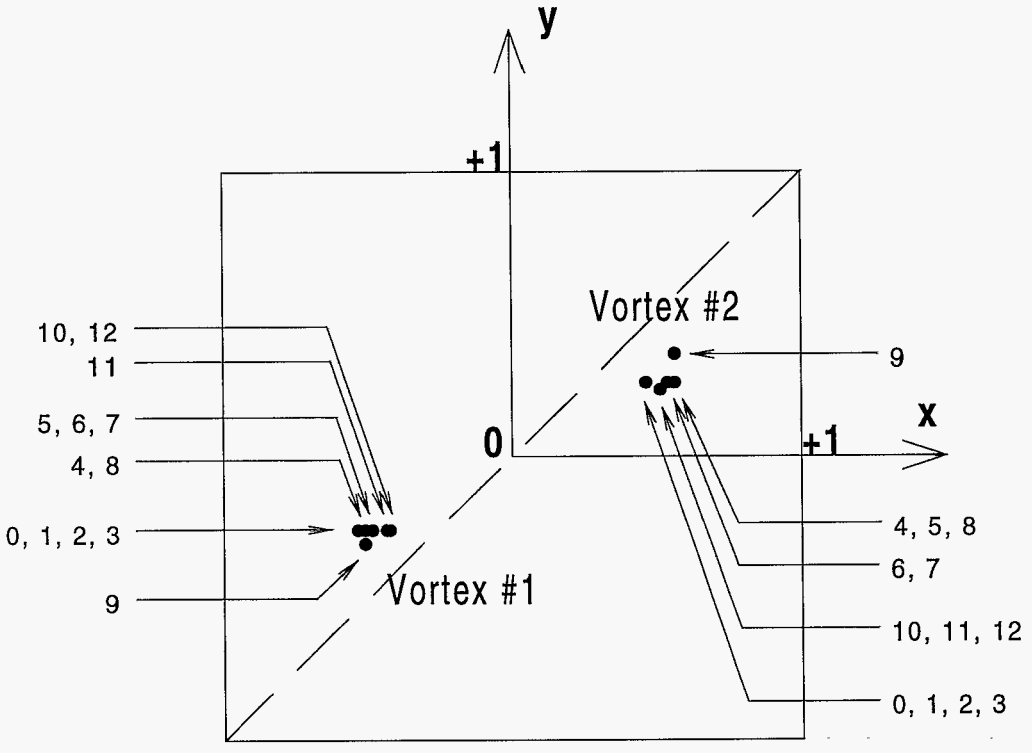

Figure 4.29 The positions of the two vortices shown in Table 4.5 during the transport current depinning experiment

5 CONCLUSIONS

The thermal depinning of an Abrikosov vortex trapped in a SNIS Nb-Ag-Al-Al_xO_y-Nb planar junction has been studied as a function of an external magnetic field perpendicular to the plane of the junction. From the results of this work, it appears that the vortex changes behavior dramatically under the influence magnetic fields up to 10 mG. First of all, the temperature T_0^{dep} where the vortex is first depinned, is lowered by about 100 mK. Secondly, once this temperature is reached, the vortex becomes very unstable resulting in an almost continuous range of depinning temperatures. And finally there were gaps present in the depinning temperature scale of the order of 100 mK. These gaps seem to have no relation to the transition temperatures of either the films or the junction. The superconducting order parameter Δ/Δ_0 and the superfluid density ρ_s were calculated at various depinning temperatures. In zero applied field, it was found that $T_0^{dep} = 8.815$ K where Δ/Δ_0 was equal to 0.178 and ρ_s equal to 3.16%. In an applied magnetic field of 10 mG perpendicular to the junction, the corresponding T_0^{dep}, Δ/Δ_0 and ρ_s values were 8.699 K, 0.265 and 7.03%. Similarly, in an applied magnetic field of -10 mG, these values were 8.648 K, 0.295 and 8.72% respectively. Also there is no "vortex free" region close to T_c in this particular junction as it was reported for Pb. It should also be mentioned that the above results are subject to some discrepancy since the initial pinning site for each experiment was different, resulting in different initial conditions. In general, the strength of the pinning potential at different sites varies.

For the transport current depinning experiment, it was found that the data lie on a straight line and that there are not any large jumps in I_0 as it was seen in Pb junctions. Also the $I_0(T)$ data were fitted very successfully by a transition type power law: $I_0 = I_0(0)(1 - (T/T_c)^4)^3$.

The motion of two trapped vortices with the same polarity was also studied. It was found that even when transport currents were applied in order to push the vortices towards a particular direction, the two vortices would not deviate much from their initial position. The vortices were always diagonally opposite to each other and along one of the main diagonals of the square junction, thus minimizing their repulsive interaction.

APPENDIX A CONVERSION BETWEEN MKSA AND GAUSSIAN UNITS

The Gaussian system of units is normally used in the literature when deriving a theoretical expression in electromagnetism. The main reason is clarity and convenience, especially when it comes to treat the electric and magnetic fields in an equal basis, and also to relate the miscellaneous constants appearing in Maxwell equations to the speed of light c. In spite of its great usefulness in the theory of electromagnetism, the Gaussian system of units is rarely used in practice for measurements. The MKSA system has prevailed experimentally, mainly due to historical reasons and its easiness of use in large-scale engineering applications. In general, there is some confusion when converting from one system to the other because the physical quantities are not always defined in the same way, and also because the basic units are different. The main purpose of this Appendix is to explain in some detail how certain results which were measured in MKSA units, were used in formulas which were expressed in Gaussian units.

Small junction limit of sample MB3-126

As it was mentioned in the discussion following Eq. (2.15), the small junction limit is achieved when $w \ll \lambda_J$ or when

$$\frac{\lambda_J}{w} = \sqrt{\frac{c\Phi_0}{8\pi^2 d_{eff} I_0}} \gg 1 \tag{A.1}$$

where $I_0 = J_0 w^2$. In this section, the quantity λ_J/w will be calculated for the sample MB3-126 at the reference temperature of 7.993 K. I_0 would be chosen to be equal to $I_{00} = 759\mu$A, the maximum supercurrent at 7.993 K. The Gaussian unit of current is the statampere. Jackson [47] provides a usefull unit conversion table between MKSA and Gaussian units according to which 1 ampere corresponds to 3×10^9 statamperes. The reason for writting "corresponds" instead of "equals" is that the current (more precisely the charge) is defined differently in the two system of units and in general it is wrong to write 1 A $= 3 \times 10^9$ statamperes. If this difference is kept into mind, the table in Jackson's book can be used to convert units. In the above examble, the I_0 of 759×10^{-6} A corresponds to $I_0 = 2.3 \times 10^6$

statamperes. The MB3-126 junction had a thickness of $\sim 6000\mathring{A}$ and by taking the penentration lenght *of Nb at 7.993 K to be* $\sim 500\mathring{A}$, we have $d_{eff} \sim 6000 + 500 + 500 = 7000\mathring{A} = 7 \times 10^{-5}$ cm. In Gaussian units $\Phi_0 = 2.07 \times 10^{-7}$ G-cm^2 and $c = 3 \times 10^{10}$ cm / s. Substituting all the above to Eq. (A.1) we have

$$\frac{\lambda_J}{w} = \sqrt{\frac{3 \times 10^{10}\text{cm/s} \times 2.07 \times 10^{-7}\text{Gcm}^2}{8\pi^2 \times 7 \times 10^{-5}\text{cm} \times 2.3 \times 10^{6}\text{statamperes}}} = 0.7\sqrt{\frac{\text{G} \times \text{cm}^2}{\text{statamperes} \times \text{s}}} \tag{A.2}$$

at 7.993 K. But statamperes $\times$ s = statcoulombs and from dimensional analysis in Gaussian units 1 G = [B] = [E] = [q/r^2] = statcoulombs / cm ^{2} and so the above expression is dimensionless as it should be. The above calculation shows that at 7.993 K $\lambda_J \sim w$ which means that this temperature is the crossover from the large to the small junction limit. However, the diffraction patterns taken at 7.993 K exhibited good characteristics indicating that practically the small junction limit was satisfied.

Elementary pinning force in practical units

In this section, the Eq. (4.3) (Gaussian units) will be expressed in MKSA units so as to allow direct substitution of the measured currents, which are usually expressed in mA. The Nb films used in the present work had a width of about $w = 50\mu$m. With the value of Φ_0 given in the last section, Eq. (4.3) becomes

$$f_p = 3.024\frac{2.07 \times 10^{-7}\text{Gcm}^2}{\pi \times 3 \times 10^{10}\text{cm/s} \times 5 \times 10^{-3}\text{cm}} I_p^{dep}(\text{statamperes}) \tag{A.3}$$

As in the last section, statamperes $\times$ s = statcoulombs and G $\times$ statcoulombs = [B][q] = [E][q] = [F/q][q] = [F] = dynes which means that

$$\frac{f_p}{I_p^{dep}(T)} = 1.33 \times 10^{-15}(\text{dynes/statamperes}) \tag{A.4}$$

Using the fact that 1 dyne = 10^{-5} N, as well as that 1 A corresponds to 3×10^9 statamperes, the last expression can be written in MKSA units as

$$\frac{f_p}{I_p^{dep}(T)} = 1.33 \times 10^{-15} \times 10^{-5} \times 3 \times 10^{9} = 4.00 \times 10^{-11}(\text{N/A}) \tag{A.5}$$

APPENDIX B GLOSSARY AND TERMINOLOGY

CGR: Carbon Glass Resistor. This resistor, fabricated from a carbon-impregnated glass matrix, has the property of having a relatively high resistance ($\sim 1000\Omega$) at very low temperatures (4 K) and so it can be used as a thermometer with the aid of an accurate $R(T)$ calibration curve.

Condensation energy: The free energy difference between the normal and the superconducting state.

Depinning: The opposite of "pinning" (see below). The process of providing external energy to the vortex in the form of electromagnetic force or thermal activation in order to deattach it from its "pinning site" (see below).

Diffraction pattern: An I_c versus B plot, with B either parallel or perpendicular to the plane of the junction. The term "diffraction pattern" comes from the fact that when there are no vortices present in the junction, the form of the $I_c(B)$ plot (with B parallel to the plane of the junction) is similar with that of the Fraunhofer diffraction pattern in Optics.

Pinning: The property of the material defects to attract and eventually trap vortices. This happens because the defects act as small normal regions inside the bulk superconductor and so it takes less free energy if the vortex core, which is basically normal, resides on the defect than if the core is located in the superconducting bulk.

Pinning sites: The defects in a material that cause pinning. Usually all the defects that have one of their dimensions comparable to the vortex core size are possible pinning sites.

Thickness monitor: An instrument that measures the thickness of films. The thickness monitor is basically a vibrating crystal which is placed as close to the sample as possible. As more material is deposited onto the crystal, its characteristic frequency changes. A calibration curve can convert this frequency to thickness measurements.

Turbomolecular drag pump: This pump is used in the high vacuum region ($10^{-4} \rightarrow 10^{-8}$ Torr) and it consists of rotating parts that have bolt-like threads on them. As the threads are rotating, they drag gas molecules with them toward the exhaust of the pump.

BIBLIOGRAPHY

[1] W. Meissner and R. Ochsenfeld, *Naturwissenschaften* **21**, 787 (1993)

[2] M. Tinkham, *Introduction to Superconductivity* (McGraw-Hill, New York, 1996), p. 12

[3] A. A. Abrikosov, Zh. Eksperim. i. Teor. Fiz. **32**, 1442 (1957) [Sov. Phys. JETP **5**, 1174 (1957)];

[4] A. M. Campbell and J. E. Evetts, Adv. Phys. **21**, 199 (1972)

[5] M. Tinkham, *Introduction to Superconductivity* (McGraw-Hill, New York, 1996), p. 11

[6] M. Tinkham, *Introduction to Superconductivity* (McGraw-Hill, New York, 1996), p. 118

[7] T. L. Hylton and M. R. Beasley, Phys. Rev. **B41**, 11669, (1990)

[8] J. Halbritter, Appl. Phys **A 43**, 1 28 (1987)

[9] P. Kofstad, *High Temperature Oxidation of Metals* (Wiley, New York, 1976)

[10] K. E. Gray, J. Low Temp. Phys. **15**, 335 (1974)

[11] M. Tinkham, Phys. Rev. **129**, 2413 (1963)

[12] G. J. Dolan and J. Silcox, in *Low Temperature Physics LT-13 (Proc. 13th Int. Conf. Low Temp. Phys., Boulder, 1972)* (plenum, New York, 1972)

[13] G. J. Dolan and J. Silcox, Phys. Rev. Letters **30**, 603 (1973)

[14] D. Cribier, B. Jacrot, L. M. Rao and B. Farnoux, Phys. Lett. **9**, 106 (1964)

[15] U. Essmann and H. Träuble, Phys. Lett. A **24**, 526 (1967); Phys. Status Solidi **20**, 95

[16] P. G. de Gennes and E. Guyon, Phys. Lett. **3**, 168 (1963)

[17] P. G. de Gennes, Rev. Mod. Phys. **36**, 225 (1964)

[18] P. G. de Gennes, *Superconductivity of Metals and Alloys* (Benjamin, New York, 1966).

[19] P. W. Anderson and J. M. Rowell, Phys. Rev. Letters **10**, 230 (1963)

[20] B. D. Josephson, Adv. Phys. **14**, 419 (1965)

[21] P. W. Anderson, in *Lectures on the Many-Body Problem*, edited by E. R. Caianiello (Academic, New York, 1964), Vol. 2, p. 115.

[22] B. D. Josephson, Rev. Mod. Phys. **36**, 216 (1964)

[23] S. L. Miller, Kevin R. Biagi, John R. Clem, and D. K. Finnemore, Phys. Rev. **B31** 2684 (1985)

[24] O. B. Hyun, D. K. Finnemore, L. A. Schwartzkopf and J. R. Clem, Phys. Rev. Lett. **58**, 599, (1987)

[25] B. D. Josephson, Phys. Lett. **1**, 251 (1962)

[26] S. L. Miller and D. K. Finnemore, Phys. Rev. **B30** 2548 (1984)

[27] O. B. Hyun, Ph. D. dissertation, Iowa State University, (1987)

[28] Qiang Li, Ph. D. dissertation, Iowa State University, (1991)

[29] S. C. Sanders, J. Sok, D. K. Finnemore and Qiang Li, Phys. Rev. **B47** 8996 (1993)

[30] Junghyun Sok and D. K. Finnemore, Phys. Rev. **B50** 12770 (1994)

[31] B. Mayer, J. Mannhart, and H. Hilgenkamp, Appl. Phys. Lett. **68**, 21, (1996)

[32] J. Mannhart, Supercond. Sci. Technol. 9 49 (1996)

[33] J. Bardeen, L. N. Cooper, and J. R. Schrieffer, Phys. Rev. **108**, 1175 (1957)

[34] V. L. Ginzburg and L. D. Landau, Zh. Eksperim. i. Teor. Fiz. **20**, 1064 (1950).

[35] M. Tinkham, *Introduction to Superconductivity* (McGraw-Hill, New York, 1996), p. 14

[36] A. Barone and G. Paterno, *Physics and Applications of the Josephson Effect* (Wiley, New York, 1982), p. 17

[37] A. F. Hebard and T. A. Fulton, Phys. Rev. Lett. **35**, 1310 (1975)

[38] A. Barone et. al., J. Appl. Phys. **53**, 5802 (1982)

[39] B. W. Roberts, *Properties of Selected Superconductive Materials*, 1974 Supplement, National Bureau of Standard Technical Note 825, U.S. Government Printing Office, Washington, D.C., 1974, 11

[40] John Clarke, Phys. Rev. **B4** 2963 (1971)

[41] Junghyun Sok, Ph. D. dissertation, Iowa State University, (1995)

[42] N. L. Rowell and H. J. T. Smith, Can. J. Phys. **54**, 223 (1976)

[43] J. A. Blackburn, H. J. Smith and N. L. Rowell, Phys. Rev. **B11** 1053 (1975)

[44] J. P. Romagnan, A. Gilabert, J. C. Noiray and E. Guyon, Solid State Commun. **14**, 83 (1974)

[45] J. Mannhart, J. Bosch, R. Gross, and R. P. Huebener, Phys. Rev. **B31**, 5267 (1987)

[46] J. Mannhart, J. Bosch, R. Gross, and R. P. Huebener, Phys. Lett. **A 122**, 439 (1987)

[47] J. D. Jackson, *Classical Electrodynamics*, (Wiley, New York, 1975), p. 820

ACKNOWLEDGMENTS

The author wishes to express deep appreciation to his advisor Dr. D. K. Finnemore for his guidance and encouragement throughout the course of this research; to Mr. J. E. Ostenson for his invaluable assistance concerning laboratory techniques; to Mr. G. Steininger for his technical advice and help on machine shop constructions; to M. J. Breitwisch for usefull conversations; to his mentor in computational matters, Dr. Vassilis Charmandaris; and finally to his parents Stavros and Maria Kouzoudis for their endless moral support and concern.

This work was performed at Ames Laboratory under Contract No. W-7405-Eng-82 with the U.S. Department of Energy. The United States goverment has assigned the DOE Report number IS-T ~~1773~~ 1864 to this thesis.